Universidad Nacional Autónoma de México

Posgrado en Ciencia e Ingeniería de Materiales
Instituto de Investigaciones en Materiales

FLOW OF SINGLE AIR BUBBLES IN COMPLEX FLUIDS

Tesis

que para obtener el grado de

DOCTOR EN CIENCIA E INGENIERÍA DE MATERIALES

PRESENTA

M. en C. Enrique Soto Castruita

Tutor Principal: Dr. Octavio Manero Brito
Co-tutor: Dr. Roberto Zenit Camacho

México D.F., Enero de 2008

UNAM
POSGRADO
Ciencia e Ingeniería de Materiales

COORDINACION DEL POSGRADO EN CIENCIA E INGENIERIA DE MATERIALES
INSTITUTO DE INVESTIGACIONES EN MATERIALES EDIFICIO "P", UNAM
CIRCUITO EXTERIOR, CIUDAD UNIVERSITARIA
04510 MEXICO, D.F.
TEL: 56224730 Y 56224731
pceim@www.posgrado.unam.mx

OF. PCeIM/05/08

M. C. ENRIQUE SOTO CASTRUITA
P R E S E N T E

De acuerdo a su solicitud, para presentar su examen de grado de Doctor correspondiente al Programa de Doctorado en Ciencia e Ingeniería de Materiales, en el que defenderá su tesis titulada **"Flow of single air bubles in complex fluids"**, le informo que el Comité Académico en su sesión del 27 de noviembre de 2007, acordó nombrar al siguiente jurado:

CARGO	NOMBRE	ADSCRIPCION
Presidente	Dr. Federico Méndez Lavielle	Facultad de Ingeniería
Primer Vocal	Dr. Octavio Manero Brito	Instituto de Investigaciones en Materiales
Segundo Vocal	Dr. Andrew Belmonte	Pensylvania State University
Tercer Vocal	Dr. Baltasar Mena Iniesta	Instituto de Ingeniería
Secretario	Dr. Eduardo Ramos Mora	Centro de Investigación en Energía

Agradeceré a usted entregar en esta coordinación los votos aprobatorios con la firma de cada jurado, en las formas anexas, y ponerse de acuerdo con su jurado para definir la fecha del examen y hacérmelo saber.

Se le informa al jurado que cuenta con un plazo de 20 días hábiles para evaluar la tesis y emitir su dictamen

Sin otro particular de momento, aprovecho la ocasión para enviarle un saludo cordial.

Atentamente
Cd. Universitaria, D.F., a 8 de enero de 2008.

DR. RICARDO VERA GRAZIANO
COORDINADOR

c.c.p.-Integrantes del Jurado

Agradecimientos

A la Dra. Celine Goujon por su intensa colaboración, su asesoría, entusiasmo y dedicación. Sin ella este trabajo no hubiera sido el mismo.

Al Dr. Roberto Zenit por todo su apoyo, paciencia y dirección durante el desarrollo de este trabajo.

Al Dr. Octavio Manero por su asesoría.

Al Dr. Ángel Enrique Chávez por sus valiosos comentarios y optimismo.

Al Dr. José Ramón Herrera y a Daniel Chehata quienes trabajaron en este tema con anterioridad y sentaron las bases para continuarlo.

A la QFB Araceli Ordóñez Medrano por la pronta realización de las pruebas de tensión superficial.

A la Universidad Nacional Autónoma de México por el tiempo que pase dentro de ella.

Al Instituto de Investigaciones Materiales y al Posgrado en Ciencia e Ingeniería de Materiales por todo las facilidades otorgadas para la realización de este trabajo.

Agradezco al CONACyT y a la DGEP por las becas otorgadas para la realización de este trabajo.

Finalmente, quiero agradecer a todos aquellos que de alguna u otra manera estuvieron conmigo durante la realización de esta tesis.

¡Gracias por el cariño, amistad y apoyo a lo largo de esta etapa!

Resumen

En este trabajo se estudia el ascenso libre de burbujas de aire en un polímero asociativo hidrofóbicamente modificado soluble en un medio acuoso y alcalino. Las propiedades reológicas de la disolución están determinadas por los grupos hidrofóbicos: a moderadas rapideces de deformación el sistema se estructura, la viscosidad se incrementa y aparecen los esfuerzos normales. Para rapideces de deformación mayores el sistema se alinea y la viscosidad disminuye. Estos fluidos presentan un comportamiento casi newtoniano para pequeñas rapideces de deformación, pero se comportan como viscoelasticos para deformaciones mayores. Experimentalmente se observa la presencia de una discontinuidad a un volumen critico, para la curva velocidad vs volumen. Esta discontinuidad se asocia con un cambio de la forma de la burbuja, a volúmenes por debajo del crítico las burbujas son esferoidales y a volúmenes por arriba del crítico presentan la formación de una cola. La aparición de la cola esta asociada a la formación de un punto de inflexión en la superficie de la burbuja y se asocia con el momento en que la elasticidad del fluido se manifiesta. Se propone un número adimensional que relaciona la elasticidad y la tensión superficial, a un valor crítico este número se presenta la aparición de la discontinuidad. Este criterio se prueba para varios líquidos con diferentes propiedades reológicas y funciona para todos los casos. También se presenta un estudio de la contribución de los diferentes parámetros involucrados en la magnitud de la discontinuidad. Finalmente, se muestran fotografías de colas de burbujas con formas peculiares.

0.1 Objetivo

Determinar las condiciones a las que se presenta la discontinuidad en la velocidad terminal de una burbuja ascendiendo libremente en fluidos viscoelásticos.

0.2 Introducción

El movimiento de burbujas en líquidos es de particular interés debido a su importancia en procesos químicos y físicos, como por ejemplo, tratamiento de aguas residuales y la extracción de petróleo. En el caso de burbujas ascendiendo libremente en fluidos no newtonianos, se observan diversos fenómenos, uno de ellos, es la llamada discontinuidad de la velocidad terminal de la burbuja. Esta discontinuidad se presenta cuando a un ligero incremento de volumen, la velocidad terminal aumenta abruptamente. En 1965 Astarita y Apuzzo fueron los primeros en reportar este comportamiento, seguidos de diferentes autores que lo confirman (Barnett, Humphrey y Litt, 1966; Calderbank, Johnson y Loudon, 1970; Leal, Skoog y Acrivos, 1971; Zana y Leal, 1978; Rodrigue, De Kee y Chan Man Fong, 1996; Rodrigue, De Kee y Chan Man Fong, 1998; Herrera-Velarde et al., 2003; Pilz et al., 2007). La discontinuidad se presenta a un volumen crítico. El incremento en la velocidad terminal antes del volumen crítico, en relación a la velocidad después de este valor, varia entre 2 y 6.

Astarita et al. (1965) atribuyeron la aparición de la discontinuidad al cambio en la condición de frontera de rígida a libre. Liu et al. (1995) propusieron que la discontinuidad se debe a la reducción del arrastre debido al cambio de forma de la burbuja antes y después del volumen crítico. Rodrigue et al. (1998) atribuyen este comportamiento a un balance de la elasticidad y las inestabilidades de Marangoni. Por otro lado Herrera-Velarde et al. (2003) sugieren una fuerte relación de la discontinuidad con la formación de una cauda negativa en la parte posterior de la burbuja. Aubry (2007) no sólo apoya el argumento

anterior, sino que sostiene que la caudad negativa impulsa a la burbuja.

En este trabajo, se propone una nueva explicación para predecir bajo que condiciones se presenta la discontinuidad para el caso de un polímero asociativo tipo HASE y la comparación con varios líquidos reportados en la literatura. Se propone una análisis dimensional entre las fuerzas inerciales, viscosas, de superficie y elásticas. La elasticidad del material tiene un papel preponderante en la aparición de la discontinuidad. También se realizaron simulaciones en elemento finito para evaluar la contribución de los diferentes parámetros involucrados en la magnitud de la discontinuidad. Finalmente se presenta un estudio fotográfico de la formación de caudas no axisimétricas, que no han sido observadas para este tipo de fluidos con anterioridad.

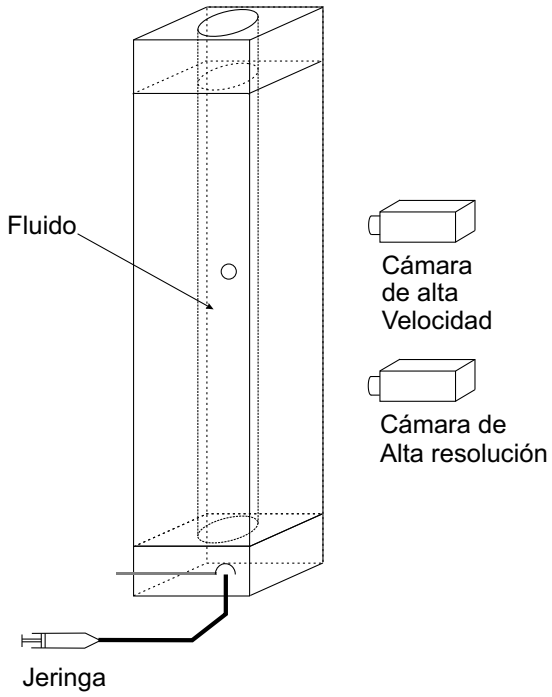

Figure 1: Dispositivo experimental

0.3 Materiales y Métodos

El dispositivo experimental (ver fig. 1) utilizado consiste de un cilindro vertical, con una campana en el fondo, inmerso en una caja de sección cuadrada, ambas partes se llenan con el mismo líquido para disminuir los efectos reflexión.

En la campana se atrapa una burbuja de aire, al girar la campana se libera la burbuja en el seno del líquido. La velocidad, volumen y morfología de la burbuja se obtienen por medio de video de alta velocidad y fotografías. Se utilizo Primal TT-935 que es un polímero asociativo hidrofóbicamente modificado soluble en un medio acuoso y alcalino conocido como HASE por sus siglas en inglés. Como agente alcalinizante se utilizo amino-metilpropanol (AMP), el pH de trabajo se ajusto a 9. Las soluciones polímericas se prepararon en agua destilada y dejando un lapso de al menos 48 horas antes de realizar los experimentos.

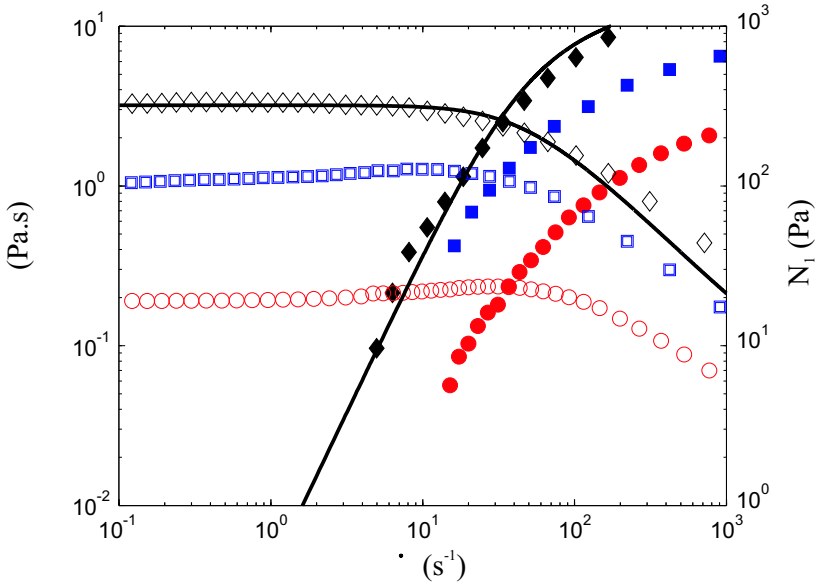

Figure 2: Viscosidad cortante (símbolos vacíos) y primer diferencia de esfuerzos normales (símbolos rellenos) como función de la rapidez de deformación para diferentes concentraciones de HASE. (○) 1.2 %; (□) 1.5 %; (◇) 1.7 %. La línea continua representa la predicción de modelo de Bautista-Manero model para HASE al 1.7 % (Bautista, 1999).

0.4 Resultados Experimentales

La figura 2 muestra la viscosidad y primer diferencia de esfuerzos normales como función de la rapidez de deformación. Se presenta los datos de flujo cortante simple para tres diferentes concentraciones de HASE en medio acuoso con un $pH = 9$. Se observa que a bajas rapideces de deformación la viscosidad permanece casi constante, en ese mismo intervalo la primer diferencia de esfuerzos normales empieza a adquirir valores considerables. A esas mismas rapideces de deformación se mueven las burbujas liberadas en este caso y se presenta la discontinuidad, esto permite separar los efectos de reducción en la viscosidad y los efectos elásticos.

En la figura 3 se presenta la curva velocidad contra volumen para una disolución de HASE al 1.2%. Se observa que a un volumen crítico se presenta la discontinuidad ($V_c = 65mm^3$), se prestan las predicciones para la ley de Stokes y el regimen de Hadamard, usando la viscosidad de flujo cortante simple y

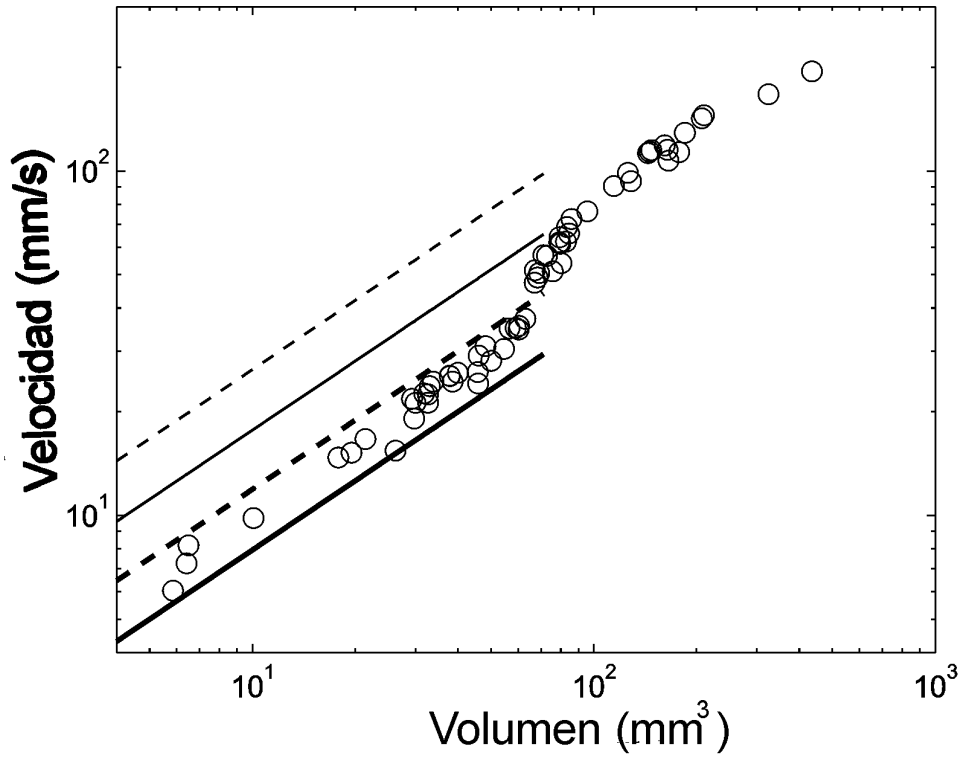

Figure 3: Velocidad de burbujas como función de volumen para HASE al 1.2%. Las líneas son las predicciones teóricas de Stokes (líneas continuas)y Hadamard (líneas discontinuas): (líneas delgadas) $\mu = \mu_{reometro}$; (líneas gruesas) $\mu = \mu_{bola}$.

la determinada por el método de caída de la bola. Debido a que el flujo alrededor de una burbuja no es homogéneo, la viscosidad seleccionada para hacer los cálculos fue la del método de la caída de la bola.

Las burbujas pequeñas (con volúmenes debajo del crítico) tienen forma esferoidal y las burbujas con volúmenes mayores al crítico presentan la formación de una cola larga, como ejemplo de ello se presentan algunas burbujas para el caso del HASE al 1.2% (ver figura 4).

Siempre que se presenta la discontinuidad se observa que la parte posterior de la burbuja cambia de forma, de convexa a cóncava. Para resaltar este hecho se presenta la superposición de los perfiles de un par de burbujas, una con un volumen menor al crítico y otra con un volumen mayor (ver figura 5). Estas observaciones y la presencia de una cauda negativa en la parte posterior de

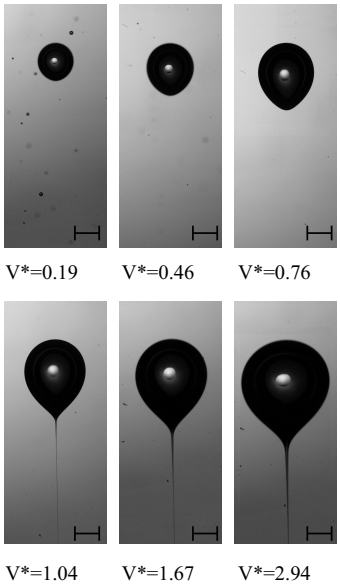

Figure 4: Burbujas para diferentes valores del volumen adimensional $V^* = V/V_c$ para HASE al 1.2 %, con $V_c = 65mm^3$. La escala representa 2 mm.

la burbuja, indican que la elasticidad esta relacionada con la aparición de la discontinuidad. En la siguiente sección se presenta una discusión al respecto.

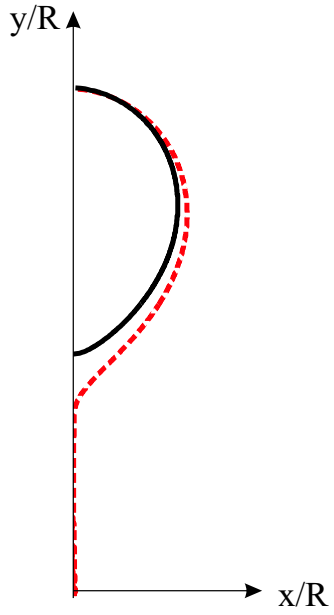

Figure 5: Comparación del perfil de burbujas antes (línea continua) y después (línea discontinua) de la discontinuidad. ($V_{menor} = 49.2mm^3; V_{mayor} = 61.2mm^3; 1.5\%HASE$)

0.5 Análisis dimensional

Se ha encontrado que la discontinuidad siempre esta asociada a un cambio de forma en la burbuja, de ahí que se plantea considerar las fuerzas que pueden modificar dicha forma. Para fluidos no newtonianos las fuerzas involucradas son:

- Fuerzas inerciales: $\rho U^2 d^2$
- Fuerzas viscosas: $\mu U d$
- Fuerzas elásticas: $N_1 d^2$ (flujo cortante)
- Fuerzas de superficie: σd

donde ρ es la densidad del líquido, U la velocidad de la burbuja, d el diámetro equivalente de la burbuja, μ la viscosidad del líquido, N_1 la primer diferencia de esfuerzos normales y σ la tensión superficial. La forma de la burbuja depende de un balance entre las fuerzas mencionadas y las fuerzas

de superficie (estas mantienen la forma esférica de la burbuja). Para fluidos newtonianos, la deformación de la burbuja esta dada por la competencia de las fueras inerciales y viscosas con la fuerza de superficie. Los números de Weber y capilar dan estas relaciones y están definidos como:

$$We = \frac{\rho U^2 d^2}{\sigma} \tag{1}$$

$$Ca = \frac{\mu U}{\sigma} \tag{2}$$

Si cualquiera de los dos números es mayor a uno, la burbuja es deformada. Para el caso de fluidos viscoeslásticos es necesario considerar la relación entre las fuerzas elásticas y las fuerzas de superficie, esta relación se identifica con el símbolo Π y se define como:

$$\Pi = \frac{N_1 d}{\sigma} \tag{3}$$

Este número Π puede expresarse como el producto del número de Deborah y el número Capilar: $\Pi \sim De \times Ca$. El número de Deborah se define como la relación entre un tiempo característico de material t_r y un tiempo característico de observación t_v:

$$De = \frac{t_r}{t_v} \tag{4}$$

Cuando una burbuja se mueve en un medio viscoelástico la elasticidad se manifiesta como una fuerza normal capaz de deformar a la burbuja, siempre y cuando el número Π sea mayor a uno. Este comportamiento se muestra en la figura 6, donde se observa que el número Π tiene un incremento más rápido que los números Ca y We. Además justo en el valor del volumen crítico el número Π adquiere un valor mayor uno, mientras que los otros dos números siempre son menores a Π, esto indica que los efectos elásticos dominan. Los números Ca y We adquieren valores mayores a uno a ciertos volúmenes, que

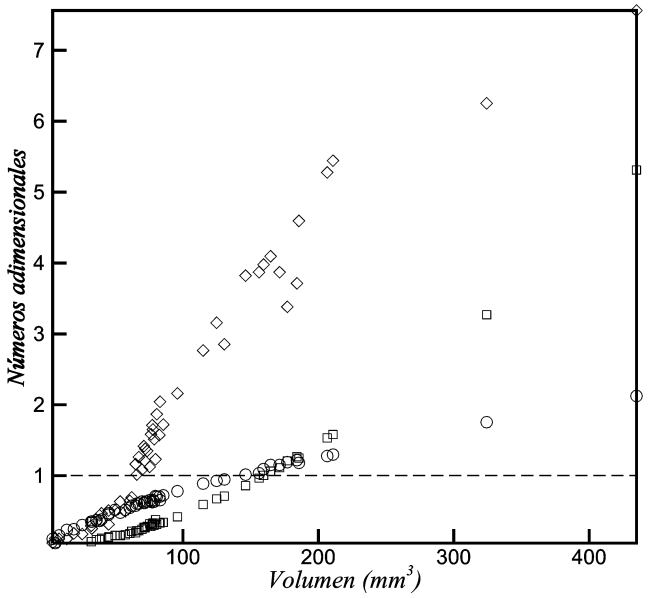

Figure 6: Gráfico del volumen de burbuja vs números adimensionales para un fluido HASE al 1.2% ($\diamond$ número Π, $\square$ número Capilar (Ca) y $\circ$ número de Weber (We)).($V_c = 65mm^3$)

podrían estar relacionados con cambios en la morfología de las burbujas. En este caso la magnitud de la discontinuidad es pequeña, debido a la falta de efectos adelgazantes y por lo tanto no existe una disminución en el arrastre por dicho efecto.

Definiendo el coeficiente de arrastre adimensional: $C_d/C_{d,0}$, donde $C_{d,0}$ es el coeficiente de arrastre de Stokes ($C_{d,0} = 24/Re$), se tiene que para burbujas pequeñas (con volúmenes menores al crítico), el coeficiente adimensional es cercano a 1. Para burbujas con volumen mayor al crítico, la velocidad aumenta y por lo tanto el coeficiente de arrastre disminuye, entonces el coeficiente adimensional es menor a 1. En la figura 7 se muestran el gráfico del coeficiente de arrastre adimensional contra el número Π, es claro que los valores se agrupan en dos zonas; la primera cuando el valor de Π es menor a uno y como era de esperarse el coeficiente es mayor a la unidad, la segunda donde el valor de Π es mayor a 1 y el coeficiente adimensional es menor a 1. De esta manera es posible predecir la aparición de la discontinuidad cuando el número Π es mayor a uno.

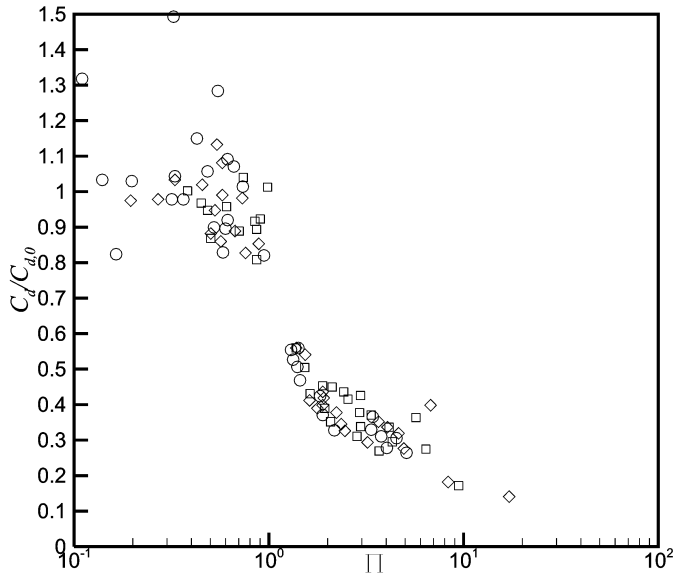

Figure 7: Coeficiente de arrastre adimensional como función del número Π para fluidos del tipo HASE: (○) 1.2%; (□) 1.5%; (◇) 1.7%.

Se realizó una comparación con datos experimentales propios y reportados en la literatura (ver figura 8), de tal manera que para todos los casos se observo el mismo comportamiento que para los fluidos del tipo HASE, lo que indica que el número Π sirve de criterio general para predecir la aparición de la discontinuidad en la velocidad terminal.

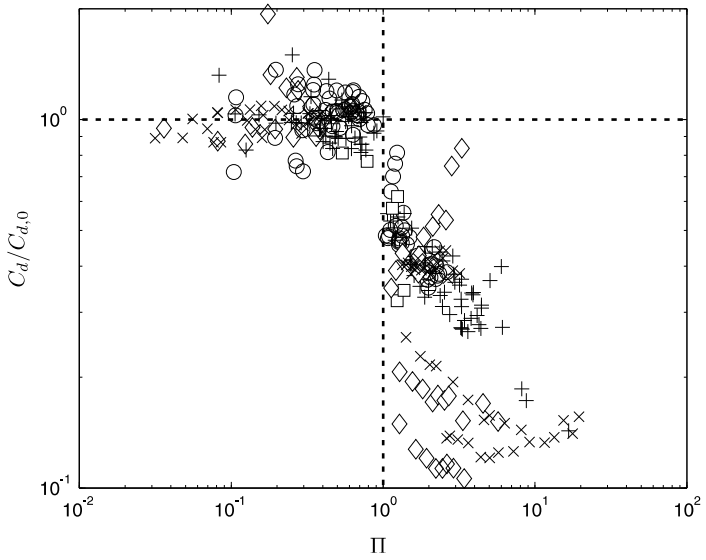

Figure 8: Número Π como una función del número de Weber para diferentes fluidos: (∘) viscoelástico medio acuoso, (□) fluido de Boger, (+) HASE al 1.5%, (⋄) glicerina agua y dodecilsulfonato de sodio en medio acuoso, Rodrigue, De Kee y Chan Man Fong (1996); Rodrigue, De Kee and Chan Man Fong (1998); Rodrigue and De Kee, (1999), (×) agua $80wt.\%$, glicerina $20wt.\%$ y $0.5wt.\%$ de poli(acrilamida) y dodecilsulfato de sodio, Rodrigue and Blanchet (2002).

0.6 Magnitud de la discontinuidad

En la tabla 1 se presentan los principales factores involucrados en la magnitud de la discontinuidad. Para evaluar el efecto de cada uno de ellos se realizaron simulaciones numéricas en elemento finito y se compararon con los resultados experimentales. Experimentalmente se puede obtener la reducción en el arrastre por medio de la relación:

$$\frac{Cd_{,2}}{Cd_{,1}} = \frac{d_{,2}}{d,1}(\frac{V_{,1}}{V_{,2}})^2 \tag{5}$$

donde C_d es el coeficiente de arrastre, V la velocidad terminal de la burbuja y d el diámetro equivalente de la burbuja. Los subindices 2 y 1 se refieren a las burbujas con volumen por arriba y debajo del crítico respectivamente. El coeficiente de arrastre se puede calcular con la fuerza neta sobre la superficie en la dirección de flujo F_d, de tal manera que se puede determinar por medio

Table 1: Principales contribuciones a la discontinuidad para el experimento y la simulación.

Experimento	Simulación
Viscosidad	Viscosidad
Velocidad de burbuja	Velocidad de burbuja
Forma de burbuja	Forma de burbuja
Condición de frontera	Condición de frontera (con o sin deslizamiento)
Elasticidad	

de la ecuación:

$$C_d = \frac{2F_d}{\pi\rho(V)^2(\frac{d}{2})^2} \tag{6}$$

En la simulación se utilizó el perfil correspondiente y las propiedades del fluido bajo las condiciones del experimento. Para la simulación, la condición de frontera se consideró rígida para burbujas con volumen menor al crítico y móvil para burbujas con volumen mayor.

De la simulaciones se obtuvo que la reducción en el arrastre es $\frac{Cd_{,2slip}}{Cd_{,1nonslip}} = 0.446$, mientras que experimentalmente es $\frac{Cd_{,2}}{Cd_{,1}} = 0.412$. Dado que la reducción en el arrastre es mayor en el caso experimental, donde todos los efectos están incluidos, y que la única contribución importante no considera en la simulación es la elasticidad del fluido, se dice que esta propiedad es muy importante para la aparición de la discontinuidad. Lo mismo ocurre para los diversos casos probados en esta sección.

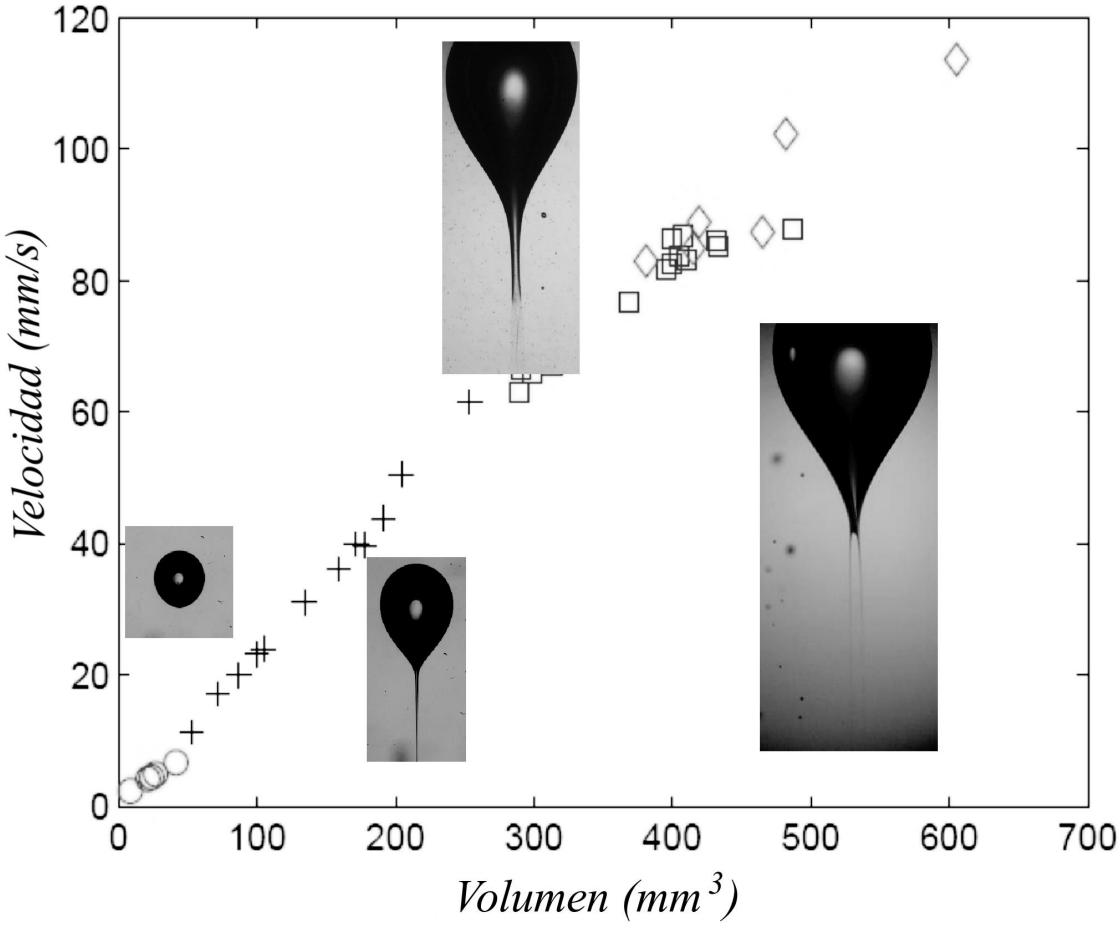

Figure 9: Velocidad como función del volumen para HASE al 1.5%. (∘) burbujas esferoidales; (+) cola axisimétrica (tip streaming); (□) cola 2D tipo cuchilla; (⋄) doblecola 2D tipo cuchilla.

0.7 Burbujas no axisimétricas

Se presentan diversas formas para las burbujas en un amplio intervalo de volúmenes. La figura 9 muestra la velocidad como función del volumen y las diversas formas encontradas. Se observa que existen ciertas regiones en las que las burbujas adquieren una forma especifica, aparentemente se tiene un volumen crítico para cada caso. Sin embargo, hasta ahora no se cuenta con alguna explicación y no se tiene idea de que estas observaciones hayan sido reportadas con anterioridad.

Conclusiones

La discontinuidad esta relacionada con las propiedades reológicas del los fluidos. El cambio de forma en la burbuja de convexa a cóncava se asocia a la discontinuidad, junto con la formación de la cauda negativa. Se presenta un críterio ($\Pi > 1$) capaz de predecir la aparición de la discontinuidad y se aplicó a diversos fluidos reportados en la literatura corroborando su funcionalidad. Para evaluar las principales contribuciones en la magnitud de la discontinuidad se realizaron simulaciones numéricas, como resultado se obtuvo que la elasticidad contribuye de manera importante. También se presenta un estudio fotográfico de la forma de burbujas con volúmenes mayores al crítico y se presentan formas peculiares, que aparecen a ciertos volúmenes, para las cuales no se cuenta con explicación, pero que no han sido reportadas hasta la fecha.

Contents

List of Figures

0.1 Abstract

The motion of air bubbles in aqueous solutions of a hydrophobic alkali-swellable associative polymer is studied in this work. The associative nature of these polymer systems dictates their rheological properties: for moderate values of the shear rate, the formation of structure can lead to a shear-thickening behavior and to the appearance of first normal stress difference. For larger shear rates, the polymer associations can be broken, leading to shear thinning. In general, these fluids show a Newtonian behavior for small values of the shear rate, but behave as viscoelastic liquids for large shear rates. Experimental results show the appearance of a critical bubble volume at which a discontinuity in the relation velocity-volume occurs; however, the velocity increase found in this case is not as large as that previously reported for the case of shear-thinning viscoelastic fluids. The discontinuity is associated with a significant change of the bubble shape: before the critical volume, the bubbles are convex spheroids, while past the critical volume a sharp cusped end appears. The appearance of the tail is also associated with the appearance of an inflection point (change of curvature) on the bubble surface. Moreover, since the rheology of the liquids is measured it was found that the discontinuity, and hence the change of shape, occurs when the elastic nature of the liquid first manifests itself (appearance of a first normal stress difference). A comparison of the measured velocities for small bubbles with predictions from a Stokes-Hadamard law shows a discrepancy. The Newtonian viscosity measured in a viscometric flow was smaller than that determined from a falling-ball arrangement. Considering the viscosity measured under this nonviscometric flow, the comparison between theory and experiments was very good for bubbles having volumes lower than the critical one. Moreover, due to the importance of the elasticity, and due to the change of the shape of the bubble, a dimensionless number formed as the ratio of elastic to surface tension forces clearly defines

the change of the behavior for the bubbles rising in these fluids. Furthermore, such criterion was tested for several classes of fluids (viscoelastic, shear thinning inelastic and constant viscosity elastic liquids). A study of the magnitude of the different contributions leading to the bubble velocity discontinuity is also presented. Finally, a photographic study of the peculiar shapes of the bubble tails, tip-, and edge-streaming phenomena is presented. To our knowledge, experiments in this class of fluids have not been reported to date.

0.2 Objective

Determine the flow conditions and viscoelastic properties of fluids necessary for a rising bubble to exhibit the bubble velocity discontinuity in complex fluids.

0.3 Originality

The flow of non-Newtonian fluids is a relevant due to the fact that most of *real materials* show this behavior. In particular, the motion of bubbles in non-Newtonian fluids is important for several industrial applications: waste water treatment, handling and processing of fermentations broths, polymer devolatization, bubble column, metallurgy, plastic foam processing and all processes where multiphasic flow is involved. An extensive work on this issue has been carried out(Chhabra, 1993 and 2006, Kee, 2002); however, the phenomena is not well understood.

At this moment there is a lack of a complete theoretical study of *bubble phenomena* due to its complexity. For this, the starting point is the *simplest case*, an isolated bubble freely rising in a liquid. The non-Newtonian properties of a liquid are responsable of some peculiar observations, such as the negative wake and the bubble velocity discontinuity. In this work, a detailed experimental study is presented to analize the competition among the different forces involved in the bubble phenomena and a criterion for the apparition of the bubble velocity discontinuity is presented.

0.4 Introduction

The study of the motion of air bubbles in liquids has received considerable attention because of its fundamental and practical importance. For the case of Newtonian liquids, there is a vast collection of investigations reporting a wide range of behaviors in many regimes (Clift, Grace & Weber, 1978). The general understanding of such a system is not complete but its state of the art can be considered relatively advanced.

For the case of the motion of gas bubbles in non-Newtonian liquids, there are several unexpected phenomena that are not yet fully understood (Chhabra, 1993; Funschfilling & Li, 2001). Among the peculiar phenomena observed in the case of non-Newtonian liquids, of particular interest is the so-called bubble velocity discontinuity. In a Newtonian fluid, the magnitude of the rising velocity of a gas bubble is proportional to the bubble size and the relation velocity-volume is monotonically increasing. For the case of non-Newtonian liquids, many authors (Astarita & Apuzzo, 1965; Barnett, Humphrey & Litt, 1966; Calderbank, Johnson & Loudon, 1970; Leal, Skoog & Acrivos, 1971; Zana & Leal, 1978; Rodrigue, De Kee & Chan Man Fong, 1996; Rodrigue, De Kee & Chan Man Fong, 1998; Herrera-Velarde et al., 2003; Soto et al., 2006; Pilz et al., 2007) have reported the existence of a critical value of the bubble volume for which a discontinuity of the velocity occurs: the bubble velocity increases abruptly for a small increase of the bubble volume.

Astarita & Apuzzo (1965) were the first ones to report that the ratio of the velocity after and before the jump ranged from 2 to 6, depending on the polymer solution. They argued that this discontinuity of the velocity could be the result of a transition from a Stokes regime to a Hadamard regime (a change from a rigid to a free interface). However, it can be shown that the velocity increase resulting from such a change of the boundary conditions would be equal to 1.5. Due to the fact that no discontinuity of the velocity has been

observed for the case of falling spheres, some authors (Barnett, Humphrey & Litt, 1966; Calderbank, Johnson & Loudon, 1970; Leal, Skoog & Acrivos, 1971) have supported this argument, even though it does not predict correctly the increase of the velocity. Astarita & Apuzzo (1965) also pointed out that the shape of the bubbles changed before and after the velocity discontinuity. Liu et al. argued the discontinuity appears due to the drag reduction involved in such change in shape. Rodrigue, De Kee & Chan Man Fong (1998) proposed an explanation for the discontinuity. They argued that it results from a balance between elastic and Marangoni instabilities providing another major difference between Newtonian and non-Newtonian hydrodynamics. In a related study, Rodrigue, De Kee & Chan Man Fong (1996) reported the effect of surfactants in the liquid and concluded that surface active agents as well as elastic forces must be simultaneously present in order to generate a sudden jump in velocity. Herrera-Velarde et al. (2003) showed that the appearance of the jump was related to the appearance of the so-called negative wake behind the bubble. Aubry et al (2007) proposed that the negative wake not only coincides with the appearance of a cusp-like trailing end of the rising bubble but also propels the bubble.

In this work, a simple and yet new explanation for the discontinuity is proposed, with a criterion to determine whether or not the bubble velocity discontinuity occurs for the case of air bubbles moving an associative polymer (HASE) and the comparison with several non-Newtonian liquids. A dimensionless analysis of the different forces (inertia, viscous, surface, elastic) shows that the discontinuity occurs when the elastic forces dominate the flow. Although there are numerous experimental results reporting this phenomenon, in most cases not all the properties are reported; hence a proper reexamination of all the existent data is not possible. To comprehensively study this phenomenon, we have carried out an extensive experimental study

of the subject.

In Chapter 1, *background*, a brief introduction of the fundamental concepts are shown. In Chapter 2, *Methods and materials*, the experimental methods and fluids properties are presented. The experimental results for single air bubbles rising in five different types of liquids: aqueous associative polymer(HASE), aqueous shear thinning viscoelastic liquids, non-aqueous shear thinning viscoelastic liquids, Boger fluids (elastic liquids with a constant viscosity), and shear thinning liquids are included in Chapter 3, *Experimental evidence*. Chapter 4, *Dimensionless analysis*, presents a discussion of the experimental results and an explanation for the discontinuity of the velocity based on a dimensionless analysis proposing the idea that elasticity dominates the equilibrium forces . Finally, in the Chapter 5, *Velocity discontinuity magnitude*, an examination of the bubble drag coefficient, shapes of bubbles and the rheological properties of the fluids are evaluated using finite element Newtonian simulations.

Chapter 1

Background

In this chapter the basic concepts are discussed. In the first section, the essential information about flow of fluids around spheres in Newtonian and non-Newtonian fluids is presented. Thereafter, a review of the *bubble velocity discontinuity* state of art is discussed. In the second part, we deal with the fluids properties, the non-Newtonian character of polymeric liquids and their structural composition. Finally, some remarks about the air-liquid interface are included.

1.1 Flow around bubbles

The molecules that constitute a liquid tend to assemble together to minimize the total energy of the system, so the liquids drops tend to adopt shapes that minimize their surface area. The sphere is the geometrical shape with the smallest surface-volume ratio and therefore liquids droplets are spherical. However, there may be other forces in competition against the tendency to adopt the spherical shape; for example, the gravity may flatten spheres into puddles(Atkins, 2002).

In our case, a bubble can be thought as a drop of air surrounded by liquid.

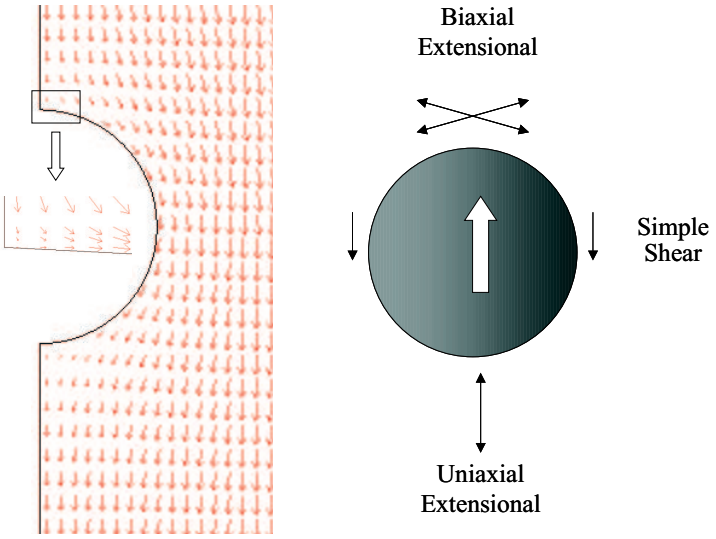

Figure 1.1: Inhomogeneous flow around a sphere. Left: Velocity field around a sphere and magnification of the frontal profile ($Re << 1$). Right: Schematic representation of the different homogeneous flows presented.

The figure 1.1 shows the velocity field around a spherical object in steady state. It can be seen that the flow is complex and not homogeneous, this being the reason why flow around objects is not easy to understand for every condition. Some analytical solutions are available for the flow around spheres; however, they are limited to slow flows. Other important parameter is the boundary condition that can be rigid or mobile; in the first case the boundary is considered as a fixed surface and in the second one the boundary moves with the film of liquid aside it.

1.1.1 Creeping flow around a sphere

One of the classical problems in fluid dynamics is the small Reynolds number flow past an sphere; known as *creeping flow*. The Reynolds number is a balance between inertial and viscous forces, defined as:

$$Re = \frac{inertial\ forces}{viscous\ forces} = \frac{\rho d_e U}{\mu} = \frac{U d_e}{\nu} \tag{1.1}$$

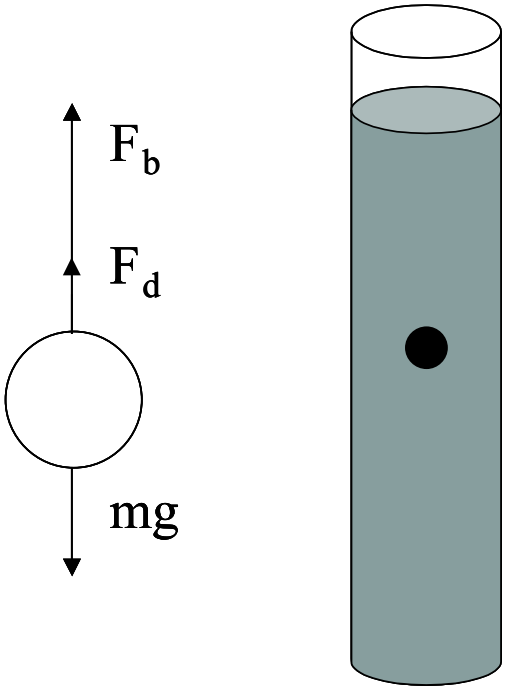

Figure 1.2: Free body diagram of a sphere. Buoyancy force (F_b), drag force (F_d and weight (mg).

where ρ is the fluid density, d_e is the sphere equivalent diameter, U is the velocity, μ is the liquid viscosity and ν is the cinematic viscosity. Then, a small Reynolds number implies that the flow is slow and laminar. Under such flow conditions there is no wake and the flow is smooth without instabilities.

The forces acting on the sphere, as it falls or ascends into the fluid, are shown in figure 1.2. These forces are the buoyancy (F_b), the drag (F_d) and the weight (mg). The first two forces act upwards, and the third one acts downwards. Then, the following balance equation can be written,

$$F_b + F_d = mg \tag{1.2}$$

The buoyancy force is simply the weight of displaced fluid:

$$F_b = m_{df} g = \frac{4}{3}\pi R^3 \rho_{fluid} g \tag{1.3}$$

where m_{df} is the mass of displaced fluid, R is the sphere radius and ρ_{fluid} is

the fluid density.

Stokes's flow

In a rigid sphere, the non-slip boundary condition of the velocity field ($v_{fluid} = v_{sphere}|_{r=R}$) is considered at the sphere surface and v_z tends to v_∞ at a large distance from the sphere. To calculate the total force acting perpendicularly to the surface, in the motion direction, the pressure $-p\cos\theta$ is considered. Multiplying the pressure on the sphere by the total area $R^2\sin\theta d\theta d\phi$, the surface integral for the normal component of the forces is given:

$$F_n = \int_0^{2\pi}\int_0^{\pi}(-p|_{r=R}\cos\theta)R^2\sin\theta d\theta d\phi \tag{1.4}$$

where R is the sphere radius and p at the surface given by:

$$-p|_{r=R} = p_0 - \rho g R\cos\theta - \frac{3}{2}\frac{\mu v_\infty}{R}\cos\theta \tag{1.5}$$

where v_∞ is the translation sphere velocity. This integral gives:

$$F_n = \frac{4}{3}\pi R^3\rho g + 2\pi\mu R v_\infty \tag{1.6}$$

The tangential contribution is given by:

$$F_t = \int_0^{2\pi}\int_0^{\pi}(+\tau_{r\theta}|_{r=R}\sin\theta)R^2\sin\theta d\theta d\phi \tag{1.7}$$

where $\tau_{r\theta}$ is the shear stress at the sphere surface, expressed as

$$\tau_{r\theta}|_{r=R} = \frac{3}{2}\frac{\mu v_\infty}{R}\sin\theta \tag{1.8}$$

Evaluating the integral

$$F_t = 4\pi\mu R v_\infty \tag{1.9}$$

Recalling 1.2, the total force balance is

$$F = \frac{4}{3}\pi R^3 \rho g + 2\pi\mu R v_\infty + 4\pi\mu R v_\infty \tag{1.10}$$

The first term is the buoyancy force, and the other two are referred to the drag force. Then, the second term is the form contribution and the third is the contribution of friction between the sphere and the fluid. Finally, balance is written

$$mg = \frac{4}{3}\pi R^3 \rho g + 6\pi R \rho g \tag{1.11}$$

It can be seen that the buoyancy forces act at any moment (even at rest) and the drag forces depend on fluid motion, related to the kinetic contribution. The drag force

$$F_d = 6\pi\mu R v_\infty \tag{1.12}$$

is known as *Stokes' law* (Stokes,1880 and Schlichting, 1964). This formula is used to determine settling velocities under gravitational forces through the next relation

$$v_\infty = \frac{R^2(\rho_s - \rho)g}{18\mu} \tag{1.13}$$

where ρ_s is the sphere density. Such relation is useful to calculate *falling bead viscosities* (which will be described in detail in the experimental Chapter). This equation is valid only for Re smaller than 1 and for *rigid* boundary conditions.

The drag can be expressed in dimensionless form as:

$$C_d = \frac{2F_d}{\pi\rho(v_\infty)^2(\frac{d_e}{2})^2} \tag{1.14}$$

From Eqs. 1.14, 1.1 and 1.12, the drag coefficient in *Stokes's flow* is given by:

$$C_d = 24/Re \tag{1.15}$$

Hadamard's flow

In this case, the sphere is itself composed of fluid susceptible to generate an internal circulation that affects the overall drag. It is assumed that the two liquids are immiscible, and that surface tension at the interface is strong enough to keep the *drop* spherical. Then, the velocity of the interface is equal to the velocity of the external fluid at the interface, $v_r = v_\theta = v_s$ and again v_z tends to v_∞ far from the sphere. The *Re* number inside and outside the *drop* should be smaller than unity. Motion equations for this conditions were solved analytically by Hadamard (1911) and Rybczynski (1911). In this case, the drag force is given by

$$F_d = 4\pi\mu R v_\infty \tag{1.16}$$

The terminal velocity of the *drop* is given by

$$v_\infty = \frac{R^2(\rho_s - \rho)g}{12\mu} \tag{1.17}$$

and in the same way as in Stokes's flow using Eqs. 1.14, 1.1 and 1.16, the Hadamard drag coefficient is given by

$$C_d = 16/Re \tag{1.18}$$

1.1.2 Bubbles in Newtonian fluids

For the motion of air bubbles in Newtonian liquids there is a vast number of investigations reporting a wide range of behaviors. Most of this information is summarized in the book *Bubbles, drops and Particles* by R. Clift, J. R. Grace & M. E. Weber, 1978. This book provides an excellent review. However, the general understanding of such systems is not complete.

In this book, drops and bubbles rising freely in a media are grouped in the following three types:

a) *Spherical*: In general, bubbles and drops are approximated by spheres if interfacial tension and/or viscous forces are much more important than inertia forces. A particle is termed spherical if the minor to major axis lies within 10% of unity.

b) *Ellipsoidal*: This term is used to name bubbles and drops which are oblate with convex interface around the entire surface. Frequently such bubbles or drops are not matched exactly with true ellipsoids and symmetry must not be assumed. Moreover, ellipsoidal bubbles and drops commonly undergo periodic deformations and shake which complicate shape characterization.

c) *Spherical-cap* or *ellipsoidal-cap*: Large bubbles and drops tend to adopt flat or indented bases and without symmetry. They look like segments of cut spheres. If an indentation at the rear of the particle is presented, it is said to be *dimpled*. Large spherical-cap may also trail thin envelopes of dispersed fluid referred as *skirts*.

For bubbles and drops rising or falling freely in infinite media it is possible to construct a generalized graphical correlation in terms of the dimensionless numbers:

$$E_o = \frac{g\Delta\rho d_e^2}{\sigma} \tag{1.19}$$

$$M = \frac{g\mu^4\Delta\rho}{\rho^2\sigma^3} \tag{1.20}$$

$$Re = \frac{\rho d_e U}{\mu} \tag{1.21}$$

where E_o is the Eötvös number, M the Morton number and Re the Reynolds number. The resulting plot shown in Fig. 1.3 does not apply to extreme values of density ratio, (ρ_p/ρ), or viscosity ratio, (μ_p/μ), where the subindex refers to the disperse phase. The plot in Fig. 1.3 considers a broad range of fluid properties and particle volumes. Since Re contains the terminal velocity, it

may be used to estimate terminal velocities as well as shape, although in more recent works this plot is a very valuable reference. Something remarkable is that the disperse phase viscosity seems not to play an important role in determining terminal velocities and shapes regimes since it does not appear in any of the three numbers.

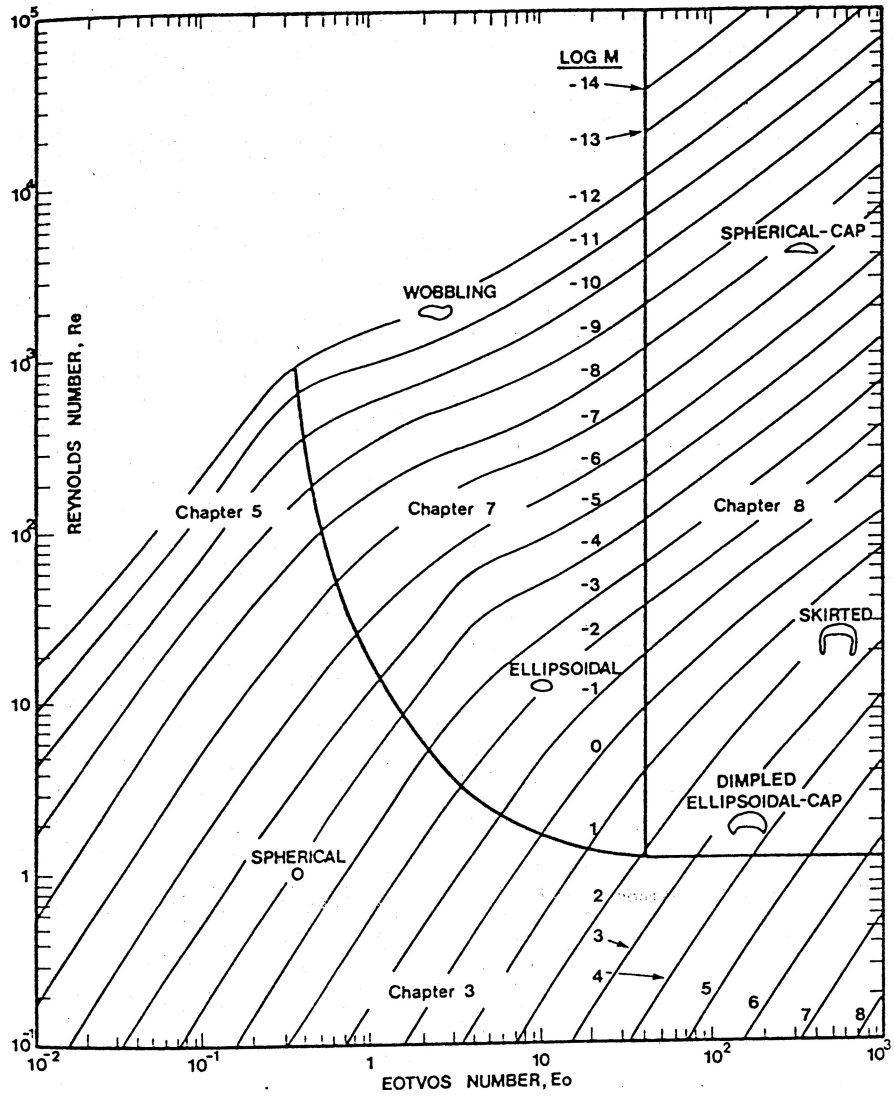

Figure 1.3: Shape regimes for bubbles and drops unhindered gravitational motion through liquids. Taken from Clif,1978.

Free rise of bubbles

The qualitative behavior of a bubble rising freely under gravity in a Newtonian liquid is presented in Fig. 1.4. Additionally, Stokes's law and Hadamard

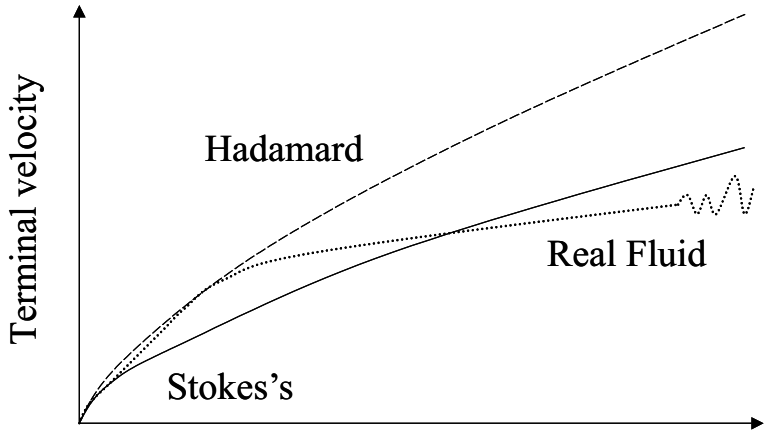

Figure 1.4: Terminal velocity as function of volume. Idealized real fluid (dotted line), Stokes's law (Solid line) and Hadamard's prediction (dashed line).

solutions are presented. For small bubble volumes, the terminal velocity follows Stokes´s, even though the interface is free, because of contamination of the water interface. It implies that the flow around the bubbles is not strong enough to deform the interface and it behaves like a rigid particle. This assumption is supported by some experiments showing that inside the bubble, under this conditions, no recirculations occur. When the volumen is increased, the terminal velocity increases monotonically and lies between both regimes until it reaches Hadamard's solution. At some volume, the velocity falls below the Hadamard's value and for higher volumes, it falls below Stokes's solution. This is attributed to the appearance of inertial effects. Finally, for very large volumes, an instability is observed in the terminal velocity due to turbulence. The bubbles become oblate which leads to an increase of drag.

1.1.3 Bubbles in non-Newtonian fluids and Bubble Velocity Discontinuity

The study of the behavior of bubbles rising freely in non-Newtonian fluids is not fully understood. This is a consequence of the fluids structure, that, in general, is composed of *large molecules*. More details about the chemical nature of *large molecules* will be given in later sections. The size, shape and flexibility of this molecules lead the fluids to exhibit some 'odd' properties in comparison whit those observed for Newtonian liquids (constituted by *small* molecules). Among these differences, change in shape, velocity and mass transfer could be observed. The main topic of this work is the so-called *jump discontinuity*, this is a sudden increase in velocity resulting from a small change in volume. This issue is discussed in detail in the next section.

Bubble velocity discontinuity

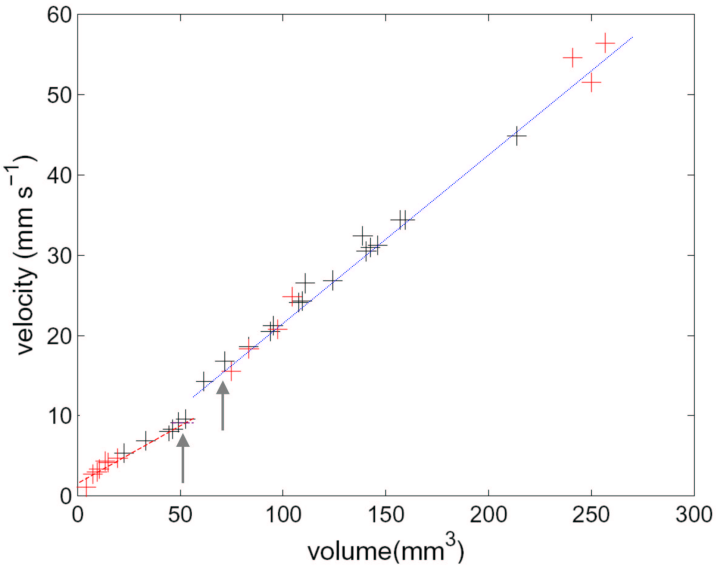

Figure 1.5: Velocity discontinuity plot for an aqueous solution of HASE at 1.5 $wt\%$. Terminal velocity as function of volumen. As increasing the volume the velocity increases monotonically until a critical volume, where the discontinuity appears.

Table 1.1: Magnitude of the discontinuity, ratio of the velocity past the discontinuity and the velocity prior the discontinuity.

Author	System	$\frac{V_a}{V_b}$
Astarita & Apuzzo 1965	Air/polyacrylamide ET-497 and J-100	2.22-5.86
Zana and Leal 1978	Air/poliacrylamide AP-30	4-5
Rodrigue et al 1998	Air/poliacrylamide AP-30/sodium dodecyl sulfate	1.6-5
Herrera-Velarde, et al., 2003	Air/water/ glicerol/poliacrylamide	1.63-2.45

Figure 1.5 shows a typical plot of terminal velocity versus volume, in this case for an aqueous solution of 1.5 HASE $wt\%$. It is clear that there is a critical volume at which an small increment in volume implies a sudden increase in the terminal velocity. This behavior has been reported extensively by several authors in different non-Newtonian liquids. Chhabra (2006) provides a recent summary of previos investigations on that subject. Others important reviews are available in the literature; Chhabra (1993), Kee & Chhabra (2002) and Caswell et al. (2004).

In Table 1.1, some experiment that report the velocity discontinuity are shown. Also shown is the ratio between the velocity past and prior the discontinuity.

The appearance of the discontinuity is related to the non-Newtonian properties of the solutions. In Table 1.2 a summary of the explanations on the origin of the discontinuity are given. The first explanation is based on the well known fact that small bubbles behave like rigid spheres, whereas large bubbles present a mobile interface. However, this explanation is not sufficient to explain discontinuities higher than a 50% increase in velocity, even for Newtonian liquids, since Newtonian liquids do not exhibit this behavior. The second explanation is about the change in shape of the bubble (see Figure 1.6a), several experimental observations are in agreement that the formation of a cusp in the trail end of the bubble coincides with the critical volume.

Table 1.2: Summary the explanations given for the discontinuity.

Author	Conclusions
Astarita & Apuzzo, 1965	Discontinuity is due to transition from stokes to Hadamard regime.
Lui, et al., 1995	Sharp reduction in the drag due to cusping.
Belmonte, 2000	Discontinuity coincides with cusp formation.
Herrera-Velarde, et al., 2003	The discontinuity appears only for volumes greater than the critical and always is related with the presence of the negative wake.

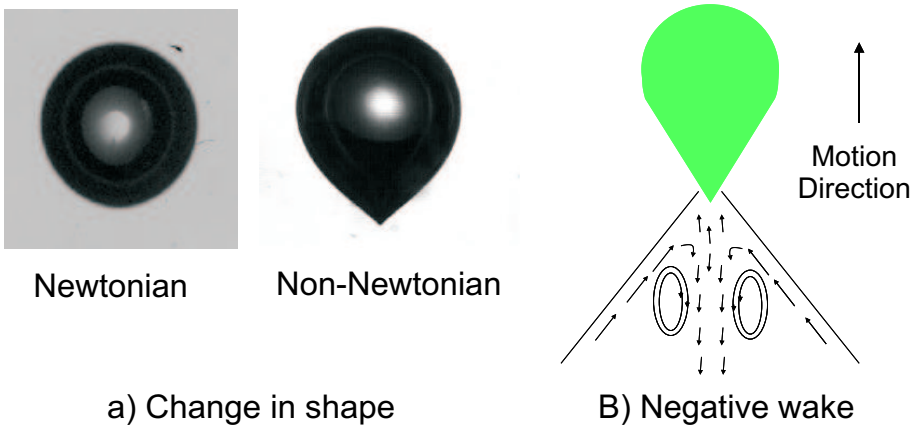

Figure 1.6: a) Comparison of the shapes of a bubble moving in a Newtonian liquid and one moving in a non-Newtonian fluid. b) Sketch of the velocity vectors in the negative wake of a bubble rising in a non-Newtonian fluid.

Finally, a key experimental observation is the formation of the negative wake (see Figure 1.6b). In a region, the velocity vectors are in the direction of the motion of the bubble. Directly below the trailing end and close to the vertical axis of the rising bubble, the velocity vectors are in the direction of the motion of the bubble, but at a short distance behind the trailing end, the velocity is in the opposite direction (Sigli, 1977, and Herrera-Velarde, 2003). The fact that both phenomena have been associated and have been observed only in elastic fluids, is a strong evidence that the elasticity plays an important role in the velocity discontinuity.

Wall effects

At small Re, the perturbation around a body is of long-range interaction. Hence, the walls may have importance on the falling objects terminal velocity. In the case of spheres in Newtonian liquids, the drag correction factor due to walls can be calculated with the Faxén correction (Happel, 1973), which is commonly expressed in the form

$$K_N(R/r) = \frac{1}{1 - f(R/r)} = \frac{U_{Stokes}}{U} \tag{1.22}$$

with

$$\begin{aligned} f(R/r) &= 2.10444(R/r) - 2.08877(R/r)^3 + 0.94813(R/r)^5 \\ &\quad + 1.372(R/r)^6 - 3.87(R/r)^8 + 4.19(R/r)^{10} + \cdots \end{aligned} \tag{1.23}$$

where R is the radius of the sphere and r is the container radius. This relation is only valid for Reynolds number smaller than 1. When (R/r) decreases, the wall effects decrease too. Then, it is possible to minimize wall effects keeping (R/r) as small as it can be. It has been shown that for viscoelastic fluids, wall effects appear to be less important than in the motion of Newtonian fluids (Chhabra, 1981). Moreover, the wall correction factor for elastic constant viscosity fluids is given by $f(R/r) = 1 - 0.17R/r$ for Deborah numbers larger than 0.2 (Chhabra, 1988).

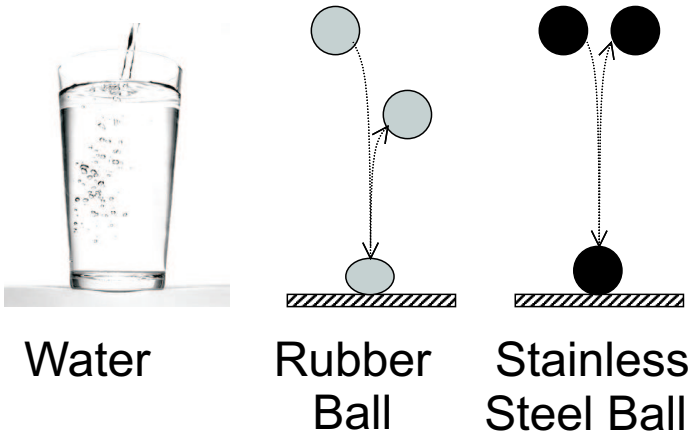

Figure 1.7: Viscous, viscoelastic and elastic behavior of materials.

1.2 Rheology

Rheology is the study of the deformation and flow of matter under the influence of an applied stress. The term was coined by Eugene Bingham, a professor at Lehigh University, in 1920, from a suggestion by a colleague, Markus Reiner. The term was inspired by Heraclitus's famous expression *panta rei* (*everything flows*). It is possible to define two kinds of matter: fluid (liquid or gas) and solid. When a weak continuos constant stress is applied, the fluid matter flows and the solid matter resist. As an example, figure 1.7 illustrates these behaviors. The water fills the glass adopting the shape of the container, the applied stress is dissipated, then the material is viscous. The stainless steel ball, falling from a certain height and impacting against a hard surface, bounces very close to the original height; it means that the applied stress is stored, then the material is elastic. The rubber ball performance is between both behaviors. When the rubber ball impacts against the surface, it deforms with a loss of energy, then the bounce height is smaller than the initial height. This behavior is called *viscoelastic*.

Materials which are pure solids o pure liquids, are just unusual exceptions. *Real materials* exhibit a combination of both properties and show a strong

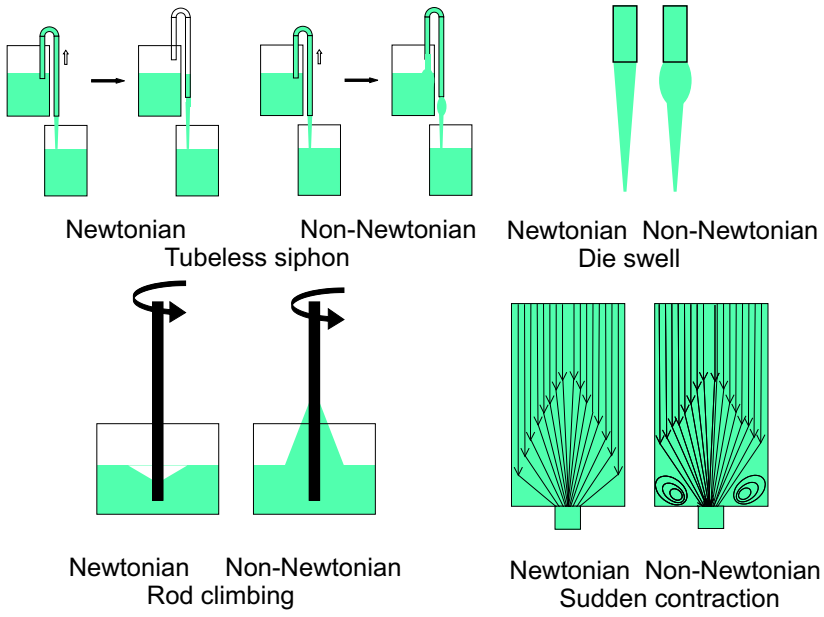

Figure 1.8: Comparison between Newtonian and Non-Newtonian behavior for classical flow conditions. Tubeless siphon, die swell, rod climbing and sudden contraction.

dependence with the deformation rate. In general, as the time scale increases the material changes from elastic to viscous, then a relevant time scale can be defined as a *relaxation time*. Correspondingly, the ratio of the relaxation time of a material to the timescale of a deformation is called *Deborah number*.

$$De = \frac{relaxation\ time\ for\ the\ fluid}{time\ scale\ of\ the\ deformation} \tag{1.24}$$

Small Deborah numbers correspond to situations where the material has time to relax (and behaves in a viscous manner), while large Deborah numbers correspond to situations where the material behaves rather elastically.

Within all the materials that exhibit viscoelasticity, this work focusing in *polymeric fluids*. Several interesting phenomena are shown by this fluids, some of them are presented in Figure 1.8. A brief explanation is in followed:

Tubeless Siphon For a Newtonian liquid the siphon is created by the difference of pressure between the entrance of the tube and the exit, the

atmospheric pressure pushes the liquid through line; when the tube is moved upwards the contact with the liquid is broken and the fluid empties the tube. When the liquid contains large molecules, the molecules align in the direction of stretching resulting in an increase in extensional viscosity. A structure is induced by flow and the fluid behaves like solid in the direction of flow and allows the formation of the tubeless effect. A high ratio of extensional viscosity to shear viscosity is a requirement for the open-siphon experiment.

Die Swell For fully developed flow of a viscoelastic fluid in the tube, a tension along the streamlines associated with the normal stresses is present. When the fluid passes through the exit of the tube into the atmosphere, it will relax the tension along the streamlines by contracting in a longitudinal direction. For an incompressible liquid, this results in lateral expansion of the liquid, giving rise to the die-swell phenomenon. Due to the lack of normal stresses the Newtonian liquids do not show this behavior.

Rod Climbing In the Newtonian liquid, a rotating rod pushes the liquid outward by centrifugal forces, and a downward vortex is generated. On the other hand, for non-Newtonian liquids and for high enough rotational speeds, the fluid moves toward the rod and climbs it. In the case of polymeric liquids it can be argued that the long polymeric chains wrap onto the rod and creep upwards.

Sudden contraction In the case of a Newtonian fluid straight flow in line directly towards the contraction. For the non-Newtonian case not all the fluid lines move directly toward the exit; part of it is trapped in a recirculating region. There are some explanations about the origin of this behavior, but a general criteria is not still accepted. One possible

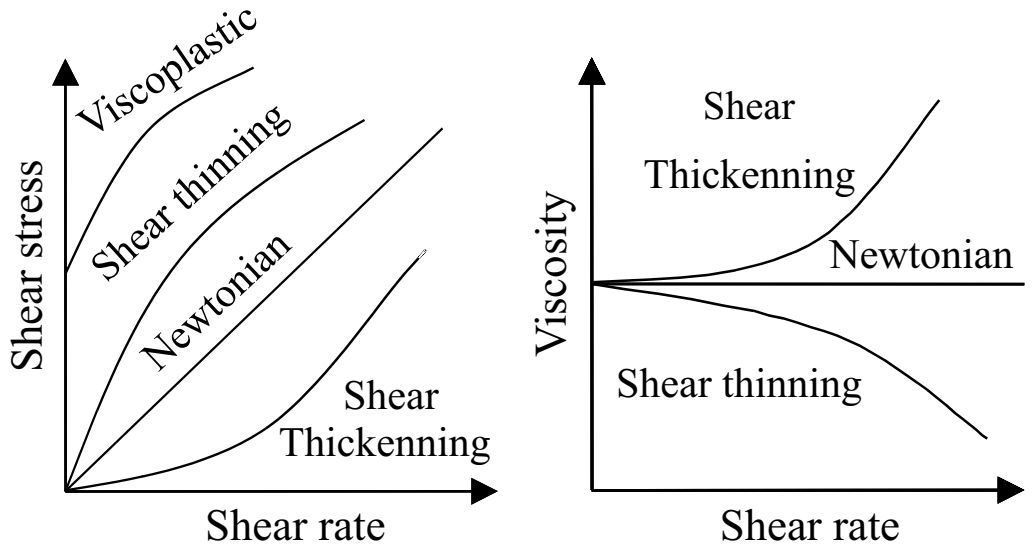

Figure 1.9: Shear stress and viscosity dependence upon shear rate. Newtonian, shear thickening, shear thinning and viscoplastic fluids

explanation is that near the contraction, where the velocity increases and the pressure decreases, the normal stresses relax and promote the formation of a vortex.

1.2.1 Non-Newtonian fluids

The non-Newtonian fluids can be divided in different ways depending on their response when they are deformed. These types of fluids are illustrated in Figure 1.9. The *Newtonian* behavior is characterized by a linear dependence between shear rate and shear stress, as a consequence its viscosity remains constant for any rate of deformation. *Shear thinning* and *shear thickening* fluids are characterized by a non-linear dependence of the shear stress and shear rate. For the first, the slope of the curve shear stress-shear rate decreases, and is reflected in a decrease of viscosity with increasing shear rate. Such behavior is attributed to the alinement and slip of the molecular components of the fluid. In the second fluid, the slope of the curve shear stress-shear rate increases and the viscosity increases with increasing the shear rate. This is believed to the result of assemble of molecular components

under flow generating new structures. Another fluid shown in figure 1.9 is the *viscoplastic*; this fluid has an initially ordered structure that must be broken before the fluid moves; the stress necessary to brake such structure is known as *yield stress*.

Due to the characteristic structural conformation of non-Newtonian liquids a great variety of fluid behaviors can be observed. An interesting phenomena is the time dependence of some fluids called *thixotropy*, in which the structural arrangement is able to acquire different arrays in time for the same flow conditions (Bird, 1976, 2002, Harris, 1997 and Morrison, 2001).

Polymeric solutions and associative polymers

A polymer is a substance composed of molecules with large molecular mass constituted of repeating structural units, or monomers, connected by covalent chemical bonds. A simple model for a polymer considers a set of entangled chains. Then, when a deformation is applied, the chains slip one on top of the other and create an aligned field. This peculiar structure leads to a several interesting and useful mechanical properties (Callister, 1994).

The structural properties of a polymer relate to the physical arrangement of monomers along the backbone of the chain. Structure has a strong influence on the other properties of a polymer. For example, a linear chain polymer may be soluble or insoluble in water depending on whether it is composed of polar monomers (such as polyacrylamide, $(-CH_2CHCONH_2-)_n$) or non-polar monomers (such as styrene). In solution the polymers tend to modify the rheological behavior of the solvent, for this reason they are extensively used in industrial applications as *rheology modifiers*, for example in coating, oil extraction and transportation, food processing, cosmetics and more.

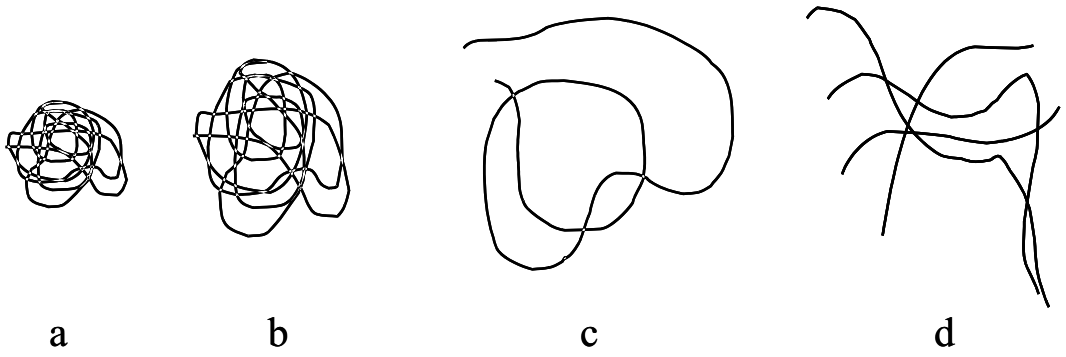

Figure 1.10: Linear polymer swelling in solution. a) Polymer in a bulk, b) Polymer swelling, c) Single chain complete hydrated and d) Single hydrated chains entangled among themselves.

The process of disolving a polymer in a solvent is carried out in various steps; dispersion, swelling and solution. In figure 1.10 a sketch of this steps is shown. The pure polymer must be dispersed in the solvent, avoiding the formation of clusters. Once the polymer is dispersed, the solvent migrates slowly inside the bulk, until the chains are totally surrounded by solvent. Then, the chains are able to move freely in the solution. If the concentration of polymer is high enough, the possibility that two chains enter in contact and interact increase; then they form a network that modify the rheological behavior of the solvent which is observed by a change in viscosity (increase or reduction) and the presence of elasticity. The forces involved in the interaction of such chains are just *dispersion forces* that are usually weak.

One way to increase the interaction forces among the polymeric chains is by grafting hydrophobic groups in their backbone. The hydrophobic groups stick together and form clusters that increase the total joints in the solution and the contribution to the final rheological behavior. This kind of polymers are called *associative polymers* and are widely used because are able to modified the rheological behavior of the solutions at smaller concentrations than typical soluble polymers(Kastner,2001).

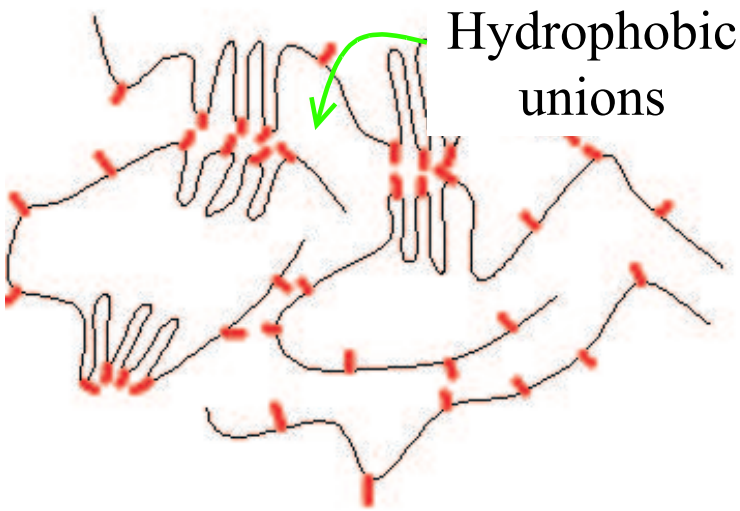

Figure 1.11: Schematic representation of a linear polymer grafted with hydrophobic groups.

1.3 Surface properties

Previous sections of this thesis dealt with macroscopic properties through a continuum approach. However, it is important to recognize that such behavior is a consequence of the materials microscopic nature. In nature it is possible to find four distinct forces. Two of them are strong and weak interactions that act among elementary particles such as neutrons, protons, electrons and others. The other two forces are electromagnetic and gravitational interactions that act among atoms, molecules and elementary particles. The first pair of forces are a short range interactions, less than 10^{-5} nm. The second pair are effective over a larger range of distances, from subatomic to astronomical distances, and are responsable of the macroscopic behavior of matter.

It is possible to explain the properties of solids, liquids and gases through electromagnetic interactions. Astronomical behavior and tidal motion can be explained with gravitational forces. When these two forces work simultaneously are the cause of several phenomena, for example, liquid rising between nearly closed walls or in small capillaries.

In this section a brief explanation about surface tension, interfacial ten-

sion and some surface chemistry is presented. These issues will be relevant to explain the terminal velocity discontinuity in the terminal rising bubble problem.

1.3.1 Surface energy or surface tension

In nature, stable forms are those with minimal energy, for example, liquids tend to adopt shapes that minimize their surface area, keeping the minimum number of molecules at the surface. Sphere is the geometry with less surface-volume ratio, for this reason, bubbles and droplets tend to be spherical. However, there may be other forces that modify this ideal shape, for example, gravity flatten spheres into spheroidal shapes.

From a thermodynamical point of view, the free energy change to separate unit areas between two media (1 and 2) from contact to infinity (in vacuum) is called *work of cohesion* W_{11}; when both media are identical and *work of adhesion* W_{12} when those media are different.

Surface energy or *surface tension* γ is the free energy change when a surface area of a medium is increased by an unit area. Such process is equivalent to separating to half-unit areas from contact, so *surface tension* is given by

$$\gamma_1 = \frac{1}{2} W_{11} \tag{1.25}$$

γ is given in units of energy per unit area and is commonly given in Jm^{-2}. However, in the case of liquids γ_1 is given in units of tension per unit length Nm^{-1}. In the Table 1.3, values of the surface tension for some liquids is presented.

The intermolecular forces responsable of *surface tension* are the same as those that determine *latent heat* and *boiling point*. Figure 1.12 shows the decreasing of surface tension in water with temperature. It is important to mention that impurities tend to reduce surface tension. Actually, this property is used to

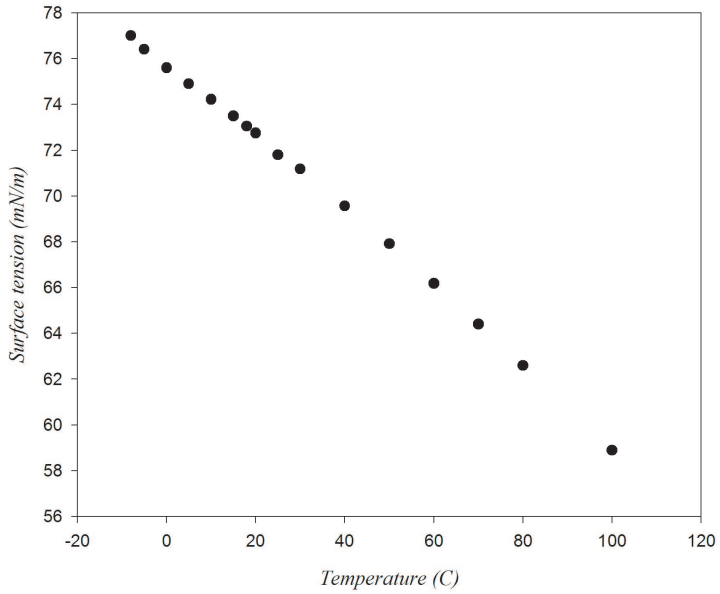

Figure 1.12: The variation of the surface tension of water with temperature

Table 1.3: Surface and interfacial energies (mN m^{-1})

Liquid	Surface energy γ_1	Liquid-liquid interface γ_{12}	Interface Energy
Chloroform	27	chloroform-water	28
Octane	21.8	Octane-water	51
Ethylene glycol	48	Ethylene glycol-tetradecane	20
Water	72	Tetradecane-water	53
Mercury	472		

characterized water purity. When surface tension is determined in a foreign vapor, the effect is lowering γ from its value in vacuum. For example, when mica is cleaved in high vacuum the surface energy is around $3500 mJm^{-1}$, but when cleaved in humid laboratory air it falls to $300 mJm^{-1}$. This is the principal reason of the different behavior of bubbles in clean and in contaminated water.

There are several techniques to determine *surface tension*. A universal method especially suited to check surface tension over long time intervals is the *Wilhelmy plate method*. A vertical plate of known perimeter is attached to a balance, and the force due to wetting is measured.

1.3.2 Interfacial energy or Interfacial tension

Recall from the previous section where interactions between molecules inside each fluid resulted in a given viscosity. Now, consider two immiscible liquids. At the interface between the liquids there will be interactions between molecules of different type and the *interfacial tension* arises due to the attractive forces between the molecules in the different fluids. Generally, the interfacial tension of a given liquid surface is measured by finding the force across any line on the surface divided by the length of the line segment. Thus, the interfacial tension becomes a force per unit length which is equal to the energy per surface area γ_{12}. This property can be calculated with the equation:

$$\gamma_{12} = \frac{1}{2}W_{11} + \frac{1}{2}W_{22} - W_{12} = \gamma_1 + \gamma_2 - w12 \tag{1.26}$$

where W_{11} and W_{22} are the cohesion works for each liquid, and W_{12} is the adhesion work, defined as the reversible work required, per square centimeter, to separate both liquids.

Chapter 2

Methods and materials

In this chapter the basic techniques, methods and materials are described.

2.1 Equipment and characterization

The experiments were conducted in a cylindrical setup with a proper arrangement to release freely bubbles. Video and photographs were acquired with a *high speed camera* (Kodak Motion Corder Model 1000) and with a *digital camera* (Fuji FinePix S1Pro, 6 Megapixels). Bubble velocities, volume and geometrical parameters were determined through digital image processing. The rheological properties were measured in a cone and plate *rheometer* (Rheolyst AR-1000N by TA Intruments). The velocity fields were measured using a standard *particle image velocimetry* technique (Dantec Dynamics, PIV), with fluorescent particles. Surface tension was measured by a Wilhelmy scale with a *DuNouy ring* model 700 (Sigma). A description and details of this techniques are given below.

2.1.1 Experimental device

To analyze the motion of air bubbles in a liquid, the experimental device presented in figure 2.1 was used. A certain known volume of air was placed in

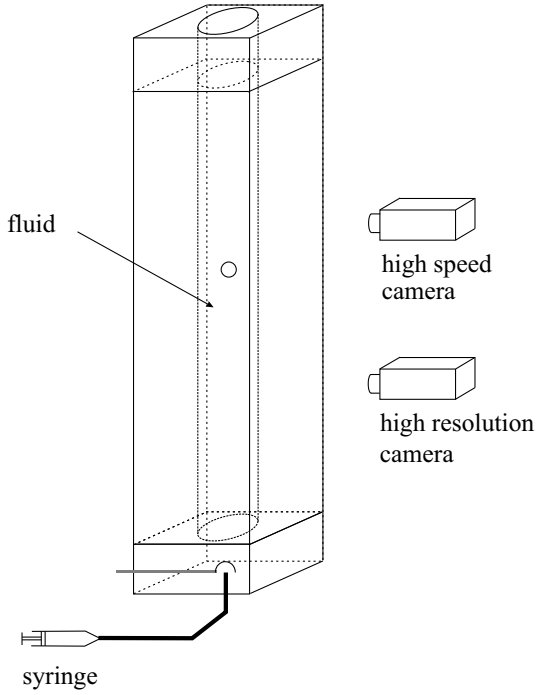

Figure 2.1: Experimental device to study the motion of air bubbles rising freely in a liquid. A square shell filled with the inner liquid is used to avoid reflections. Two cameras (a high speed one and a high resolution one) are included.

a hemispherical glass cap with a syringe; by turning the cap, the bubble was released to move upwards in the test section. The test section is a cylindrical tube with an internal diameter of $9cm$ and a length of $60cm$. The width of the tube was large enough to neglect wall effects and its length was long enough to let the bubbles reach their terminal velocity. The cylindrical tube was placed inside a squared container. To reduce the refraction effects, the cylinder and the square section were filled with the test fluid. Different fluids were tested and their rheological properties are shown below. It has been suggested that the velocity of the bubbles can be dependent on the injection frequency (Rodrigue,De Kee and Chan Man Fong, 1996); therefore, at least a five minutes interval was left between two consecutive bubbles to avoid this effect.

2.1.2 Viscosity

In general, *viscosity* is a measure of the resistance of a fluid to deform under stress. The viscosity depends on flow characteristics. The measured viscosity can be *apparent* and *viscometric*. The apparent viscosity is measured under inhomogeneous flow (where the shear rate is not constant). It implies that the flow is complex and the value of viscosity is not always reproducible. However, due to their practicality and simplicity a wide variety of arrangements producing inhomogeneous flows are used. They are useful reference or control values. In this work, the *fall of bead arrangement* was used. *Viscometric* measurements are carried out under homogeneous flow conditions (constant shear rate), which are confident and reproducible; one example is the *shear viscosity*. Experimental details of both methods are presented in the next sections.

Fall of bead viscosity

When a spherical particle falls or rises freely in a liquid, it reaches a steady state in which the sum of all the forces involved in the movement is zero. Then is easy to determine the *fall of bead viscosity*. The viscosity is given by the expression:

$$\mu = \frac{R^2(\rho_s - \rho)g}{18v_\infty} \tag{2.1}$$

where R is the sphere radius, ρ is liquid density, ρ_s is sphere density and v_∞ is the terminal velocity. This equation is only valid for small Reynolds numbers ($Re < 1$) and small ratios between sphere and container diameter ($D_s/D_c < 0.1$).

Couette flow and simple shear

This type of flow is characterized by the action of boundaries with relative motion. The classical example of this flow is that between two infinite and parallel planes, one of which remains motionless and the other moves shearing

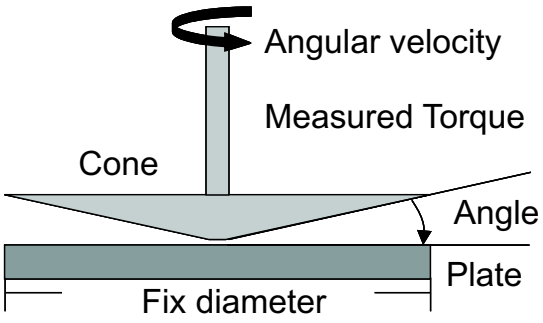

Figure 2.2: Cone and plate geometry.

the fluid. This is called *plane couette flow*. Some approximations to Couette flow are available and widely used, among those, *coaxial cylinders*, *parallel plate* and *cone and plate* are found.

In this work a *cone and plate geometry* was used as it produces a nearly homogenous flow in the test section. Figure 2.2 shows a schematic representation of this geometry. The correspondent shear rate $\dot{\gamma}$, shear stress τ_{12} and viscosity μ are given by the relations;

$$\dot{\gamma} = \frac{\Omega(t)}{\alpha} \tag{2.2}$$

$$\tau_{12} = \frac{3T\alpha}{2\pi R^3} \tag{2.3}$$

$$\mu = \frac{\tau_{12}}{\dot{\gamma}} = \frac{3\alpha T}{2\pi R^3 \Omega} \tag{2.4}$$

where α is the cone angle, Ω is the angular velocity, R is the radius of the geometry and T is the applied torque.

With this geometry is also possible to determine the *first normal stress difference* by the equation:

$$N_1 = \frac{2F_{thrust}}{\pi R^2} \tag{2.5}$$

where F_{thrust} is the total thrust the fluid applies vertically on the plate. The

shear rates which are accesible to this geometry are between 10^{-4} to 10^{2}, at higher rates some instabilities appear and the flow becomes inhomogeneous.

For all the experiments a $40mm$ $1°59'14''$ steel cone with a truncation gap of $46\mu m$ and a plate fixture with a Peltier temperature-control system was used.

2.1.3 Surface tension

The *surface tension* σ was measured with a Du Noüy ring setup coupled with a Wilhelmy fixture. Wetting properties of the surface or interface have little influence on this measuring technique. Maximum pull exerted on the ring by the surface is measured. All determinations were carried out at room temperature and repeated three times, the error among the several determinations was less than 3%. The values were given in mNm.

2.1.4 Visualization techniques

From flow visualization several properties of motion of bubbles can be obtained. In this section, the conditions and digital treatment to determine *velocity*, *volume*, *morphology* and *flow field* are described.

Velocity determination

The bubble velocity was measured with a high speed camera. The camera records up to 4000 frames/s, and follows the motion of bubbles. In figure 2.3 two images taken at various times are shown. The time between images is known and the displacement can be measured determining the change in position of the bubble and with the equivalence between pixels and millimeters. To guarantee that the bubble has reached its terminal velocity an space-time diagram was generated. In figure 2.3, two of this diagrams are presented. The first one is for a bubble moving steadily; there the position-time line is straight

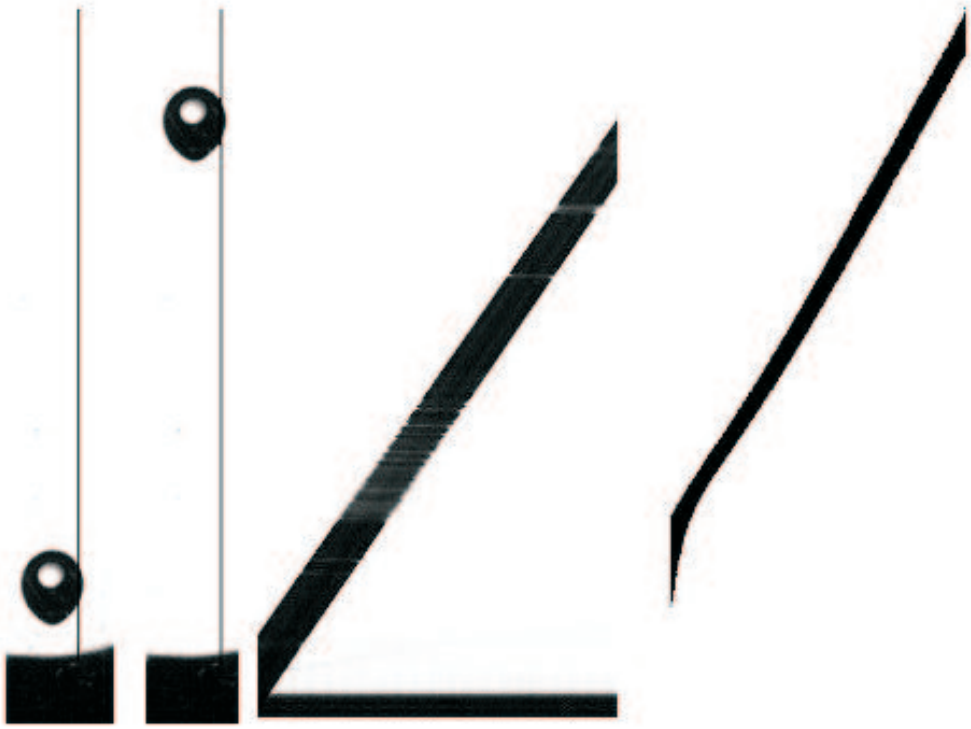

Figure 2.3: Space-time diagrams. From left to right: bubble at time 1 (the line shows the column of pixels selected to created the diagram), bubble at the final stage, space-time diagram for a bubble terminal velocity and space-time diagram for a transient motion.

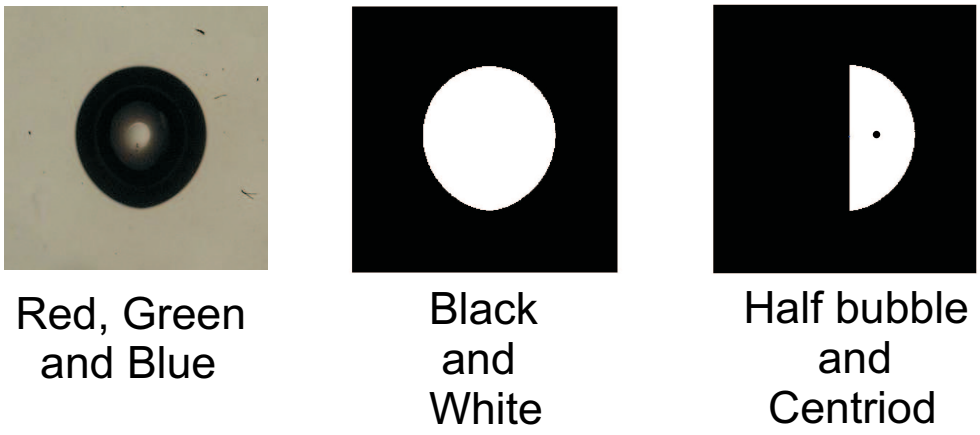

Figure 2.4: Volume digital determination. From left to right: Photograph of a bubble in RGB format, black and white image converted from the RGB and image result from a threshold applied.

and the velocity can be obtained measuring the slope. The second diagram is for a bubble in a transient state (start-off). It is possible, in this case, to obtain the velocity calculating the slope at every position. The calibration was carried out setting a sphere in the bubbles path. Then, the pixels by unit length are measured.

Volume and morphology

When a bubble is released in a fluid, it is important to control its volume. However, its not practical to inject a known air volume in the experimental device, because the bubble can be broken into small bubbles. Then, an approximated volume was injected and the volume was calculated by a subsequent digital analysis of a bubble image. This method is described in Figure 2.4. To obtain this images, a back light illumination was used; it traces the outline of the bubble. Such picture was converted into a *black and white format* and a proper threshold analysis was applied. Then, a bidimensional and axisymmetric bubble was generated. The centroid and area of this half bubble were

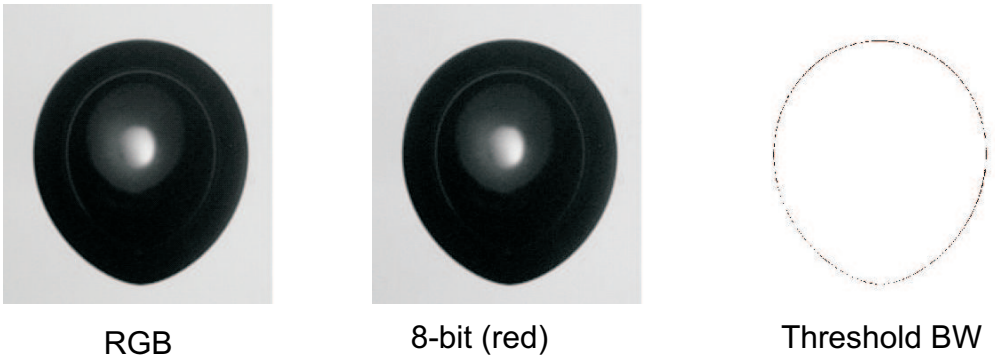

Figure 2.5: Bubble profile digital process. From left to right: RGB picture, 8-bit picture (red) and bubble profile after threshold processing.

calculted. The volumen was found using *Pappu´s centroid theorem* given by

$$V = 2A_m d_c \tag{2.6}$$

where V is the bubble volume, A_m is the area of the middle bubble and d_c is the distance from the simmetry axis to the centroid of the middle area.

The morphology of a bubble can be studied obtaining the coordinates of its profile. The general steps to acquire such profile are shown in figure 2.5. From a RGB picture a 8-bit image was splitted. In general, the red component has the best definition due to the light source. Then, a threshold analysis was applied and the contour was defined. Finally, the coordinates of the contour were obtained.

Velocity field

A *particle image velocimetry* (PIV) system with two 532nm lasers and one CCD camera (Dantec Dynamics) was used to measure the flow field around a bubble. Figure 2.6 (left) shows the experimental setup. The fluid is seeded with fluorescent particles, which, for the purposes of PIV, are generally assumed to faithfully follow the flow dynamics. It is the motion of these seeding particles that is used to calculate the velocity field. When the laser sheet illuminates the testing area, the particles scatter the light revealing their position and a

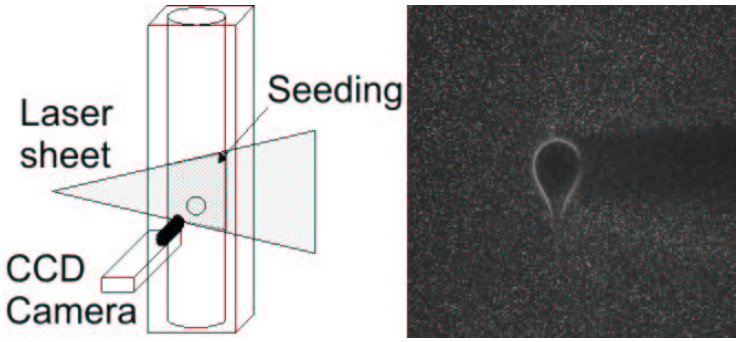

Figure 2.6: Experimental device and PIV arrangement (left). Typical seeding field of view for a bubble moving in a HASE fluid (right)

first photograph was taken (figure 2.6 right). After a period of time, a second photograph was taken. In this study, this time delay was $20,000\mu s$. The flow field is determined from the two images and the domain is divided in several interrogations areas. The spatial fields were transformed to Fourier space and the correlation function is evaluated. Then, considering the spatial field and the time between photographs, an average vector is built for each section. Finally, the complete vector field is obtained, as seen in Figure 2.7. This method allows to determine the complete velocity field for a 2D region without disturbing the flow.

2.2 Materials

Although the principal fluid are a HASE-type (see next section), several others with widely different properties were considered. All solutions were prepared at room temperature. Samples where left to settle 48hrs to guarantee the complete solubility and swelling. Thereafter, surface tension and rheological characterization were performed.

The fluids used are summarized in the Table 2.1, disclosing rheological data. In the following sections a complete description and liquid properties

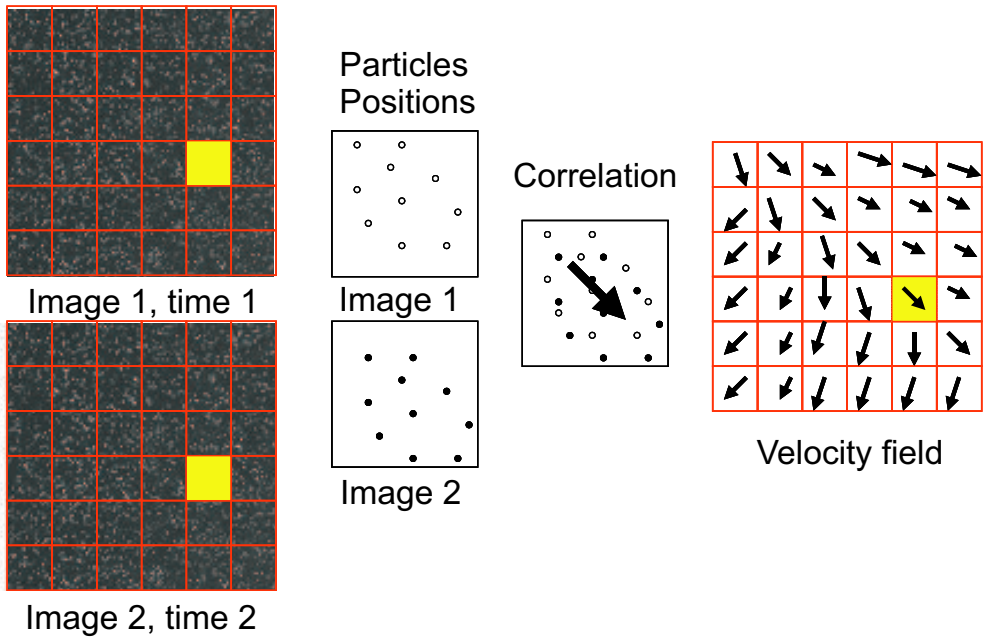

Figure 2.7: An schematic representation of the PIV procedure. From left to right: Two images taken at different times of the seeding field divided in interrogation areas, position of particles for a selected interrogation area, superposition of both interrogation areas with the resulting velocity vector and the final velocity field.

Table 2.1: Fluids summary

Fluid caption	Description	Rheological behavior
FluidH	Associative polymer in water solution	Shear thinning, but with a region of constant viscosity where the normal stresses are important
Fluid1	Aqueous viscoelastic fluid	Shear thinning and elastic
Fluid2	Non-aqueous viscoelastic fluids	Viscoelastic
Fluid3	Constant viscoelastic fluids	Constant viscosity and normal stresses
Fluid4	Shear thinning inelastic fluids	Shear thinning and inelastic

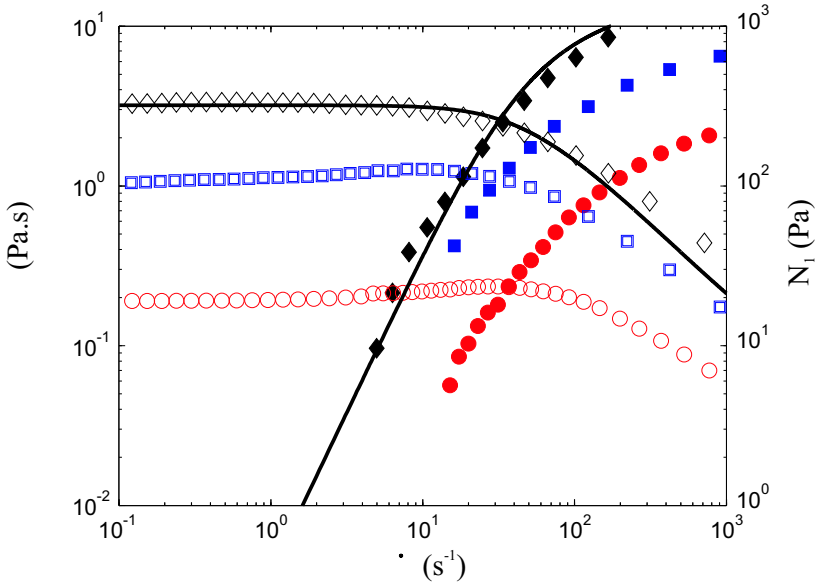

Figure 2.8: Shear viscosity (empty symbols) and first normal stress difference (filled symbols) as a function of the shear rate for different concentrations of HASE. (○) 1.2 %; (□) 1.5 %; (◇) 1.7 %. The bold lines show predictions of the Bautista-Manero model for 1.7 % of HASE (Bautista, 1999).

are shown.

For the case of viscoelastic fluids, the measured first normal stress difference and shear viscosity were fit to a power law: $N_1 = a\dot{\gamma}^b$, $\eta = m\dot{\gamma}^n$. The values of the coefficients a, b, m and n, as well as their range of validity and surface tension are also reported in Tables 2.2, 2.3, 2.4, 2.5 and 2.6. All fluids were chosen such that their shear viscosity would be of the same order of magnitude as those fluids in which the bubble velocity discontinuity had previously been observed.

2.2.1 HASE fluids

HASE (*hydrophobic alkali swellable emulsion*)Primal TT-935 is supplied by Rohm and Haas. It is an associative polymer obtained in a suspension, 30% wt. at a pH of 3. Aqueous solution in distilled water were prepared at 1.2, 1.5, and 1.7% by weight. At low pH HASE is not soluble, becoming soluble for a pH higher than 6. If the pH is increased hydrophobic interactions are

Table 2.2: Properties of the HASE aqueous solutions: viscosity μ, surface tension σ, and coefficients a and b in the expression of the first normal stress difference, $N_1 = a\dot{\gamma}^b$.

Fluid	$\%HASE$	μ Pas	a	b	range $\dot{\gamma}$ s^{-1}	σ mNm^{-1}	d(mm) mm	$\overline{\dot{\gamma}}$ s^{-1}
H-1	1.2	0.22	0.2078	1.3097	0.1-100	38.41	0.3-9.4	1-42
H-2	1.5	1.14	1.1449	1.3192	0.1-100	36.93	3.3-7.6	2-16
H-3	1.7	3.34	2.3728	1.3289	0.1-50	55.55	2.5-8.7	1-10

increased too. Consequently the viscosity increases up to a pH about 9 at which the viscosity reaches its maximum. Above this pH value the viscosity levels-off or decreases. To adjust the pH to 9 an alkaline 0.5 M solution of 2-amino,2-methyl propanol (AMP supplied by Aldrich) was used.

Once the solutions were left free of bubbles, the rheological behavior and surface tension properties were determined (Table 2.2). Figure 2.8 shows the rheological behavior of HASE solutions under shear flow. The HASE solutions tested behave as Newtonian fluids at small shear rates. Viscosity remains constant and normal stresses are negligible. From 0.1 to 50 s^{-1}, the normal stresses are measurable while the viscosity remains almost constant. For all concentrations, a slight shear thickening behavior can be observed for small ranges of shear rate. For large shear rates and depending on the concentration, the fluids exhibit a shear-thinning behavior.

2.2.2 Other fluids

Aqueous viscoelastic fluids

These liquids are aqueous polyacrylamide (PAA) solutions. They were prepared slowly mixing of an aumonunt of PAA in a mixture of 50 wt.% water and 50 wt.% glycerin. Different percentages of PAA were studied: $0.05wt.\%$, $0.1wt.\%$, $0.15wt.\%$ and $0.2wt.\%$. As can be seen in figure 2.9, the PAA solutions are both shear thinning and viscoelastic. The viscosity and the first normal stress difference increase with PAA content. The surface tension decreases

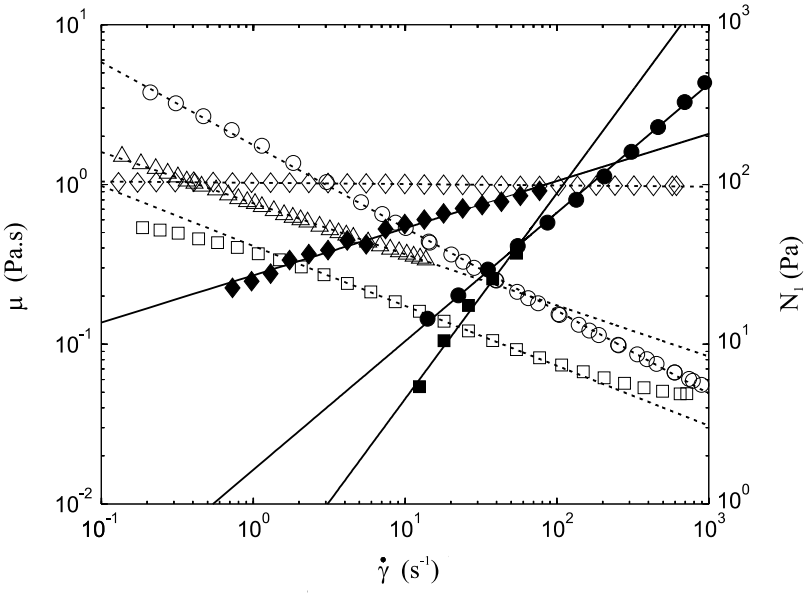

Figure 2.9: Shear viscosity (empty symbols) and first normal stress difference (filled symbols) as a function of the shear rate for different liquids: (○) fluid 2: aqueous viscoelastic fluid (PAA = 0.2%), (□) fluid 3: non-aqueous viscoelastic fluid (PAA = 0.1%), (◇) fluid 4: Boger fluid (PAA =0.1%), fluid 4: shear thinning fluids (0.1 wt. % Carbopol and 0.08 wt.% of triethylamine). The lines represent the power law fit given by the tables 1.3, 1.4, 1.5 and 1.6.

Table 2.3: Properties of solution 1 (50 wt.% of water + 50 wt.% of glycerine + 0.05-0.2 % of PAA).

Fluid	PAA %	a	b	m	n	range of $\dot{\gamma} s^{-1}$	σ (mNm_{-1})	d (mm)	$\overline{\dot{\gamma}}$ s^{-1}
1-1	0.2	1.6390	0.805	1.7666	-0.5156	0.1-200	58.81	2.5-6.1	2-30
1-2	0.15	1.6192	0.7683	0.5625	-0.4571	0.1-80	92.6	2- 2.5	3-35
1-3	0.1	1.771	0.6712	0.3993	-0.4523	1-80	101.58	3-5.7	9-50
1-4	0.05	1.7296	0.5967	0.201	-0.3475	10-100	113.16	2.6-6.7	22-71

slightly with an increase in PAA content. This liquid was chosen because several authors have reported the appearance of the velocity discontinuity (Leal, Skoog and Acrivos, 1971; Rodrigue, De Kee and Chan Man Fong, 1996; Rodrigue, De Kee and Chan Man Fong, 1998; Rodrigue and Blanchet, 2002; Herrera-Velarde et al., 2003). The properties of this fluid are shown in the Table 2.3.

Table 2.4: Properties of solution 2 (ethyleneglycol + 0.05-0.3 % of PAA).

Fluid	PAA %	a	b	m	n	range of $\dot{\gamma}$ s^{-1}	σ (mNm_{-1})	d (mm)	$\overline{\dot{\gamma}}$ s^{-1}
2-1	0.3	0.2101	1.5003	1.6644	-0.4655	0.1-100	48.19	2-6.3	0.8-11
2-2	0.15	0.1248	1.3188	0.7032	-0.4127	1-100	86.41	2.4-7.4	8-27.6
2-3	0.1	0.2352	1.2882	0.4125	-0.3751	5-100	85.23	2.8-8.3	11-34
2-4	0.05	0.2560	1.0675	0.1691	-0.2915	5-100	87.85	3-10.5	14-44

Non-aqueous viscoelastic fluids

To test if the bubble velocity discontinuity can be observed also for non-aqueous viscoelastic solutions, several runs were performed using ethyleneglycol as the base for the solution. These solutions are mixtures of ethyleneglycol and PAA. Different PAA contents were studied: 0.05 wt.%, 0.1 wt.%, 0.15 wt.% and 0.3 wt.%. As can be seen in figure 2.9, the PAA solutions are viscoelastic. The viscosity and the first normal stress difference increase with PAA content, but the surface tension decreases (Table 2.4).

Constant viscosity fluids

To investigate if the phenomenon of the bubble velocity discontinuity could be observed in the absence of shear thinning effects, a series of fluids of the Boger type (elastic with constant viscosity) were tested. These solutions were composed of glycerol (Drogeria Cosmopolitan) and small quantities of PAA (0.05 wt.%, 0.1 wt.%, 0.2 wt. %). As presented in Figure 2.9, these fluids are viscoelastic, but the viscosity is not strictly a constant with the shear rate. The viscosity and the first normal stress difference increase with PAA content, and the surface tension slightly decreases (Table 2.5). It was not possible to obtain a low viscosity Boger fluid with the materials considered in this study.

Shear thinning inelastic fluids

To complete our parametric study, we consider the case of fluids in which elastic effects are absent but shear thinning effects are important. These flu-

Table 2.5: Properties of solution 3 (glycerine + 0.05-0.2 % of PAA).

Fluid	PAA %	a	b	m	n	range of $\dot{\gamma}\ s^{-1}$	σ (mNm_{-1})	d (mm)	$\overline{\dot{\gamma}}$
3-1	0.2	6.8058	0.7023	1.1407	-0.0362	0.1-100	108.33	5-10.5	1-3
3-2	0.1	26.988	0.2952	1.0232	-0.0081	0.1-100	111.44	5.7-19.7	2.6-8
3-3	0.05	17.186	0.208	0.9717	-0.0092	0.1-100	112.74	5.7-19.6	4.3-14

Table 2.6: Properties of solution 4 (ethylenglycol + carbool + triethylamine).

Fluid	$Carbopol$ $wt.\%$	$triethyl-$ $aminewt.\%$	m	n	range of $\dot{\gamma}\ s^{-1}$	σ (mNm_{-1})	d (mm)	$\overline{\dot{\gamma}}$ s^{-1}
4-1	1	0	2.8462	-0.5771	0.1-100	90	4.2-19.7	3.8-27.8
4-2	0.1	0.08	0.7635	-0.3198	0.1-100	86.51	4.2-19.7	22.6-34.3
4-3	0.1	0.1	1.4179	-0.4392	0.1-100	86.51	4.2-24.3	9.4-31.7

ids were obtained mixing ethylenglycol with Carbopol (Polygel CA supplied by 3V). Different concentrations of Carbopol were studied: 1 wt.% and 0.1 wt.%. Due to the fact that the Carbopol is not complete soluble at low pH in ethylenglycol, some drops of triethylamine were added to increase the pH level and to dissolve the Carbopol. These liquids behave essentially as power law fluids (Fig. 2.9). The viscosity level increases with the concentration of Carbopol and with triethylamine. The surface tension increases with Carbopol content, but is not affected by the presence of triethylamine (Table 2.6).

Chapter 3

Experimental Results

In this chapter the experimental measurements of bubble velocity, size and shape are presented, first for the HASE fluids and then for the other fluids. The velocity discontinuity is not observed in all the examined fluids. Furthermore, some comments and observations are given to present the experimental results analyzed in the following Chapter. The chapter dealt with methods and materials. A list of the liquids is presented in Table 2.1.

The liquids named *HASE fluids* show an interesting rheological behavior. Their viscosity remains constant for the rates of deformation at which the bubbles rise, and exhibit considerable normal stresses in this region. Then, it is possible to isolate the presence of normal stresses and the change in viscosity separately. This behavior is the key of the proposed explanation for the necessary conditions to observe the velocity discontinuity. Besides the volume-velocity dependence and the morphology of the bubbles, the velocity fields around the bubbles are shown for this fluid. For the others fluids, the flow fields are similar, and hence they are omitted.

3.1 Falling bead or shear viscosity

Recalling the solutions for a Stokes and Hadamard regimes shown in chapter 1, the equations for the terminal velocity for both conditions are:

$$v_\infty = \frac{R^2(\rho_s - \rho)g}{18\mu} \tag{3.1}$$

$$v_\infty = \frac{R^2(\rho_s - \rho)g}{12\mu} \tag{3.2}$$

It is relevant to figure out the correct viscosity to calculate the terminal velocity in Hadamard and Stokes regime. For this, experimental determinations of both viscosities are compared. It has been shown (McKinley, 2002) that *for moderate Deborah Numbers (De), wall effects appear to be less important than in the motion of the corresponding Newtonian fluid.* In our experiments, the Deborah number lies between 0.5 and 1.6, implying that the drag correction factor is smaller than the one calculated in the case of a Newtonian fluid (Chhabra,1981). In these HASE solutions, a $\frac{r}{R}$ value of 0.07 corresponds to $K_N(\frac{r}{R}) = 1.16$. It implies a viscosity increase of 1.16. Moreover, the wall correction factor for elastic, constant-viscosity fluids (Chhabra,1988) is given by $f(\frac{r}{R}) = 1 - 0.17\frac{r}{R}$ for Deborah numbers larger than 0.2, which corresponds in our case to $K_N(\frac{r}{R}) = 1.006$. The wall effect contributes to a small increase in viscosity obtained from falling-bead experiments over that obtained in simple shear.

In the background section, a discussion on the flow around a sphere was presented. In summary, the fluid domain can be divided in three regions: a simple shear region at the equator, a simple extensional region at the rear, and a biaxial extensional region at the front of the bubble. The extensional components lead to extra stresses that slow down the sphere motion, and

Table 3.1: Viscosity measurements for different solutions with two methods: $\mu_{rheometer}$ is the viscosity measured in a cone-plane rheometer under simple shear, μ_{fall} is the viscosity calculated from falling-bead experiments. The ratio of the viscosity α decreases with increasing HASE concentration

Fluid	$HASE$ %	$\mu_{rheometer}$ Pas	μ_{fall} Pas	Viscosity ratio α
1	1.2	0.22	0.49±0.01	2.23
2	1.5	1.14	1.58±0.04	1.39
3	1.7	3.34	4.08±0.23	1.22
4	2.1	12.5	13.23±0.4	1.06

this extensional flow depends on the Reynolds number. For large values of the Reynolds number, the extensional components will be more important; as a consequence, the difference between the two viscosities will increase. So, in addition to the wall effects, which decrease the terminal velocity and hence increase the viscosity, it is necessary to include the extensional flow contributions. The ratio of the viscosity estimated from falling-bead data to the viscometric viscosity decreases with HASE concentration (3.1). Under extensional flow, models (Manero et al, 2002, Belmonte, 2002, & Boek et al, 2005) predict a region of extensional thickening at extension rates of the order of the inverse of the main relaxation time. This region coincides with the onset for measurable normal stresses in shear flow, closely related to the appearance of the velocity discontinuity.

The extensional flow contribution further retards the motion of the falling bead, increasing the mentioned viscosity ratio. The experimental and theoretical results obtained with the two viscosity measurements are compared, and results are presented in Figure 3.1. For small bubbles that are almost spheroidal, the experimental measurements lie between the two limiting cases of Hadamard and Stokes laws with a viscosity calculated from the falling-bead experiments. Therefore, the bubble interface can be considered neither fully contaminated nor clean. We note that the comparison is good for bubbles

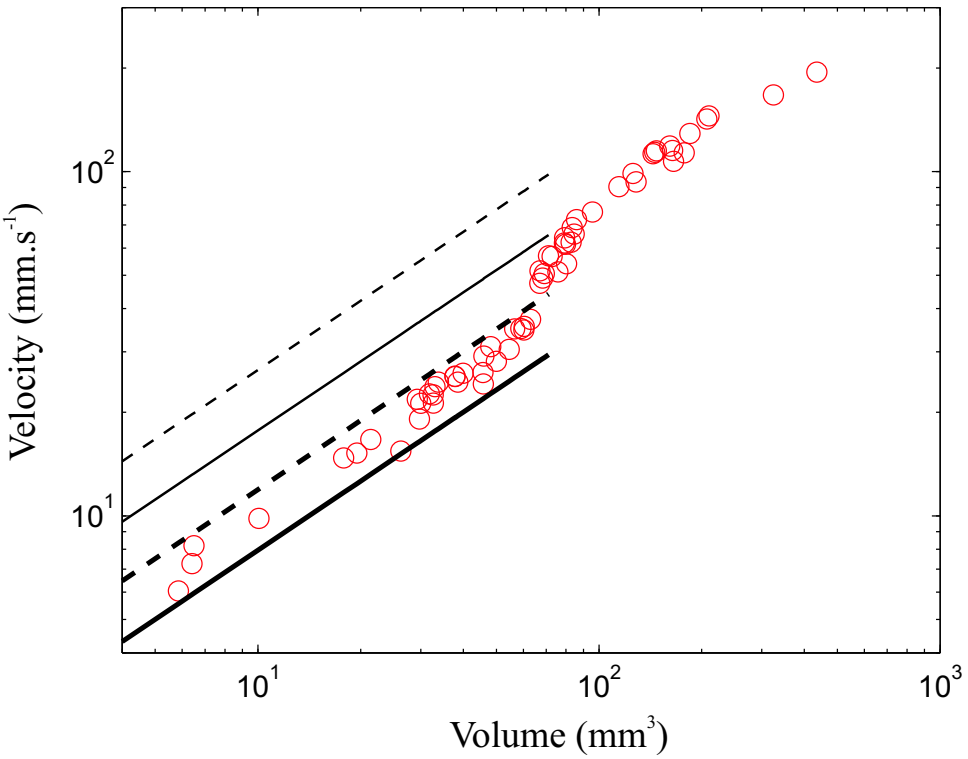

Figure 3.1: Bubble velocity as a function of bubble volume, 1.2 % HASE. The lines are the theoretical predictions obtained from the Stokes (continuous lines) and Hadamard (dashed lines) laws: (thin lines) $\mu = \mu_{rheometer}$; (thick lines) $\mu = \mu_{fall}$.

with volumes smaller than the critical volume V_c. The results for the other fluids and their comparison with the theory are not presented here, but the agreement between theory and experiments is equally good. Contrary to the measurement of the viscosity by falling-bead experiments, the simple shear rheological measurements do not take into account the uniaxial and biaxial deformations. This explains why the behavior of small bubbles rising in a viscoelastic fluid is better described using a falling-sphere measurement of the viscosity.

3.2 Terminal velocity and Morphology for HASE fluids

In this section a discussion on the terminal velocity, velocity discontinuity, flow field around bubbles and shape of the bubbles is presented for HASE fluids. HASE solutions behave as Newtonian fluids at small shear rates, viscosity remains constant and normal stresses are negligible. For large shear rates and depending on the concentration, the fluids exhibit a shear-thinning behavior: the viscosity decreases with the shear rate and the first normal stress difference increases with the shear rate. In general, for a given shear rate, the viscosity and the first normal stress difference increase with HASE concentration, and the critical value of the shear rate at which normal stresses appear decreases with increasing HASE concentration.

Shape and critical volume

Figure 3.1 shows the plot terminal velocity versus volume for a HASE solution $1.2wt\%$. It is clear that a discontinuity is observed a some critical volume ($V_c \approx 65mm^3$). The correspondent shape of bubbles for selected volumes are presented in the Figure 3.2. A characteristic behavior can be described as

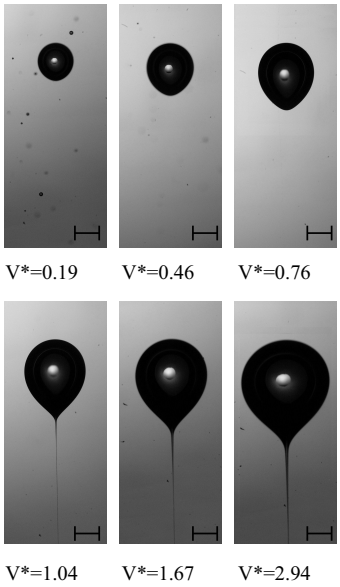

Figure 3.2: Bubble shapes for different values of the dimensionless volume $V^* = V/V_c$ for HASE =1.2 %, with $V_c = 65mm^3$. The small bubbles are almost spherical. For larger volumes (for $V* > 1$), the shape of the bubbles is concave with a very thin and long tail at the rear part of the bubble. The scale represents 2 mm.

a function of V_c. For bubbles with a volume much smaller than the critical volume Vc, the shape is spheroidal. With a small increase in volume, a slight deformation on the rear part of the bubble is observed. In all cases, for volumes smaller than Vc, the shape of the bubbles is convex all around, whereas for bubbles with a volume larger than the critical volume, the shape is concave in the trailing end: the shape presents an inflection point.

Figure 3.3 shows a comparison of the shape of a bubble before and after the jump. The shape in the front region is nearly the same, whereas it changes significantly in the back region. Moreover, the formation of a sharp cusp can be clearly observed. At the tip of the cusp, a long (few centimeters) and very thin (tens of micrometers) tail forms in all cases. Using two cameras acting simultaneously, it was possible to obtain a view of the tail from two sides. The cusps and tails immediately after Vc are axisymmetric. However, for volumes larger than Vc, this is no longer the case. Nonaxisymmetric tails are shown and discussed later.

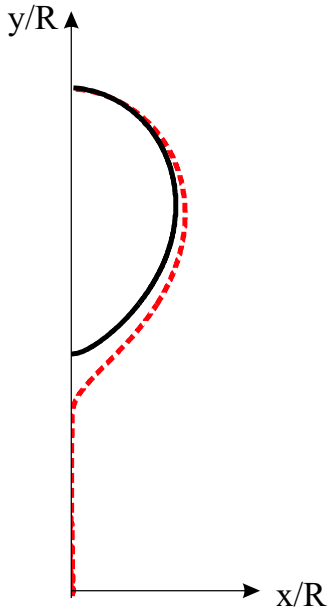

Figure 3.3: Bubble shapes before (continuous line) and after (dashed line) the discontinuity. The shape does not change in the front part of the bubble, whereas it changes in its back part ($V_{before} = 49.2mm^3; V_{after} = 61.2mm^3; 1.5\% HASE$)

The plots terminal velocity versus volume for the three HASE fluids are shown in Figure 3.4. The general observations and remarks are the same for the different concentrations. Furthermore, the bubble shapes for 1.5 and 1.7% of HASE are presented in Figures 3.5 and 3.6

Shear rate and discontinuity

It is possible to link this behavior with the rheological properties of the fluid. For this, the mean shear rate (defined as $\overline{\dot{\gamma}} = U/r$)at which the normal stresses are measurable and at which the discontinuity of the velocity occurs, is determined. Figure 3.7 shows the calculated $\overline{\dot{\gamma}}$ for the three tested liquids.

From this plot, the value of the shear rate corresponding to the critical volume can be determined and is approximately the same as the shear rate at which the elastic nature of the fluid begins to manifest itself (N_1 becomes

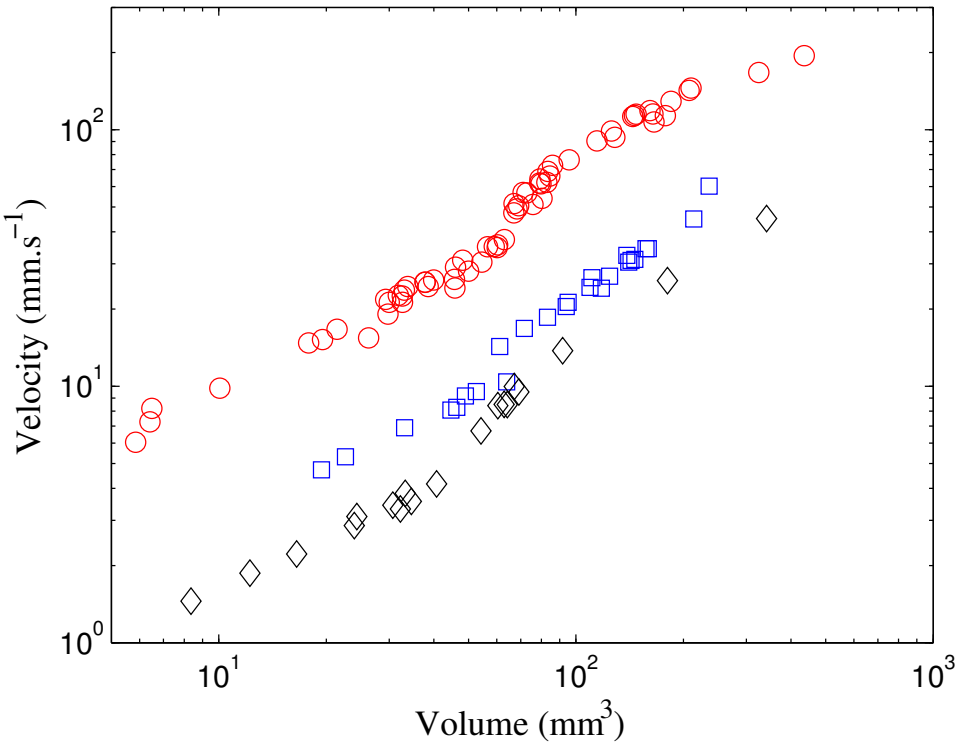

Figure 3.4: Bubble velocity as a function of bubble volume for different HASE contents: ∘ 1.2 %; □ 1.5 %; ⋄ 1.7 %. There is a discontinuity of the bubble velocity for volumes equal to V_c(1.2% : $V_c \simeq 65\ mm^3$; 1.5% : $V_c \simeq 60\ mm^3$; 1.7% : $V_c \simeq 50\ mm^3$). The critical volume decreases with an increase in HASE concentration.

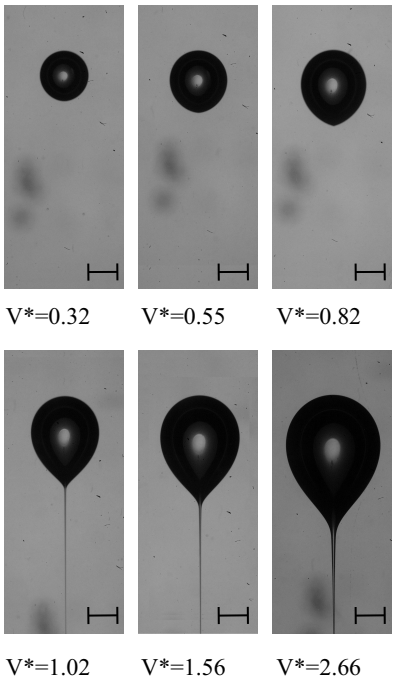

Figure 3.5: Bubble shapes for different values of the dimensionless volume $V^* = V/V_c$ for HASE =1.5 %, with $V_c = 60mm^3$. The scale represents 2 mm.

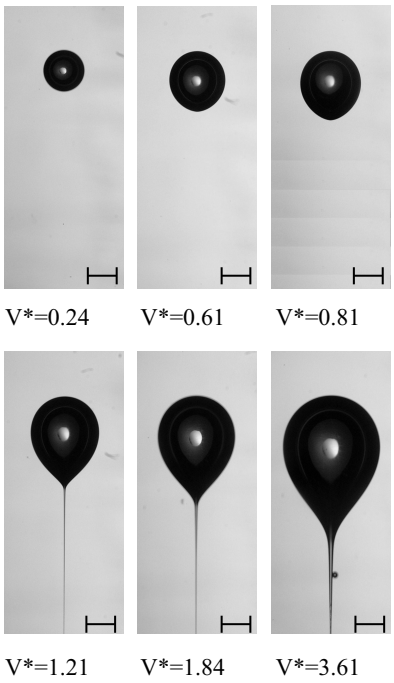

Figure 3.6: Bubble shapes for different values of the dimensionless volume $V^* = V/V_c$ for HASE =1.7 %, with $V_c = 50mm^3$. The scale represents 2 mm.

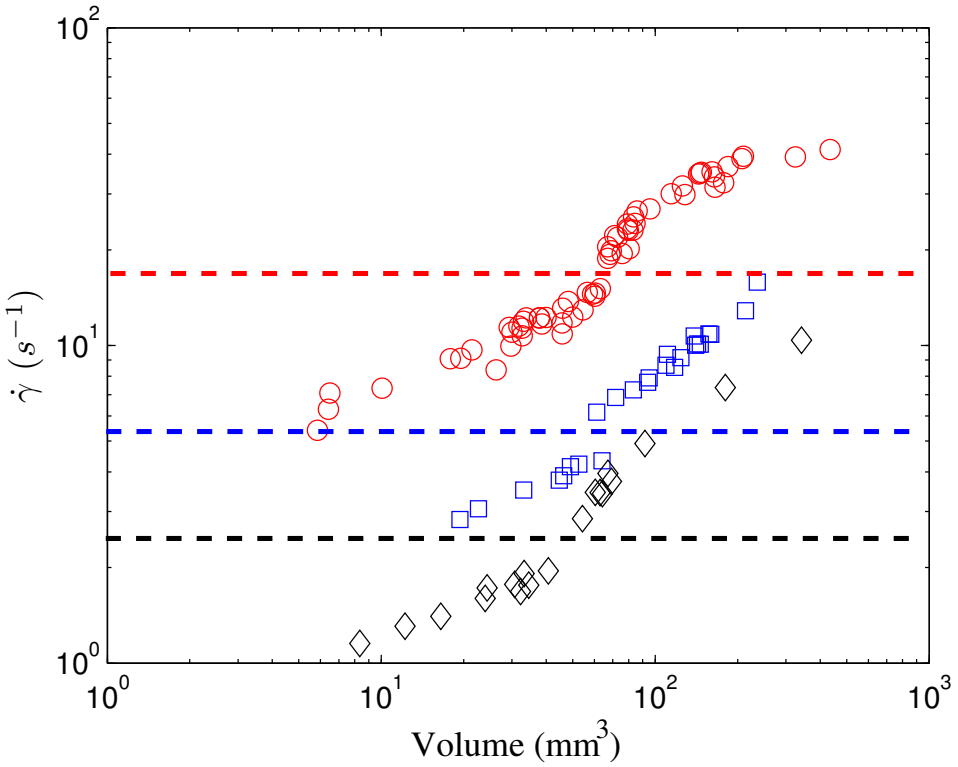

Figure 3.7: Mean shear rates $\overline{\dot{\gamma}}$ as a function of volume for various HASE contents: ∘ 1.2 %; □ 1.5 %; ⋄ 1.7 %. The dashed lines represent, for each HASE concentration, the shear rate at which the normal stresses are measurable.

measurable). Therefore, the bubble velocity discontinuity is a direct result of the appearance of elastic stresses. For negligible normal stresses, the bubbles are spheroidal and their velocities agree reasonable well with the Stokes and Hadamard laws. For significant normal stresses, the velocity is larger than that predicted by Stokes and Hadamard law, and the bubbles are concave, presenting a tail at their rear part. The immediate consequence of the presence of normal stresses in the liquid is a change in the bubble shape, which evidently leads to a drag reduction and, hence, a rapid increase of velocity. A particular bubble shape is then related to its rising velocity. This important evidence will be recalled in the chapter of dimensionless analysis.

Negative wake contribution

Flow visualization around bubbles before and after the discontinuity using the PIV technique are presented in Figures 3.8 and 3.9. For air bubbles with volumes smaller than the critical one, the fluid at the front and at the rear of the bubble is moving in the same direction of the bubble (see figure 3.8). For bubbles with a volume larger than the critical one, the flow around the bubble is drastically different (figure 3.9). The flow at the front of the bubble is in the same direction of the bubble motion. At the rear of the bubble, the fluid is moving in the opposite direction of the bubble motion. This phenomenon is called negative wake and was previously reported elsewhere (Funfschilling, 2001, Hassagar, 1979, Bisgaard et al, 1982, and Li et al, 2001). More recently Herrera et al, 2003 propuse that the negative wake is a manifestation of importance of the elastic effects in the bubble motion and found that the appearance of the negative wake is related with the discontinuity. It is important to remark that the elasticity of the liquid is an important factor for the discontinuity to appear. This argument will be further discussed later.

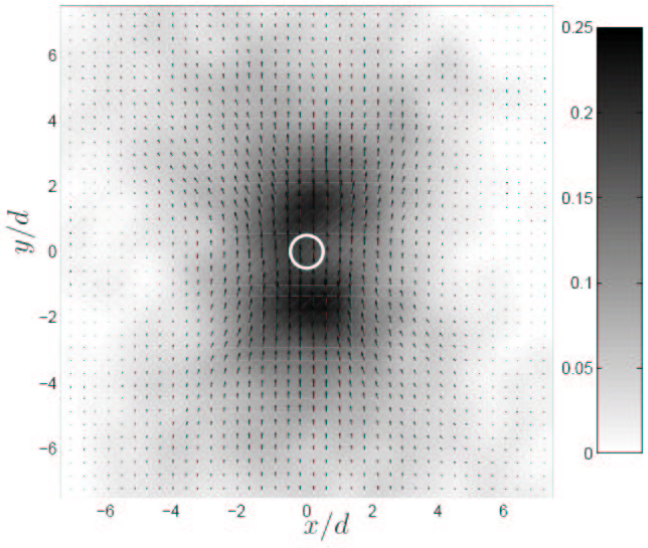

Figure 3.8: Flow around a rising bubble with volume below the critical one (V=4.2 mm^3 ; U=1.1 mm s^{-1} ; HASE 1.5 %)

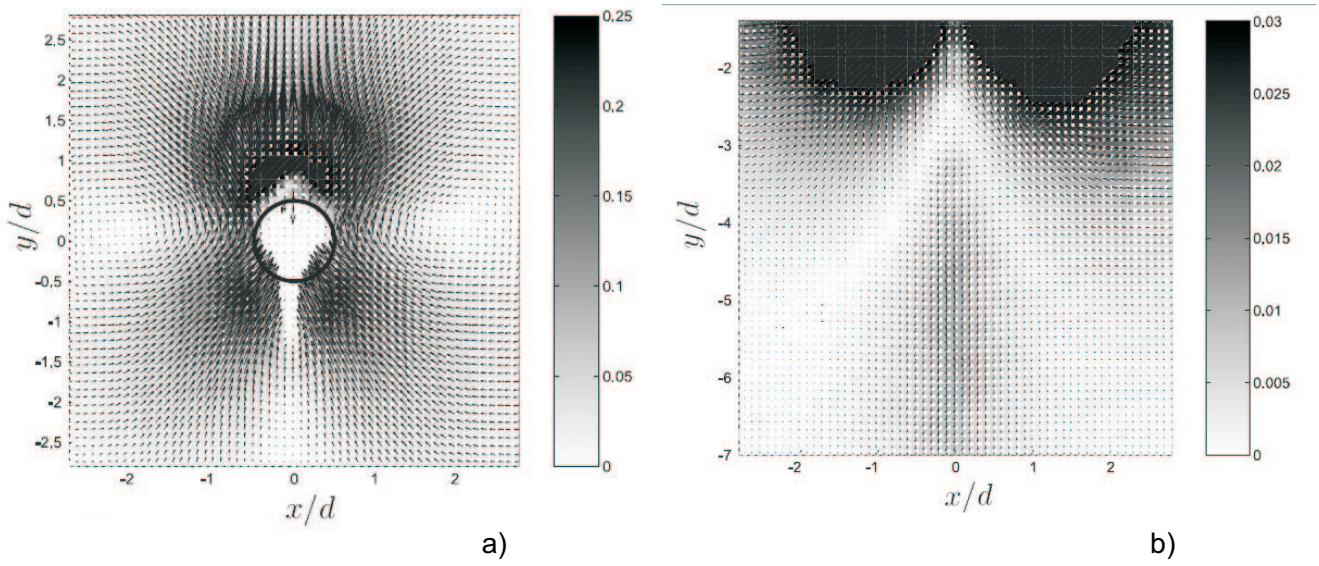

Figure 3.9: Flow around a rising bubble with volume above the critical one. a) Flow around the bubble. The flow is very similar to the flow observed for a bubble with a volume smaller than V_c. b) At the rear part of the bubble, the negative wake can be seen. $V = 239mm^3$; $U = 54.6mms^{-1}$; HASE 1.5 %.

In the next sections, a similar presentation of results for the other liquids is shown, in order to gather all the experimental evidence for the further dimensionless analysis.

3.3 Other Fluids

3.3.1 Aqueous Viscoelastic Fluids

The fluid composed of $50wt.\%$ of water and $50wt.\%$ of glycerol and PAA is viscoelastic. The relation velocity-volume for a concentration of PAA equal to $0.15wt.\%$ is presented in Figure 3.10. There is a critical value of the volume ($V_c \approx 68.5mm^3$) for which the velocity discontinuity occurs. For this fluid, whatever the concentration of PAA (from $0.05wt.\%$ to $0.2wt.\%$), a critical value of the volume for which a velocity discontinuity occurs exists (figure 3.11). For all PAA concentrations and for small bubbles (with a volume smaller than the critical one), the terminal velocity lies between the two limiting cases of Hadamard and Stokes laws. For percentages of PAA between $0.1wt.\%$ and $0.2wt.\%$, the value of this critical volume decreases with PAA concentration. For small percentages of PAA ($0.05wt.\%$ and $0.1wt.\%$) the critical volume increases with a decrease of PAA. Furthermore and for percentages of PAA larger than $0.1wt.\%$, the slope of the velocity versus volume relation is larger after the discontinuity than before.

It is also possible to relate the discontinuity with the shape of the bubbles. Figure 3.12 shows the bubble shapes corresponding to the terminal velocities, for the case of $1.5wt.\%$ PAA, shown in Figure 3.11. For bubbles with a volume smaller than the critical volume V_c, the bubble shape evolves from spherical to tear-like as the volume increases. It is important to note that, in this case, the bubble shape remains convex (Astarita & Apuzzo, 1965; Zana & Leal,

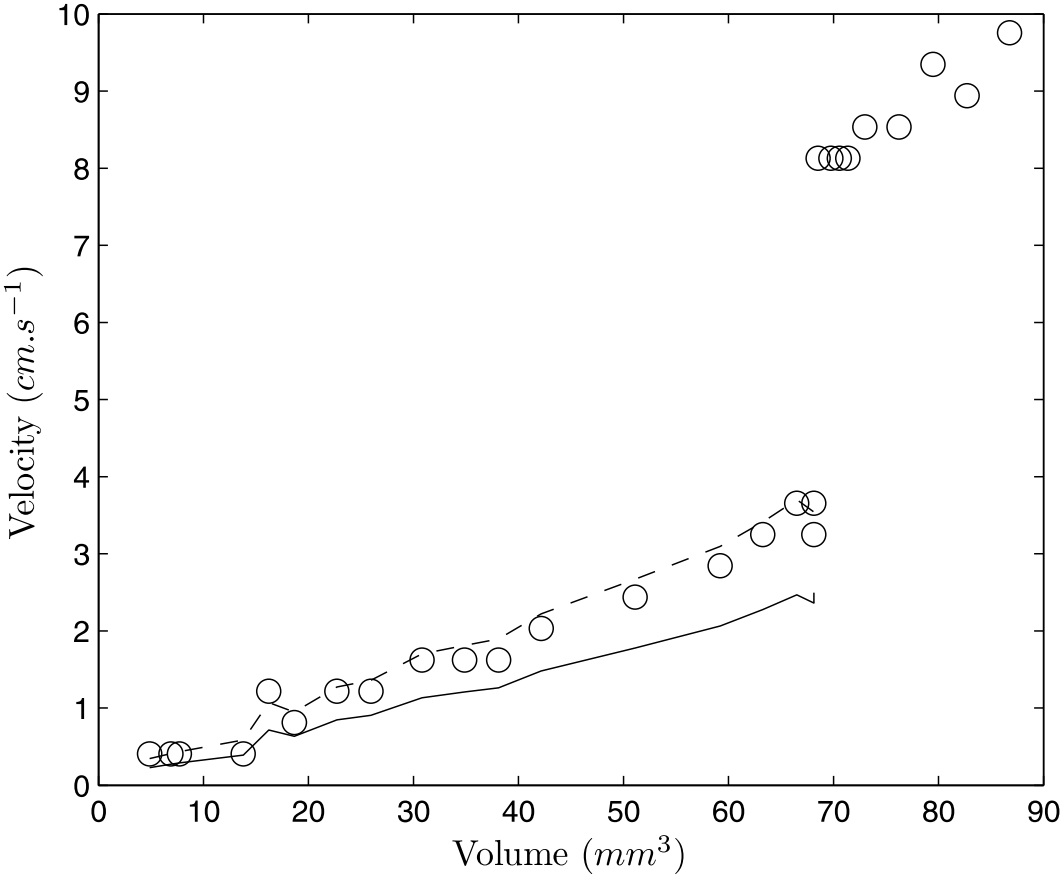

Figure 3.10: Velocity of the bubble as a function of volume. A discontinuity of the velocity can be observed at a volume of $Vc = 68.5mm^3$. The lines are the theoretical predictions obtained from Stokes (continuous line) and Hadamard (dashed line) laws ($\mu = \mu_{fall}$), (50$wt.\%$ water, 50$wt.\%$ glycerol and 0.15$wt.\%$ PAA).

1978). For large bubbles, with a volume larger than Vc, the shape changes from convex to concave. The presence of an inflection point at the rear part of the bubbles can be observed. Also a small cusped "tail" appears. A zoom of the shape of rear part of the bubble at the transition point is shown in Figure 3.13. As the volume of the bubble increases (for sizes larger than $200mm^3$), the shape becomes oblate (horizontal axis larger than the vertical one), but it retains the convex shape with a rear tail. The velocity of bubbles of such large sizes continues to increase monotonically with volume.

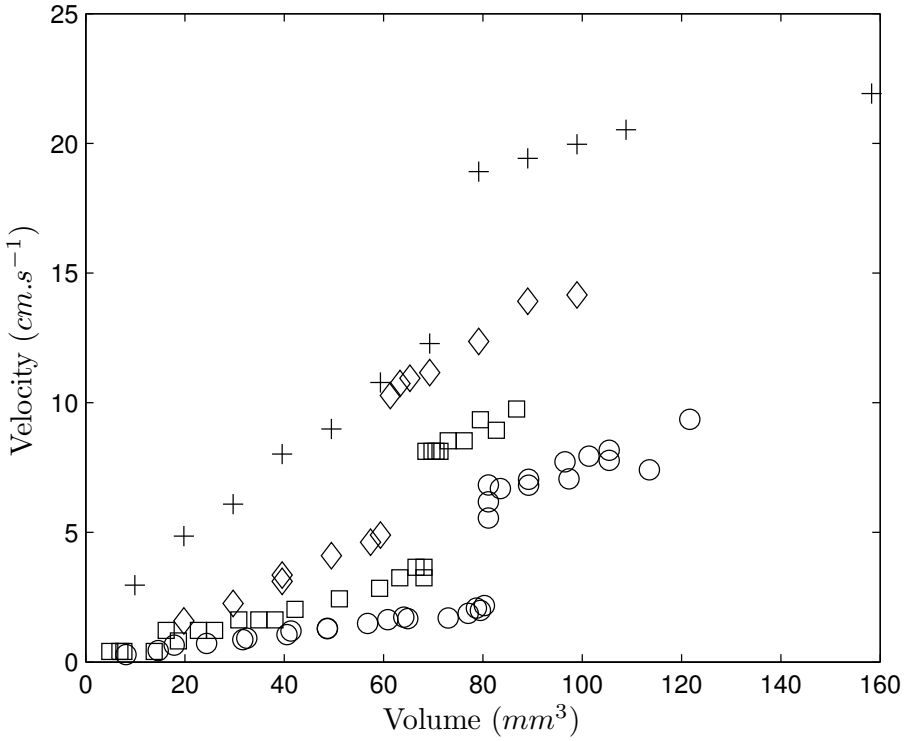

Figure 3.11: Velocity of the bubble as a function of volume for different percentages of PAA : (○) $\%PAA = 0.2$, (□) $\%PAA = 0.15$, (◇) $\%PAA = 0.1$, (+) $\%PAA = 0.05$ ($50wt.\%$ water and $50wt.\%$ glycerol)

3.3.2 Non-aqueous Viscoelastic Fluids

The fluid composed of ethylene-glycol and PAA is clearly viscoelastic. The relation velocity-volume for a concentration of PAA equal to $0.1wt.\%$ is shown in Figure 3.14. Contrary to the previous case, there is no critical value of the volume for which a discontinuity occurs. For bubbles with a volume larger than $90mm^3$ there is a reduction of the slope of the velocity-volume relation. For all the volumes studied the velocity of the bubble lies between the two limiting cases of Stokes and Hadamard. The reduction of the slope for the velocity-volume relation can be associated to the shape of the bubbles. In Figure 3.15, the bubble shapes for this particular experiment are shown. In this case, the bubble shape evolves from spherical to teardrop shape but for nearly all cases the convexity of the shape is retained. For very large bubbles

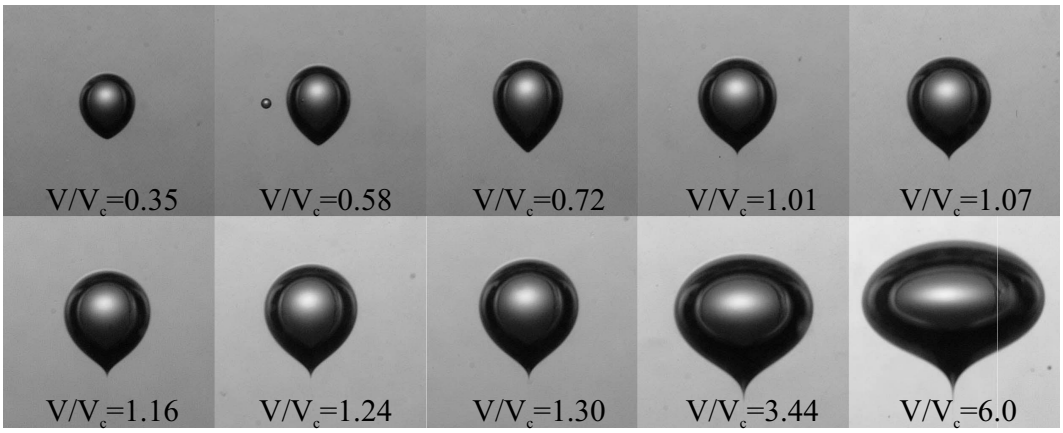

Figure 3.12: Shape of the bubbles as a function of the dimensionless volume (V/V_c with $V_c = 68.5mm^3$). The small bubbles ($V/V_c < 1$), the shape of the bubble is convex. The shape of large bubbles is concave. For large volumes, there is a strong increase of the horizontal diameter ($50wt.\%$ water, $50wt.\%$ glycerin and $0.15wt.\%PAA$)

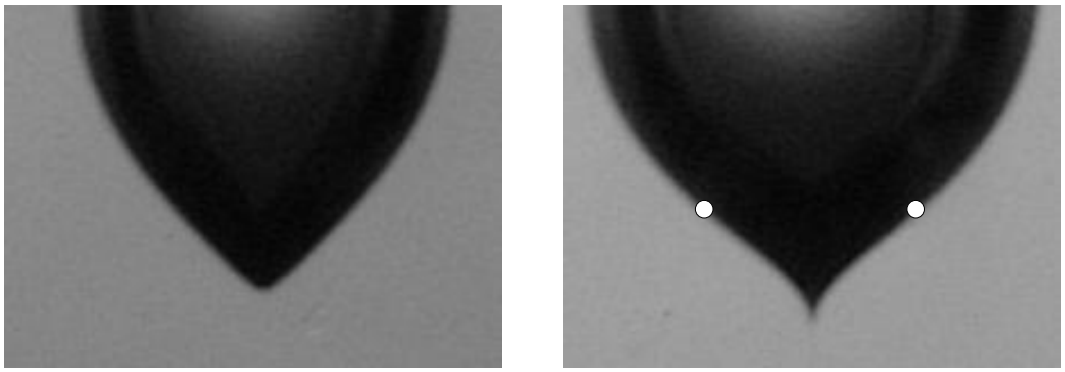

Figure 3.13: Zoom of the rear part of the bubble. The circles show the location of the inflection point where the curvature changes sign ($50wt.\%$ water, $50wt.\%$ glycerin and $0.15wt.\%PAA$).

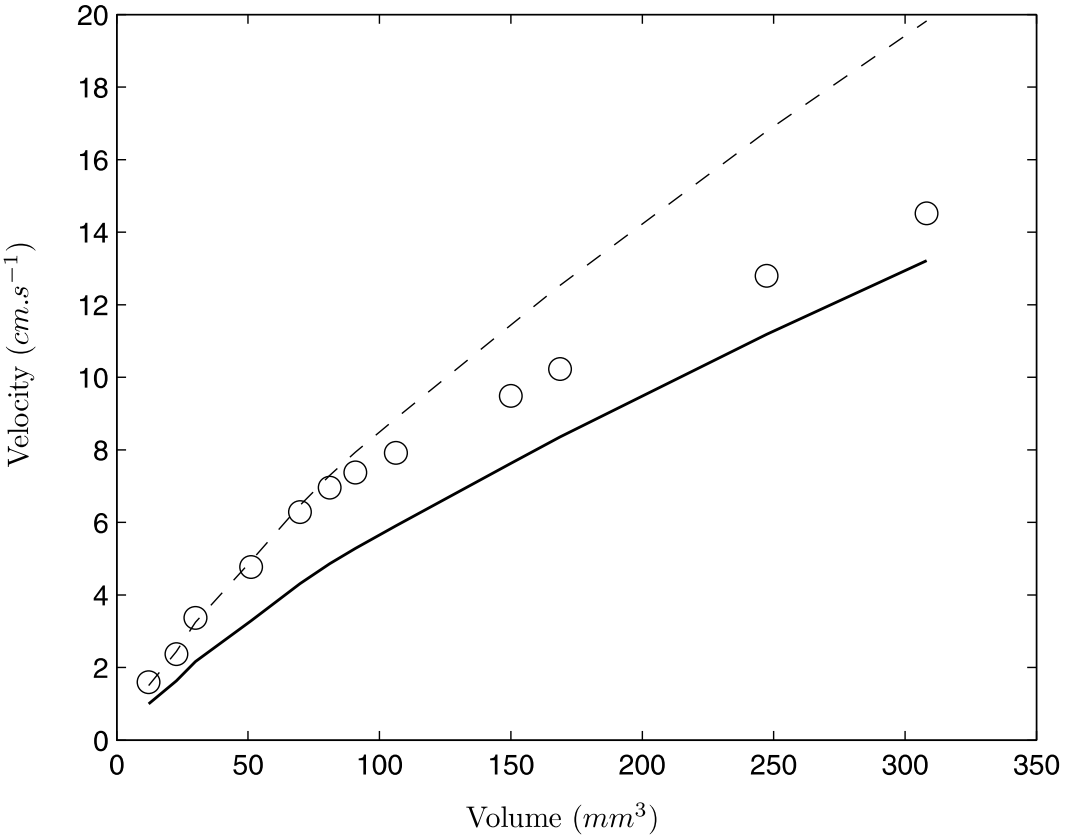

Figure 3.14: Velocity of the bubble as a function of volume. The lines are the theoretical predictions obtained from Stokes (continuous line) and Hadamard (dashed line) laws ($\mu = \mu_{fall}$), (ethylene-glycol at $0.1wt.\%PAA$).

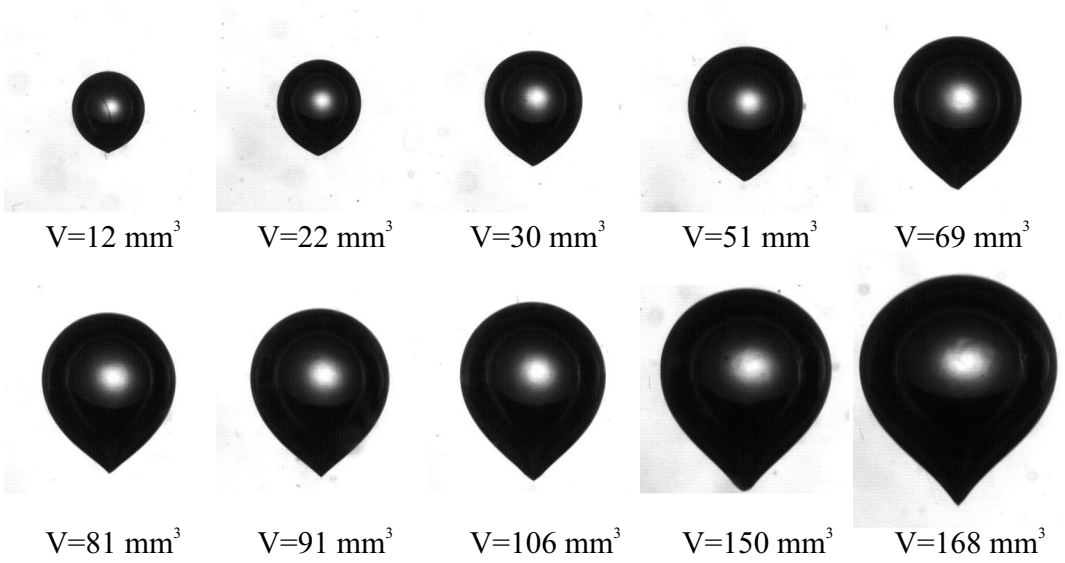

Figure 3.15: Shape of the bubbles as a function of volume. For small bubbles are convex and for large bubbles present an inflection point and we can also notice an increase of the horizontal radius of the bubble with the volume (ethylene-glycol with $0.1wt.\%PAA$).

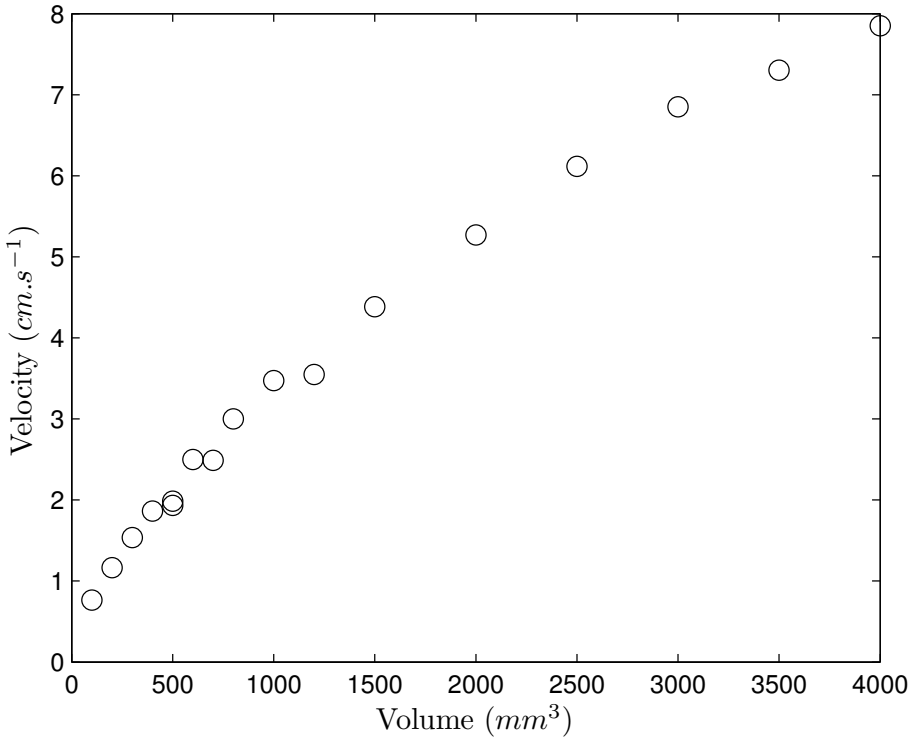

Figure 3.16: Velocity of the bubble as a function of the volume for a Boger fluid. The lines are the theoretical predictions obtained from Stokes (continuous line) and Hadamard (dashed line) laws (with $\mu = \mu_{fall}$), (glycerol + $0.1wt.\%$ PAA).

($V > 150mm^3$), a change of curvature on the rear of the bubble is observed. It must be noted that this convex shape is observed when the bubble shape also became oblate. A cusped tail is not observed in any of the bubbles studied. For other liquids of the same type, similar behavior is observed: no discontinuity of the terminal velocity appears although above certain volume, the slope of the relation velocity-volume decreases significantly. The volume for which the decrease of the slope occurs increases as concentration of PAA decreases.

3.3.3 Boger Fluids

The fluid composed of glycerol and PAA is approximately a Boger fluid: it shows elastic effects with a nearly constant viscosity. The velocity-volume relation for a concentration of PAA equal to $0.1wt.\%$ is shown in Figure 3.16.

There is no critical value of the volume for which a discontinuity of the

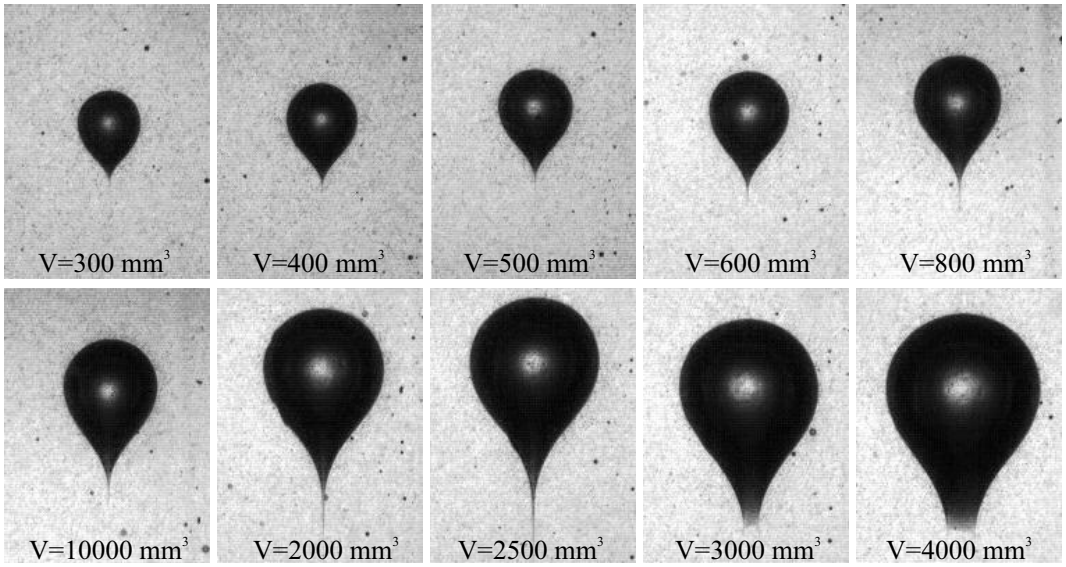

Figure 3.17: Shape of the bubbles as a function of volume. Whatever the value of the volume, all the bubbles are concave (presence of a tail and of an inflection point) (glycerol + $0.1wt.\%$ PAA).

velocity occurs; there is also no significant change of the slope in the relation velocity-volume for large volumes, as seen in the previous cases. The velocity does not lie between the two limiting cases for all volumes studied: the velocity is larger than that predicted by the laws of Stokes and Hadamard. Whatever the bubble volume, the bubble shape does not change significantly: the bubble is concave, there is an inflection point and formation of a tail at the rear part of the bubble, as shown in Figure 3.17. The shape of the tail, however, changes with the bubble volume: for small volumes, the tail is very thin (few microns) and long (few centimeters); for larger volumes, the width of the tail abruptly increases from few microns to few millimeters and may loose its axi-symmetric shape.

For percentages of PAA smaller than $0.2wt.\%$, the behavior is the same: there is no discontinuity of the velocity and no change of the slope for the relation velocity-volume relation. For a percentage of PAA of $0.2wt.\%$, the bubble velocity discontinuity occurs at a volume ($V_c \approx 350mm^3$) but the data, shown in Figure 3.18, are not very conclusive. For this particular case, very few

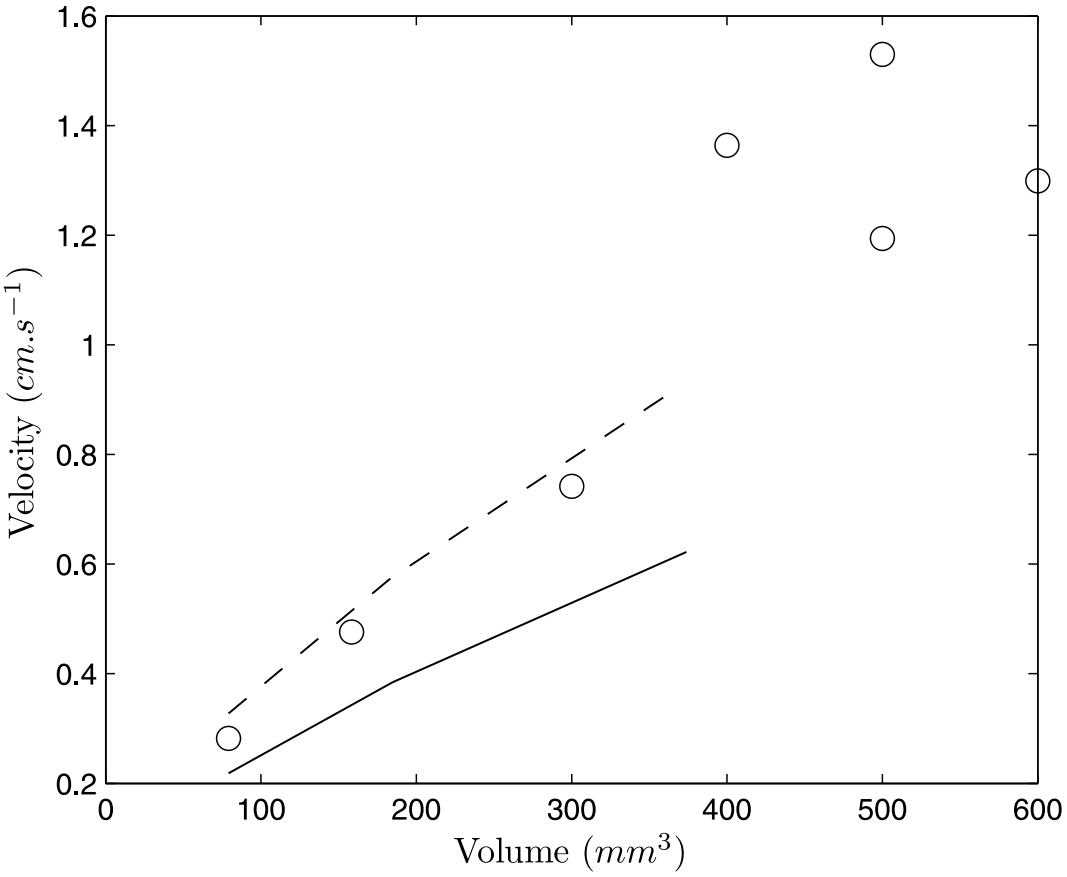

Figure 3.18: Velocity of the bubble as a function of the volume for a Boger fluid. The lines are the theoretical predictions obtained from Stokes (continuous line) and Hadamard (dashed line) laws (with $\mu = \mu_{fall}$), (glycerol + 0.1$wt.\%$ PAA).

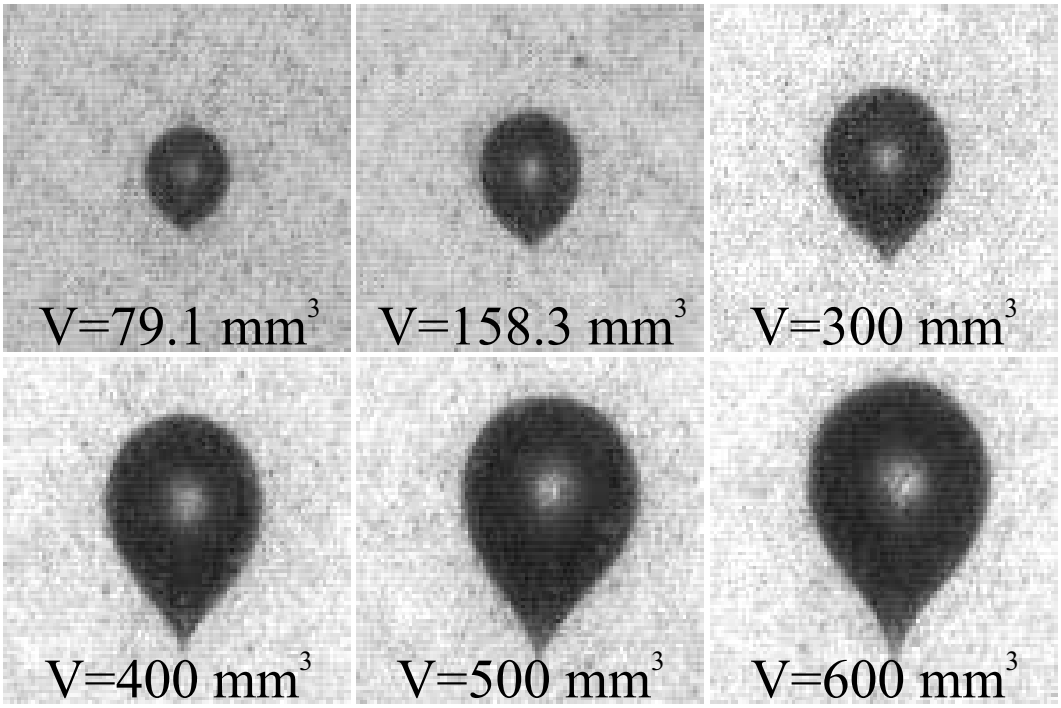

Figure 3.19: Shape of the bubbles as a function of volume. Whatever the value of the volume, all the bubbles are concave (presence of a tail and of an inflection point) (glycerol + 0.1$wt.\%$ PAA).

measurements were possible. Also, the liquid was not very transparent; hence the images are not very clear. For small volumes, the velocity of the bubble lies between the two limiting cases of Stokes and Hadamard. The experimental velocities of bubbles larger than $350mm^3$ are higher than those predicted by the H-R law. In Figure 3.19, the shapes of the bubbles are shown. Although the images are not as clear as in the previous cases, the transition from convex to concave can be observed at the critical volume.

3.3.4 Shear Thinning inelastic fluid

The fluid composed of ethylene-glycol and Carbopol is shear thinning and inelastic. The velocity-volume relation for a concentration of Carbopol equal to 0.1$wt.\%$ and 0.08$wt.\%$ of triethylamine is presented in Figure 3.20.

Clearly, no discontinuity of the velocity-volume relation is observed. For

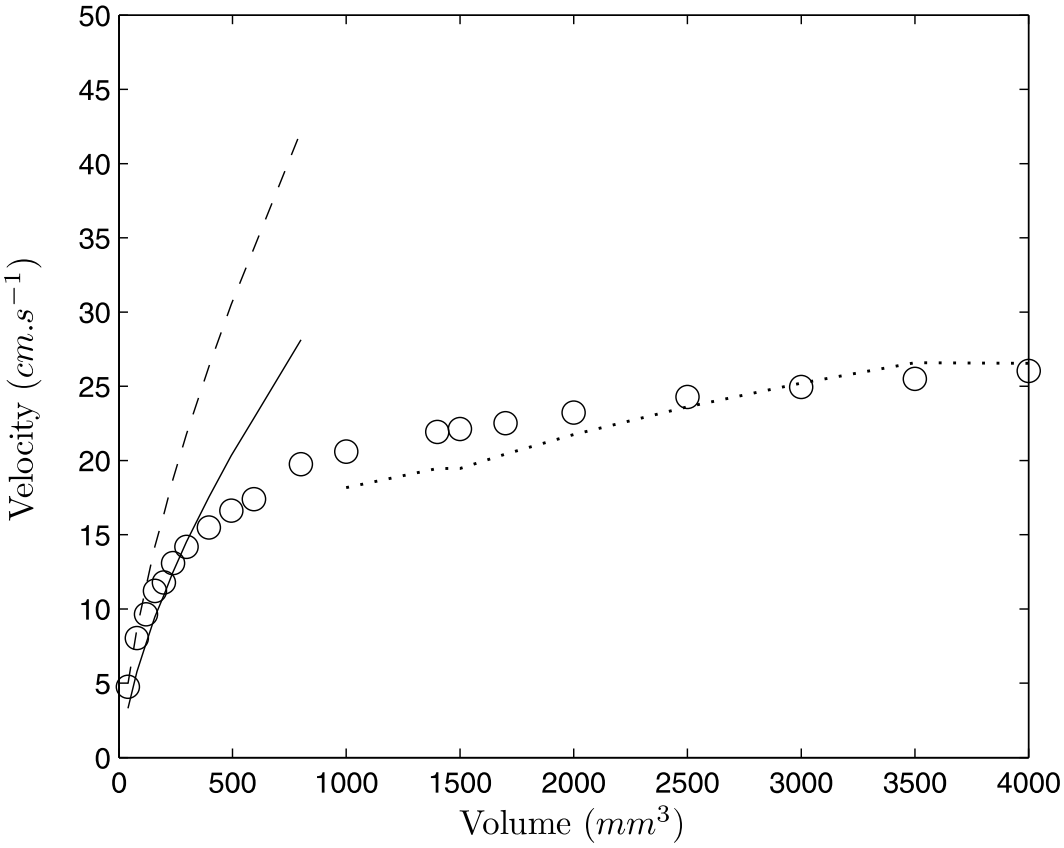

Figure 3.20: Velocity of the bubble as a function of the volume. The lines are the theoretical predictions obtained from Stokes (continuous line) and Hadamard (dashed line) laws (with $\mu = \mu_f all$). The dotted line is the theoretical results obtained by Joseph (2003) (ethylene-glycol + $0.1wt.\%$ Carbopol + $0.08wt.\%$ of triethylamine).

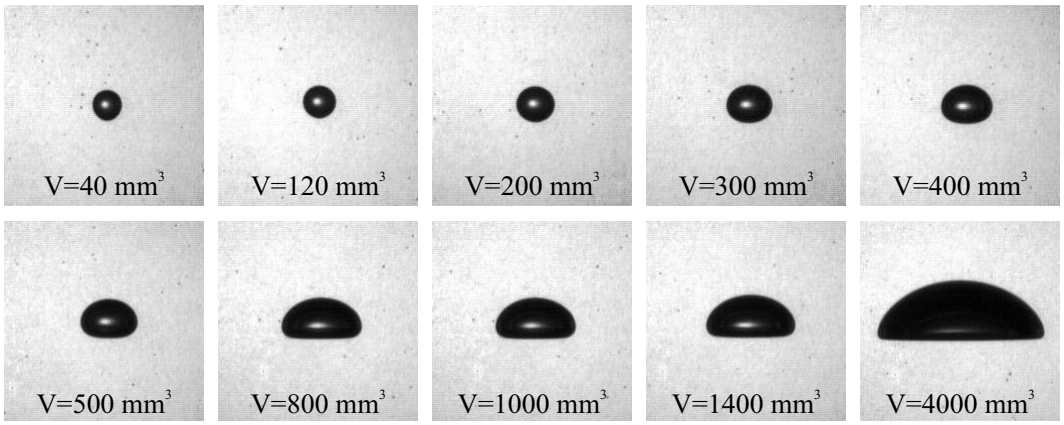

Figure 3.21: Shape of the bubbles as a function of volume. For small bubbles, the shape is spheroidal-convex. The large bubbles are oblate bubbles and a flat part at the rear part appears (ethylene-glycol + $0.1wt.\%$ Carbopol + $0.08wt.\%$ of triethylamine).

volumes larger than $200mm^3$, a decrease of the slope of the relation velocity-volume occurs. For small volumes, the velocity lies between the two limiting cases of Stokes and Hadamard. For large volumes, the velocity is well-described by the theoretical predictions of Joseph (2003). For this class of fluids, there is a value of the volume for which there is a decrease of the slope of the velocity-volume relation. The value of this volume decreases with the percentage of Carbopol and increases with the concentration of triethylamine. As shown in Figure 3.21, for small bubbles, the bubble shapes are spheroidal-convex. As the volume increases, the bubble deforms initially into an oblate shape and then, for very large volumes, into a spherical cap. For all the fluids in this class, the same changes of the shapes are observed. The decrease of the slope of the velocity-volume relationship is clearly related to the change of shape.

3.3.5 Results summary

In conclusion, the experimental results show a wide range of behaviors for bubbles rising in non-Newtonian liquids. A summary of all results is presented here. A velocity discontinuity occurs for aqueous shear thinning viscoelastic liquids, as observed by many authors, and also in Boger fluids for large PAA concentrations. For these two cases, the velocity discontinuity can be related to the change of the bubble shapes from spheroidal-convex to concave with a cusped tail at their rear part. For Boger fluids, with concentration of PAA smaller than $0.2wt.\%$, no discontinuity and no change of the slope occurs. But for this case, all the bubbles, irrespectively of volume, are concave and already show a tail at the rear. For non-aqueous shear thinning viscoelastic liquids and inelastic shear thinning liquids, no discontinuity of the velocity is found. Moreover, the slope of the velocity-volume relationship decreases after a critical value of the volume. This behavior can be related to the change of bubble shape from spheroidal-convex to oblate bubbles or spherical cap (in the case

of a shear thinning inelastic fluid). At this point, the raw experimental data have not provided a sufficient understanding of the phenomenon of the velocity discontinuity. In the following Chapter, a dimensionless analysis approach will be considered for this purpose.

Chapter 4

Dimensionless analysis

The evolution of the bubble shape and the change of the velocity-volume relation whether as a sudden increase (discontinuity) or as a progressive decrease, can be related to the rheological properties of the liquid. In what follows, we analyze the different observed behaviors (velocity discontinuity, decrease of the slope of the velocity-volume relation) in terms of the different forces affecting the bubble motion (viscous, inertia, surface tension and elastic).

One significant characteristic observed at the discontinuity is a change of shape. Hence, let us consider the force ratios affecting the bubble shape. For the case of an air bubble moving in a non-Newtonian liquid, the characteristic forces that will influence the shape are:

- Inertial forces: $\rho U^2 d^2$
- Viscous forces: $\mu U d$
- Elastic forces: $N_1 d^2$ (from shear flow)
- Surface forces: σd

where ρ is the density of the liquid, U is the velocity of the bubble, d is the equivalent diameter of the bubble, μ is the viscosity of the liquid, N_1 is the first normal stress difference and σ is the surface tension. In section 2.3,

we discussed that the characteristic magnitude of the elastic forces for a given experiment could be determined from the rheological characterization of the fluid. The mean shear rate over the bubble $\bar{\dot{\gamma}}$ is used to determine $N_1(\bar{\dot{\gamma}})$. The shape of the bubbles will be determined by the balance between surface tension forces (those that keep the bubble in a spherical shape) and other hydrodynamic forces. For Newtonian fluids, the bubble deformation is determined by the competition between viscous or inertial forces with surface tension forces. If either the Weber number or the Capillary numbers are greater than one, the bubble can be deformed by either inertial or viscous forces respectively. The Weber number is defined as $We = \frac{\rho U^2 d^2}{\sigma}$ and the Capillary number as $Ca = \frac{\mu U}{\sigma}$. The Weber number measures the importance of inertial forces with respect to surface forces. The Capillary number compares viscous forces with surface forces. For the case of viscoelastic fluids, an additional force has to be considered. Since the liquid is deformed as it passes over the bubble, the elasticity manifest itself as a normal stress difference. Hence, we can argue that if elastic effects are present, the shape of the bubble can deviate from spherical if the relation between elastic and surface forces is greater than 1:

$$\Pi = \frac{N_1 d}{\sigma} > 1 \tag{4.1}$$

The Π number can be expressed as the product of the Deborah number and the Capillary numbers: $\Pi \sim De \times Ca$. The Deborah number is usually defined as the ratio of the characteristic time of the fluid t_r to the characteristic time of the flow t_v:

$$De = \frac{t_r}{t_v} \tag{4.2}$$

We can, however, reinterpret this dimensionless parameter as the ratio of elastic to viscous forces:

$$De \sim \frac{N_1}{\mu \bar{\dot{\gamma}}} = \frac{N_1 d}{\mu U} \tag{4.3}$$

For all the experiments, the first normal stress difference N_1 and the viscosity μ are known from the rheometric measurements and the mean shear rate is defined by $\bar{\dot{\gamma}} = U/r$. The surface tension is considered constant for each case. Now, the experimental results for each fluid class will be interpreted in terms of these three characteristic dimensionless numbers.

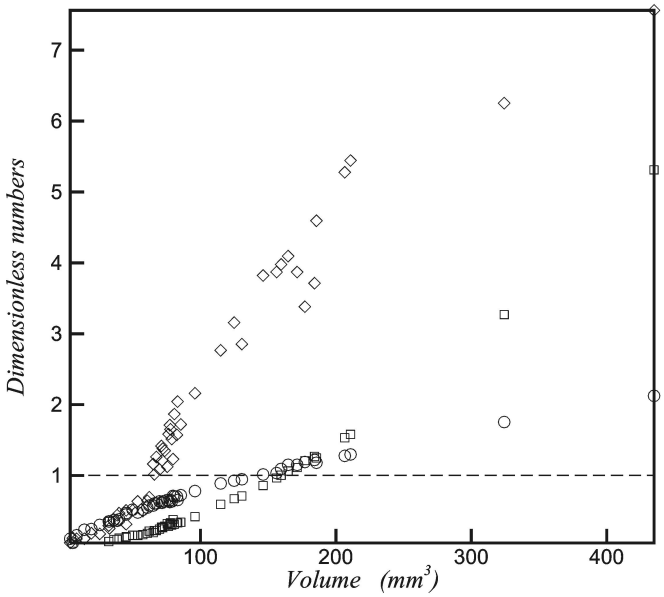

Figure 4.1: Dimensionless numbers: $\diamond$ Π number, $\square$ Capillary number (Ca) and $\circ$ Weber number (We) (HASE fluid $1.2wt.\%$). $V_c \simeq 65mm^3$

4.1 HASE fluids

The Figures 4.1,4.2 and 4.3 show the values of the dimensionless numbers: Ca, We and Π, as a function of the bubble volumen. As the volumen increases the dimensionless numbers increases too. So, the surface tension is overcome and the bubbles can be deformed from the spherical shape.

For the HASE fluids 1.2%, 1.5% and 1.7% the Π number increases faster than Ca and We. For the three cases, the discontinuity appears when the Π number is larger than the unit, i.e., the elastic forces are larger than the surface tension forces. Moreover, for volumes larger than the critical one, the Π number is larger than the others numbers (We and Ca). Obviously elastic effects are dominant. The volume at which they become important corresponds exactly to the volume for which the velocity discontinuity occurs. For the other liquids in this class, the same conclusion applies. The magnitude of the discontinuity is small for this liquids, due to there is not shear thinning. Then, the drag is not decreased by the viscosity reduction.

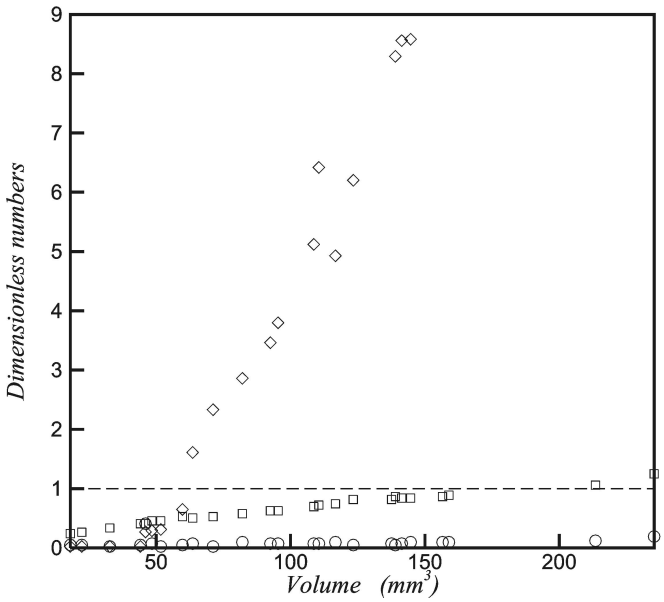

Figure 4.2: Dimensionless numbers: $\diamond$ Π number, $\square$ Capillary number (Ca) and $\circ$ Weber number (We) (HASE fluid 1.5$wt.\%$). $V_c \simeq 60mm^3$

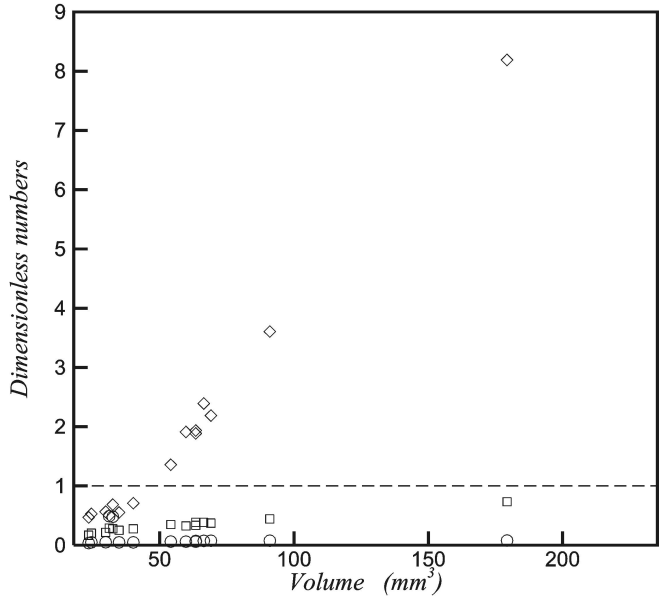

Figure 4.3: Dimensionless numbers: $\diamond$ Π number, $\square$ Capillary number (Ca) and $\circ$ Weber number (We) (HASE fluid 1.7$wt.\%$). $V_c \simeq 50mm^3$

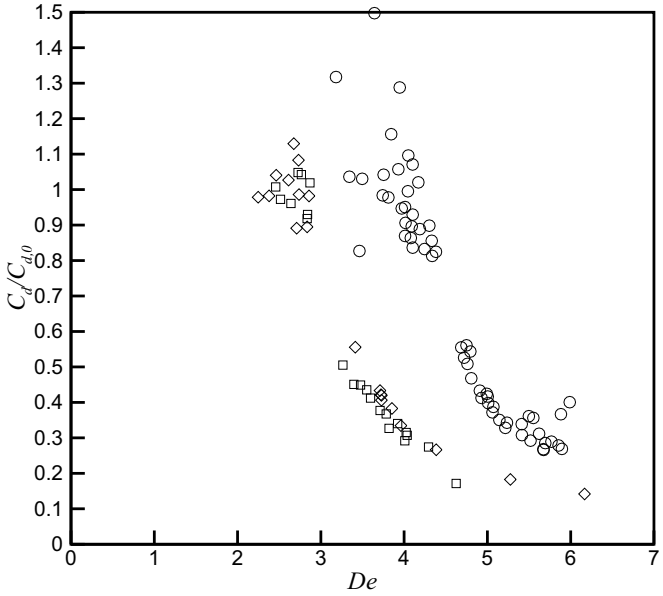

Figure 4.4: Dimensionless drag as a function of Deborah number for HASE Fluids: (∘) 1.2% HASE; (□) 1.5% HASE; (⋄) 1.7% HASE.

We can define a normalized drag coefficient, which is equal to $C_d/C_{d,0}$, where $C_{d,0}$ is the Stokes drag coefficient ($C_{d,0} = 24/Re$). For small bubbles (with a volume smaller than the critical one), the normalized drag coefficient will be close to 1. For large bubbles, there is an increase of the velocity. And so, for a decrease of the drag coefficient, the normalized drag coefficient will be smaller than 1.

The normalized drag coefficient is shown in Figures 4.4 and 4.5 as a function of the two dimensionless numbers previously defined. Clearly, for small De, the bubbles are spherical and $C_d/C_{d,0}$ is around 1. After a certain critical De, the normalized drag coefficient decays abruptly, corresponding to the point for which the discontinuity occurs. This behavior can be observed in the three solutions. However, the value of the critical De for which the discontinuity occurs is not unique, as it depends on the percentage of HASE. A similar trend can be observed for the capillary number: at a critical value of Ca, the normalized drag drops abruptly, but this critical value is different for each liquid. Hence, neither De nor Ca can be used to capture a generally valid condition for the jump to occur. There are two main conclusions from

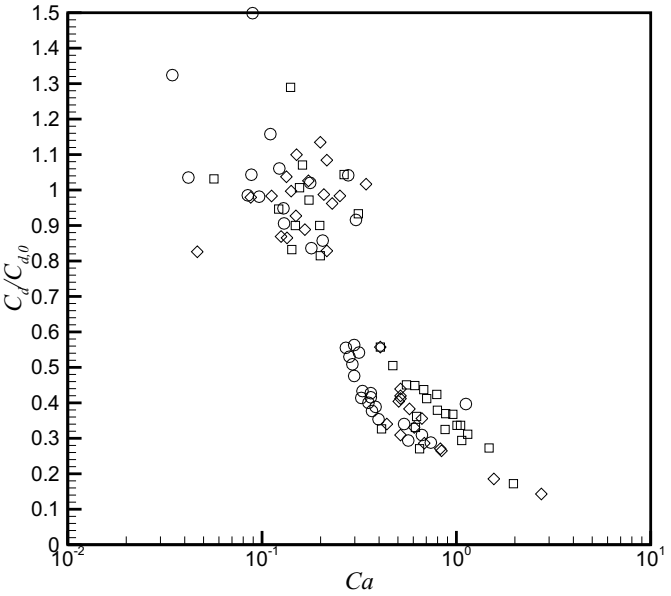

Figure 4.5: Dimensionless drag as a function of Capillary number for HASE Fluids: (∘) 1.2% HASE; (□) 1.5% HASE; (⋄) 1.7% HASE.

the results of this analysis: (1) the discontinuity appears when the elastic properties manifest themselves and (2) there is a significant change in the shape associated with the bubble velocity increase.

It is then appropriate to use the proposal dimensionless group Pi. This number would be large if elastic effects dominate over surface tension effects and vice versa. Figure 4.6 shows the normalized drag coefficient as a function of the dimensionless group Π. For this case, the transition from high to low drag appears to be the same for all the liquids: there is a critical value of $\Pi \sim 1$ that determines the conditions for the bubble velocity discontinuity to appear for all the HASE fluids. The tail at the rear part of the bubble leads to a decrease of the drag coefficient and consequently to a rapid increase of the velocity. Since the tail shape can also influence the flow behavior of the bubble, the tail shape can be related to the bubble velocity. A similar analysis is performed for the others liquids tested in the next sections.

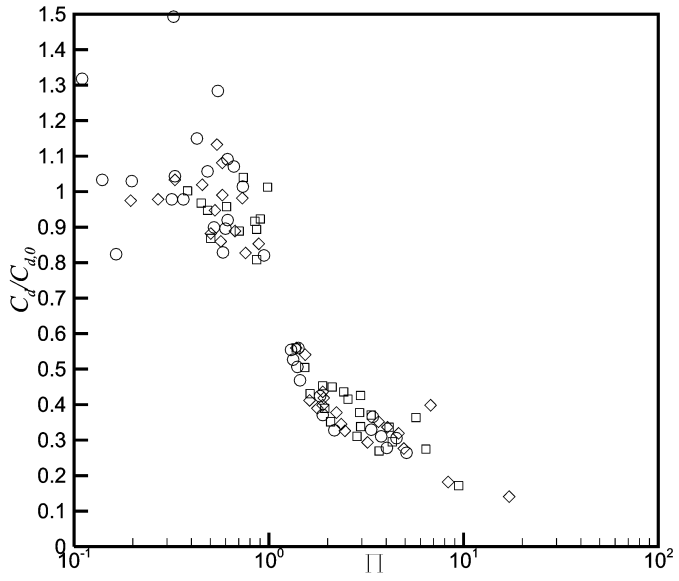

Figure 4.6: Dimensionless drag as a function of $\Pi = Ca \times De$ for HASE Fluids: ($\circ$) 1.2% HASE; ($\square$) 1.5% HASE; ($\diamond$) 1.7% HASE.

4.2 Others fluids

4.2.1 Aqueous viscoelastic fluids

For this case, we have shown the existence of a critical volume for which a velocity discontinuity occurs. Figure 4.7 shows the values of the three characteristic dimensionless numbers as a function of bubble volume for a fluid with $0.15wt.\%$ of PAA. The different dimensionless numbers increase with the bubble volume. At the critical value of the volume, the Π number becomes larger than 1. Moreover, for volumes larger than the critical one, the Π number is larger than the others numbers (We and Ca). Obviously elastic effects are dominant. The volume at which they become important corresponds exactly to the volume for which the velocity discontinuity occurs. For the other liquids in this class, the same conclusion applies. In the above case, the velocity discontinuity occurs when the Π number is larger than 1. It is also important to note that the Π number is also larger than the other dimensionless numbers ($\Pi > We, \Pi > Ca$) for the whole range of volumes studied.

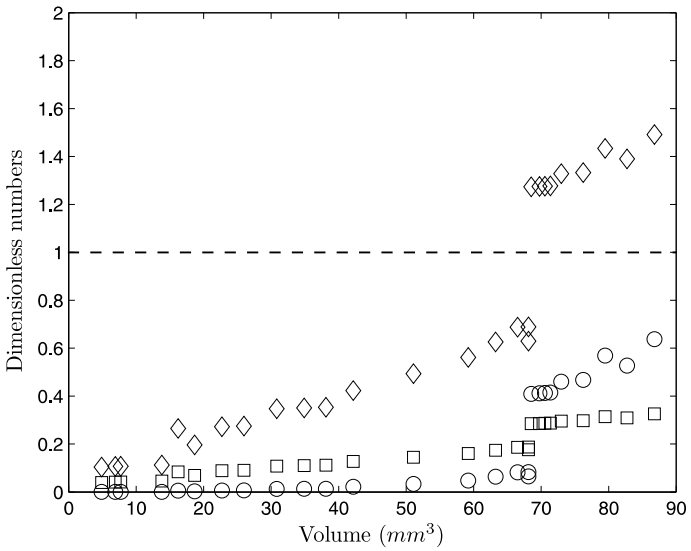

Figure 4.7: Dimensionless numbers: $\diamond$ Π number, $\square$ Capillary number (Ca) and $\circ$ Weber number (We) ($50wt.\%$ water, $50wt.\%$ glycerin and $0.15wt.\%$ PAA).

4.2.2 Non-aqueous viscoelastic fluids

For these experiments, we have shown that no velocity discontinuity occurs; however, we found that for a certain value of the volume there is a reduction of the slope of the velocity-volume relation. Figure 4.8 shows the values of the three characteristic dimensionless numbers as a function of the bubble volume for a fluid with $0.1wt.\%$ of PAA. For small bubble volume, all the dimensionless numbers are smaller than 1. At a certain value of the volume ($V = 100mm^3$), both Π and We become larger than 1. For larger volumes, the inertia forces are larger than the normal forces ($We > \Pi$). In this range of volumes, the bubbles are oblate and the reduction of the slope in the velocity-volume relation is observed. In this case, since inertial effects are dominant, no jump discontinuity appears. For polymer concentrations less than or equal to $0.1wt.\%$, the same conclusions are valid: the reduction of the slope of the velocity-volume relation is observed when the inertia forces are dominating.

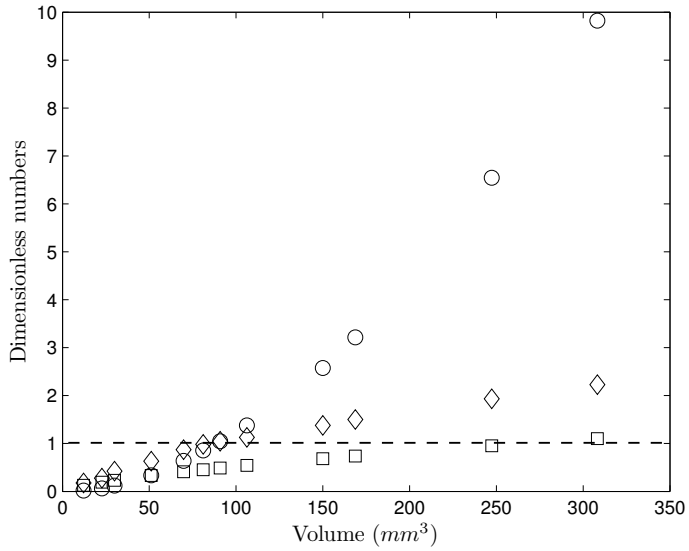

Figure 4.8: Dimensionless numbers: $\diamond$ Π number, $\square$ Capillary number (Ca) and $\circ$ Weber number (We) (Ethylen-glycol and $0.1wt.\%$ PAA).

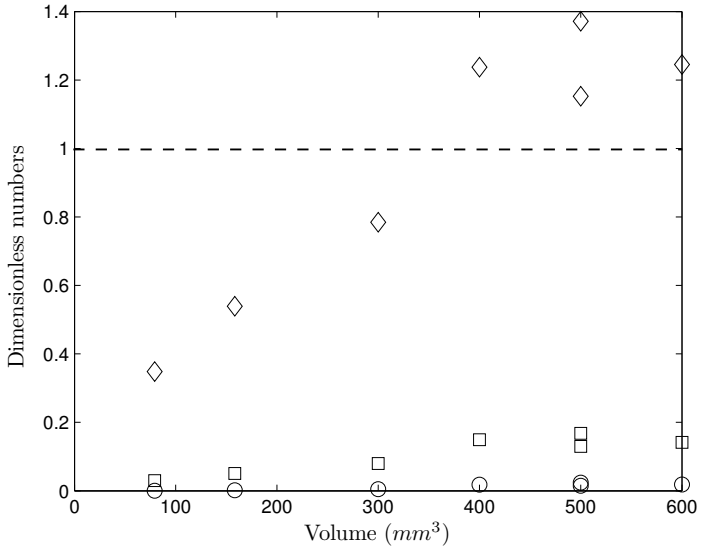

Figure 4.9: Dimensionless numbers: $\diamond$ Π number, $\square$ Capillary number (Ca) and $\circ$ Weber number (We) (glycerol and $0.2wt.\%$ PAA).

4.2.3 Constant viscosity elastic fluids

For this type of fluids, in low concentrations of PAA, no discontinuity and no change of the slope of the velocity-volume relation was observed. However, at large PAA concentrations, a sudden increase of velocity, indicative of a discontinuity, is observed. For this particular experiment it is not possible to determine clearly whether or not a jump in velocity was present. If we examine the experimental data in dimensionless terms, the results become clear. Figure 4.9 shows the dimensionless numbers We, Ca and Π as a function of the bubble volume for a concentration of PAA equal to $0.2wt.\%$. For small bubble volumes, all the dimensionless numbers are smaller than 1. At the critical value of the volume of approximately $V = 350mm^3$, the Π number becomes greater than 1 and larger than the other dimensionless numbers. This implies that the shape of the bubbles is determined mainly by elastic forces. The velocity increase occurs precisely when the elastic forces are larger than the other forces. This is in agreement with the results obtained in the case of aqueous viscoelastic fluids (section 4.2.1). However, in this case, the discontinuity is not as large as in the previous case. In the next chapter a discussion on the nature of the magnitude of the discontinuity is held. In addition to the change of shape that leads to a drag reduction, the shear thinning property of the fluid also plays an important role. Hence, for this liquid of near constant viscosity, the velocity discontinuity is not as large as in the other cases.

For smaller percentages of PAA ($0.1wt.\%$ of PAA), for all volumes tested, the Π number is always larger than 1, and larger than the other dimensionless numbers, which are smaller than 1, as shown in Figure 4.10. Again, the elastic forces dominate the flow, but no discontinuity of the velocity was found. For this particular case, the discontinuity of the velocity must have occurred at bubble volumes smaller than those tested here.

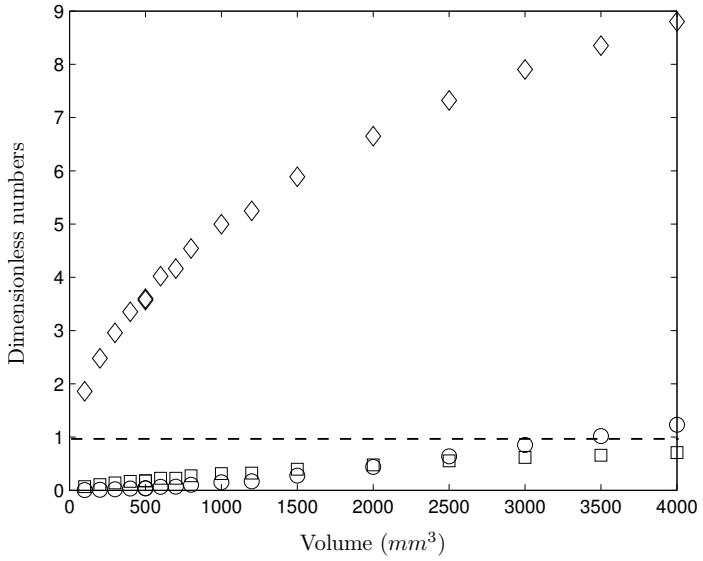

Figure 4.10: Dimensionless numbers: $\diamond$ Π number, $\square$ Capillary number (Ca) and $\circ$ Weber number (We) (glycerol and $0.1wt.\%$ PAA).

4.2.4 Shear thinning inelastic fluids

For these experiments, we have shown that no discontinuity of the velocity occurs. However, for large volumes, a reduction of the slope of the velocity-volume relation is observed. The analysis of the dimensionless parameters for a concentration of $0.1wt.\%$ of Carbopol and with $0.08wt.\%$ of triethylamine is presented in Figure 4.11. For small bubble volumes, both We and Ca are smaller than 1. The Π number is of course zero for this fluids. Above a certain volume, the Weber number becomes larger than 1 whilst the Capillary number remains less than unity. The decrease of the slope of the velocity-volume relation occurs for the bubble volume for which inertia forces are dominant, that is for $We > 1$, $We > Ca$ and $We > \Pi$. In fact, inertial effects cause the bubble to become oblate, leading to an increase in the form drag. The conclusions are the same for all experiments involving inelastic fluids.

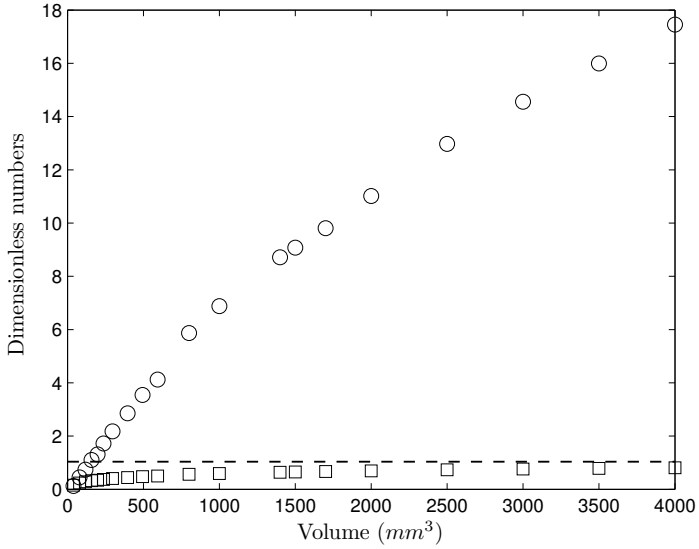

Figure 4.11: Dimensionless numbers: $\diamond$ Π number, $\square$ Capillary number (Ca) and $\circ$ Weber number (We) (ethylene-glycol, $0.1wt.\%$ Carbopol and $0.08wt.\%$ triethylenamine).

4.3 Dimensionless summarize

We may summarize the above results as follows: the velocity discontinuity appears only when the elastic forces are able to deform the bubble in a significant manner. Once the elastic forces have overcome the surface tension forces, the shape of the bubble changes from a spheroidal-convex to a concave shape with a tail appearing in the downstream section of the bubble. The change of the slope for the velocity-volume relation is due to inertia effects which are now dominant. This change is also linked to the change in shape of the bubble from a spheroidal-convex to an oblate shape. In some cases, the inertial and elastic effects may be important, that is when $\Pi > 1$ and $We > 1$. When $We > \Pi > 1$, the shape of the bubbles is oblate but shows a concave shape and a cusped tail in the downstream region. The velocity discontinuity does not occur under these conditions.

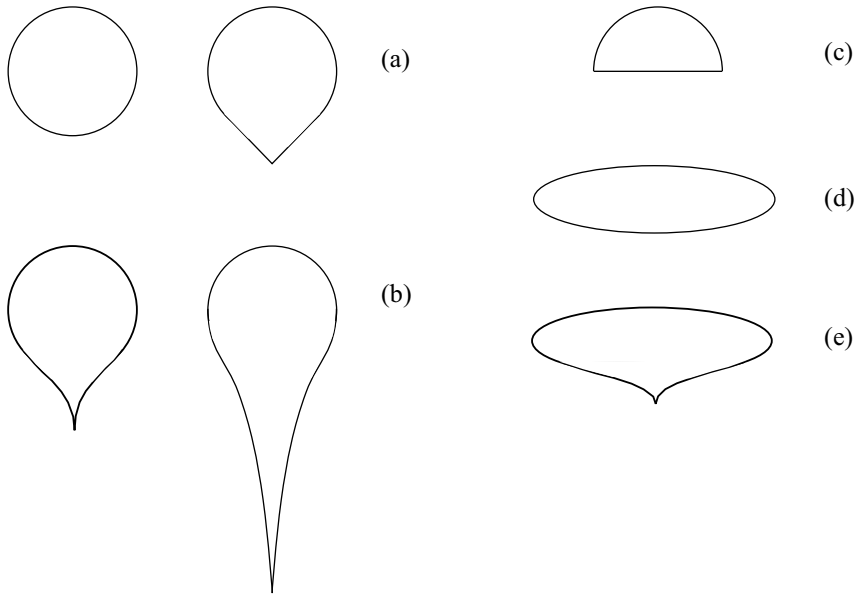

Figure 4.12: Shapes of the bubbles for different configurations (a) the bubble is spherical or spheroidal-convex, (b) the bubble presents a tail at the rear part and an inflection point, the bubble is concave, (c) the bubble is a spherical cap, (d) the bubble is oblate, (e) the bubble is oblate, but with a very small tail, or inflexion point at the rear part of the bubble.

4.4 Drag Coefficient

In order to quantify the changes in velocity of the bubbles, the drag coefficient may be examined. In particular, a normalized drag coefficient will be considered, an follows:

$$C_d^* = \frac{C_d}{C_{d,0}} \tag{4.4}$$

where C_d is the drag coefficient corresponding to the experimental measurements and $C_{d,0}$ is the Stokes drag coefficient for a spherical particle with the same diameter. An increase of the normalized drag coefficient indicates a reduction of the velocity.

From experimental observations, the bubble shapes may be grouped in four types:

- spherical bubbles or spheroidal-convex bubbles (fig. 4.12 a)
- concave spherical bubbles with a tail (fig. 4.12 b)

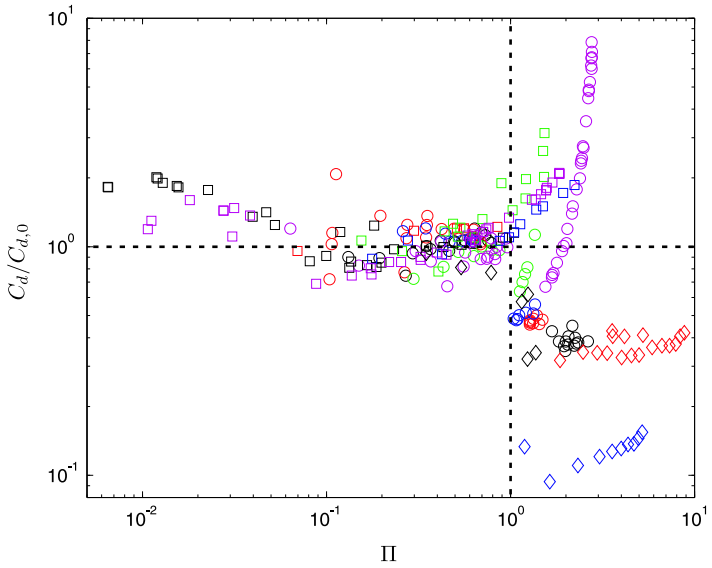

Figure 4.13: Normalized drag coefficient as a function of the Π number for different bubble shapes (○): fluid 1 (50$wt.$% of water, 50$wt.$% of glycerol and PAA), (□): fluid 2 (ethylene-glycol and PAA) ,(◇): fluid 3, Boger fluid (glycerol and PAA).

- oblate bubbles and spherical cap (fig. 4.12 c, d)
- oblate bubbles with a tail (fig. 4.12 e)

Figure 4.13 shows the normalized drag as a function of the dimensionless parameter Π for all the experimental results in this investigation, whit the exception of HASE fluids. The data are classified for the four types of fluids used in the experiments. It can be observed that when $\Pi < 1$, the normalized coefficient is approximately unity for all cases. It is important to note that all bubbles in this regime have spheroidal-convex shapes (Fig. 4.12 a). When the Π number becomes greater than 1, two distinct behaviors may be identified. For some cases, the normalized drag is smaller than 1, that is, a drag reduction is observed. The shape of the bubbles that experience a drag reduction is always concave with a tail (Fig. 4.12 b). On the other hand, when the normalized drag increases, when $\Pi > 1$, the shape of the bubbles is oblate (Fig. 4.12 e). Note that in this case, the data from the inelastic liquids is not shown ($\Pi = 0$). In order to determine what causes drag reduction or enhancement,

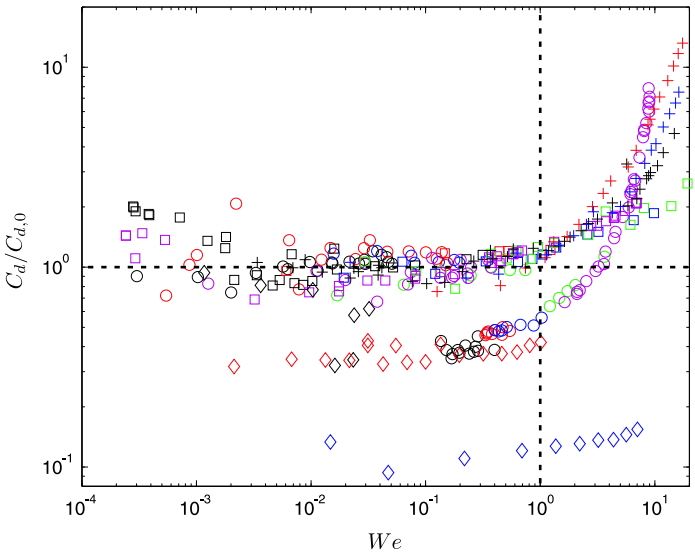

Figure 4.14: Normalized drag coefficient as a function of the Weber number for different experiments (○): fluid 1 (50$wt.\%$ of water, 50$wt.\%$ of glycerol and PAA), (□): fluid 2 (ethylene-glycol and PAA) ,(◇): fluid 3, Boger fluid (glycerin and PAA) , (+): fluid 4 (ethylene-glycol, carbopol and triethylamine).

the normalized drag coefficient is shown as a function of the Weber number in Figure 4.14.

When $We < 1$, the data are separated into two groups: experiments for which the drag is close to that calculated from Stokes-Hadamard law and experiments in which drag reduction is observed. If the data from figures 4.13 and 4.14 are replotted, classifying the experimental results according to the shape of the bubbles (fig. 4.15), it can be clearly observed that when the normalized drag is approximately 1 and $We < 1$, the shape of the bubbles is spherical or spheroidal-convex. When the normalized drag is less than unity and $We < 1$, the bubbles are concave with a tail. For bubbles, in which $We > 1$, generally a drag enhancement is observed. These bubbles are oblate (fig. 4.12 c, d and e). In a few cases, a modest drag reduction is observed. Bubbles in this regime are oblate but show the formation of a concave end as well as showing a tail. Finally, it is possible to plot the results as a diagram showing the Π number as a function of the Weber number (We) for all the experiments. This can be seen in Figure

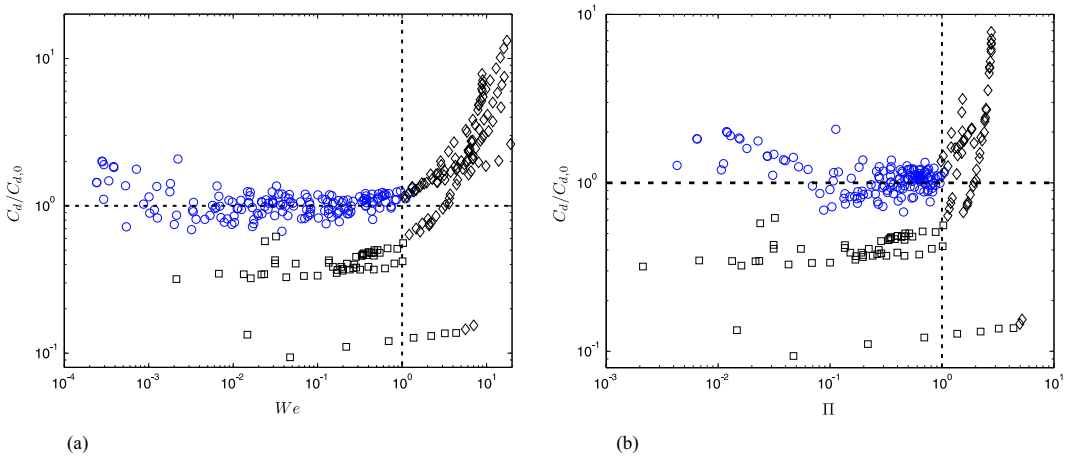

Figure 4.15: Normalized drag coefficient as a function of the Weber number for various shapes (○): spherical or spheroidal convex bubbles (fig. 4.12 a) (□): concave bubbles (fig. 4.12 b) ,(◇): oblate bubbles (fig. 4.12 c, d, e).

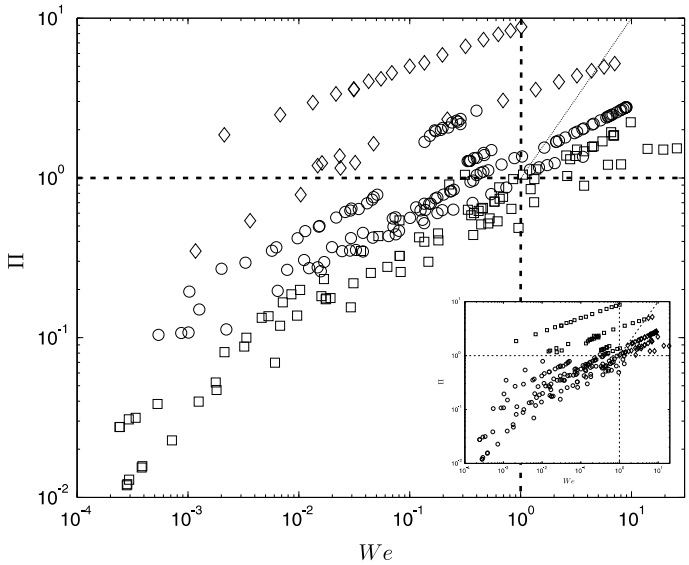

Figure 4.16: Map of Π number as a function of the Weber number for the different experiments: (○): fluid 1 (50$wt.$% of water, 50$wt.$% of glycerin and PAA), (□): fluid 2 (ethylene-glycol and PAA), (◇): fluid 3, Boger fluid (glycerin and PAA). Inset, same results by differentiating the shapes of the bubbles: (○): spherical or spheroidal convex bubbles (fig. 4.12 a) (□): concave bubbles with a tail (fig. 4.12 b), (◇): oblate bubbles (fig. 4.12 c, d, e).

4.16. Spherical bubbles are observed when both Π and Weber numbers are smaller than 1: the surface tension effects dominate. Oblate bubbles and spherical caps are observed for Weber numbers larger than 1, and Π number small or equal to 0 (the experimental results for inelastic fluids have been omitted in Figure 4.16). Bubbles with a tail appear for Π number larger than 1. Also, if $\Pi > We$, the bubbles are spheroidal-concave with a thin and long tail; for $We > \Pi$, the bubbles are oblate-concave with a small tail. The drag reduction is observed for the region that satisfies $\Pi > 1$ and $\Pi > We$.

Summarizing, the velocity discontinuity occurs when the elastic effects dominate. In this case, the shapes of the bubbles change from spherical to concave with a thin and long tail. The decrease of the slope of the velocity-volume relation occurs if the inertia effects dominate the flow. The shape of the bubble changes from spherical to oblate or to a spherical cap. In the case, when both inertia and elastic effects are predominant, the jump discontinuity only occurs when the elastic effects are larger than inertia and surface tension. If inertia effects are larger than the other two, a decrease of the slope of the velocity-volume relation appears.

4.5 Comparison with experimental results of other authors

To corroborate the fact that the velocity discontinuity appears when elastic normal forces are larger than the other forces, that is for $\Pi > 1$, we now analyze the experiments of other author for which the velocity discontinuity is observed. The data available for comparison and analysis is limited. Only in few cases, the authors report all physical properties. We have considered the experimental results of Rodrigue, De Kee and Chan Man Fong (1996),

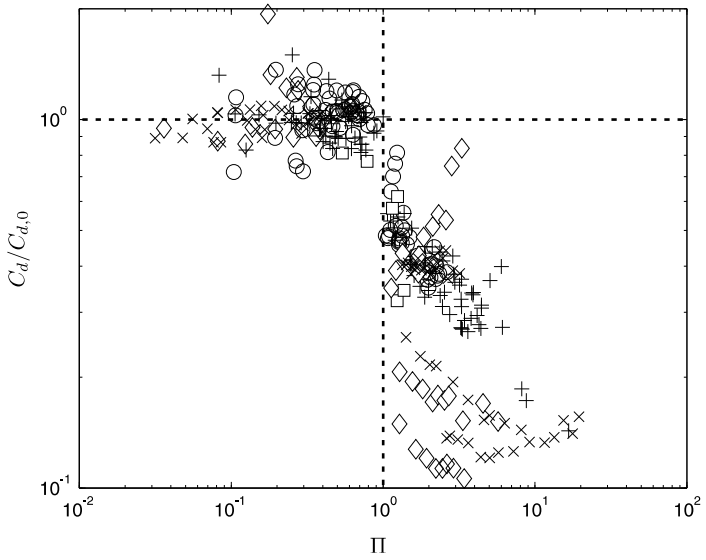

Figure 4.17: Map of Π number as a function of the Weber number (We) for different fluids: (∘) fluid 1, (□) Boger fluid, (+) HASE fluid Soto et al. (2006), (⋄) water and glycerin PAA and SDS, Rodrigue, De Kee & Chan Man Fong (1996); Rodrigue, De Kee and Chan Man Fong (1998); Rodrigue and De Kee, (1999), (×) 80$wt.\%$ of water, 20$wt.\%$ of glycerol and 0.5$wt.\%$ of PAA and SDS, Rodrigue and Blanchet (2002).

Rodrigue, De Kee and Chan Man Fong (1998) and Rodrigue and De Kee, 1999, who used $50-50wt.\%$ water-glycerol mixtures and PAA and a range of small amounts of sodium dodecyl sulfate (SDS) to adjust the surface tension. We have also included the data of Rodrigue and Blanchet (2002) who used $80-20wt.\%$ water-glycerol mixtures and PAA and SDS. The results from Soto et al. (2006) for the case of HASE-type liquids are also included. Figure 4.17 shows the dimensionless drag as a function of Π number for all the experimental data mentioned above, along with our measurements for the case of the fluid 1 and fluid 3. It may be seen that in the region where Π is less than one, the normalized drag coefficient is approximately 1 and therefore no drag reduction nor a jump discontinuity appears. If, however, Π is greater than one, drag reduction is evident and the jump discontinuity occurs.

Chapter 5

Velocity Discontinuity Magnitude

In this chapter, a discussion about the magnitude of the discontinuity is presented. The main idea is to consider the effect of the different parameters involved in the problem. A commercial finite element software (FEMLAB) was used to evaluate the drag on the bubble surface.

5.1 The magnitude of the discontinuity

Form the vast experimental evidence presented here, it can be concluded that the physical process which determines the appearance of the jump discontinuity in velocity is the following: as the bubble volume increases, the resulting mean shear rate on the surface also increases. As a result, the elastic forces on the surface of the bubble become large. The shape of the bubble slowly changes from spherical to teardrop shape. At a given shear rate, and its corresponding bubble volume, elastic forces overcome the surface tension forces that tend to maintain the spherical form of the surface. At this point the dimensionless number Π becomes greater than one; the shape changes drastically from convex to concave with the formation of a sharp

Table 5.1: Magnitude of the velocity discontinuity. The velocities ratio for two bubbles, one just below and other just above the critical volume ($\frac{V_a}{V_b}$).

Author	$\frac{V_a}{V_b}$
Astarita and Apuzzo (1965)	2.22-5.86
Zana and Leal (1978)	4-5
Rodrigue (1998)	1.65-5
Herrera et al (2003)	1.8-2.4
HASE Fluids	1.63-2.45

cusp. This new shape has a more hydrodynamic form and the corresponding drag coefficient becomes much smaller with the corresponding increase in bubble velocity. This in turn, gives rise to an increase in the mean shear rate at the surface which causes the viscosity of the fluid to drop further if the fluid is shear thinning. The reduction of viscosity causes an additional reduction of the drag, leading to a significant increase of velocity. Moreover, it has been shown that elastic effects are also drag-reducing (Leal, Skoog & Acrivos, 1971).

Therefore, a further reduction of the drag on the bubble can be expected in this case. Furthermore, it is also possible that the increase in velocity may cause a change of the boundary condition on the bubble (Blanco & Magnaudet, 1995) since the surface is in most cases dirty for small slow bubbles; hence, if the bubble moves faster, the surface may become cleaner and mobile, which would also result in an additional reduction of the drag. All these effects are the contributions that lead to the phenomena of the jump discontinuity. The magnitude of the velocity discontinuity for selected fluids is presented in the Table 5.1 from several authors. In all cases the velocities ratio is larger than 1.5, the maximum possible value for a complete change in boundary condition, from non-slip to slip. Through computer simulations it is possible to isolate the contributions involved in the magnitude of the discontinuity.

Table 5.2: Velocity discontinuity principal contributions. A comparison between the experimental conditions and the parameters used in simulations.

Experimental	Simulation
Viscosity	Viscosity
Bubble velocity	Bubble velocity
Bubble shape	Bubble shape
Boundary condition	Boundary condition (slip or non-slip)
Elasticity	

In the Table 5.2 the experimental variables and those considered in the simulation are shown. All conditions can be included in the simulation, except the elasticity.From experimental parameters es possible to obtain the ratio of drag coefficients for a bubble with volumen just below the critical and a bubble with volumen just above the critical. This is calculated by the equation:

$$\frac{Cd_{,2}}{Cd_{,1}} = \frac{d_{,2}}{d,1}(\frac{V_{,1}}{V_{,2}})^2 \tag{5.1}$$

where C_d is the drag coefficient, V the terminal velocity of the bubble, d the bubble equivalent diameter and the subindexes, 2 and 1, refer to the bubble just above the critical volume and to the bubble just below the critical volume, respectively. For the simulations, the drag coefficient is determined with the equation:

$$C_d = \frac{2F_d}{\pi\rho(V)^2(\frac{d}{2})^2} \tag{5.2}$$

where ρ is the fluid density, V is the bubble velocity and F_d is the total force at the bubble surface in the motion direction. Note that in all these simulations the bubble shape is assumed to remain fixed.

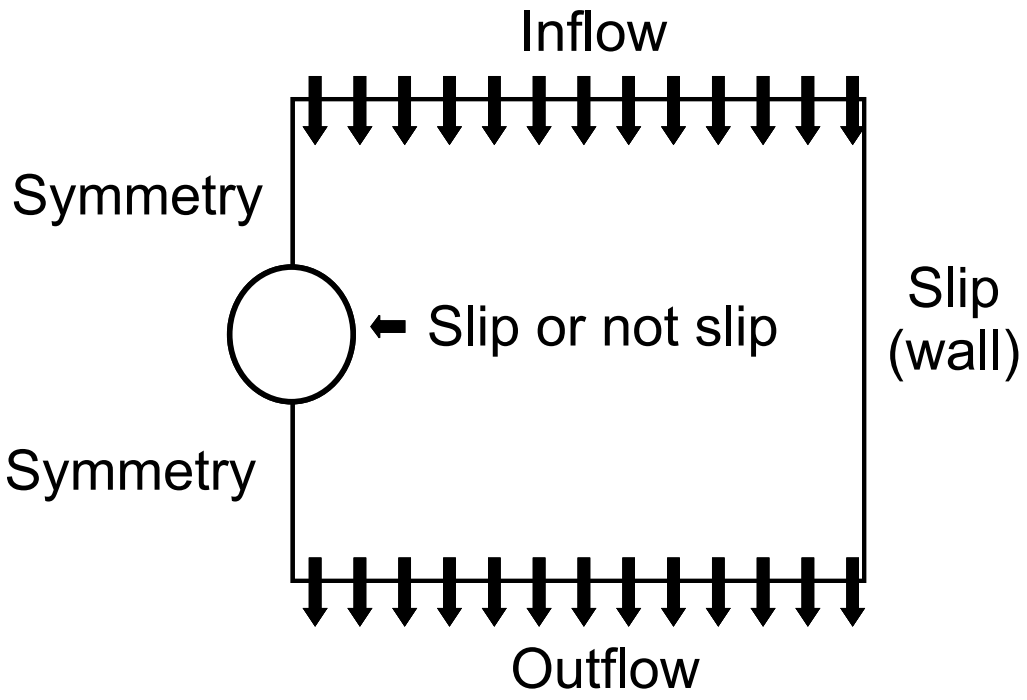

Figure 5.1: Idealization of the problem in a two dimension sketch and boundary conditions.

5.2 Computational Space

The computer simulations were performed considering a Newtonian fluid and a 2D axi-symmetric flow. Figure 5.1 shows the boundary conditions imposed on the simulations. The shape of bubbles were obtained by a digital image processing (describe in a previous chapter), from photographs of real bubbles. Typical bubble shapes with their correspondent mesh are shown in Figure 5.2.

In order to evaluate the relative importance of the relevant effects, we performed simulations to determine the drag coefficient for bubbles just after and just before the discontinuity. These simulations were done for liquids 1-2 and 1-4 ($50wt.\%$ of water, $50wt.\%$ of glycerol, and $0.15wt.\%$ PAA or $0.05wt.\%$ PAA) and for two HASE fluids (properties shown in Table 5.3).

With these simulations, we aim to evaluate the effects of the change of shape, reduction of viscosity and change in boundary conditions by considering shape fixed bubbles. The terminal velocity and shape are taken from the experiments. The drag force is determined for the flow around bubble with a

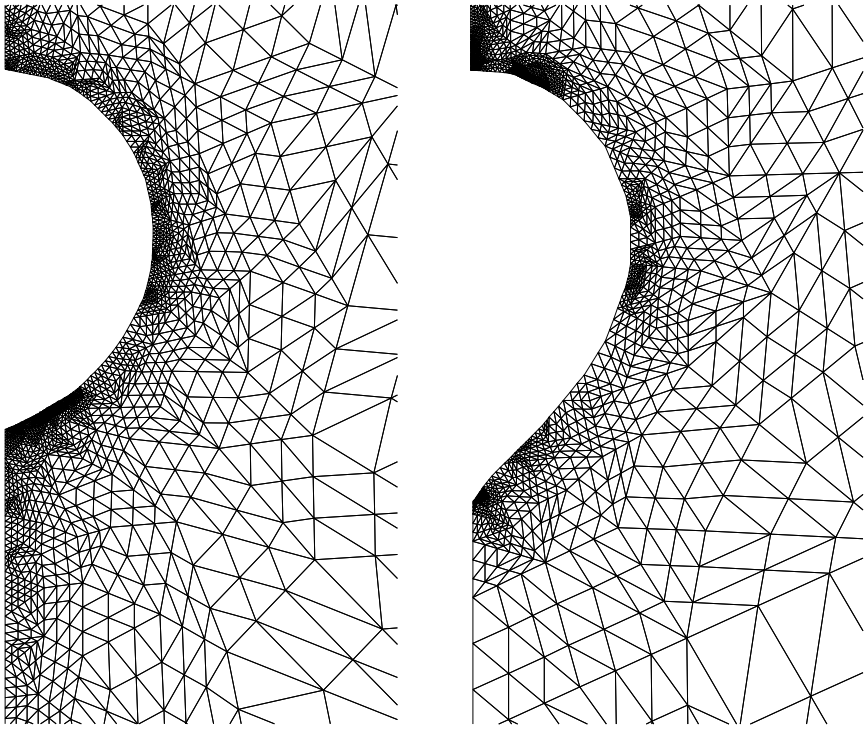

Figure 5.2: Shape of the bubble and mesh used for the simulation (a) bubble just before the discontinuity, (b) bubble just past the discontinuity.

fixed shape. The shape is that obtained from the experiment for cases either before or after the velocity discontinuity. For each case, we consider the value of the viscosity to be the one corresponding to each experimental condition using the mean shear rate as defined previously (see Table **??**). It is important to remark that our calculation scheme does not include the effect of the elasticity of the fluid.

Table 5.3: Experimental properties of the selected bubbles to performed numerical simulations, for bubbles formed just before and after the critical volume.

Bubble	$d_{eq}(mm)$	$Vol(mm^3)$	Vel (mm/s)	$\mu(Pas)$	$\overline{\dot{\gamma}}$	Re
1-2 (before)	3.28	18.6	77.5	0.128	11.8	2.23
1-2 (after)	4.06	35.1	165.1	0.108	20.32	7.03
1-4 (before)	4.94	63.2	33.2	0.702	3.36	0.264
1-4 (after)	5.12	69.7	81.28	0.462	7.96	1.01
HASE (1.2%) (before)	4.55	49.33	29.8	0.22	3.21	0.606
HASE (1.2%) (after)	5.05	67.6	50.5	0.22	4.99	1.61
HASE (1.5%) (before)	4.54	49.2	9.02	1.14	0.992	0.036
HASE (1.5%) (after)	4.88	61.2	14.7	1.14	1.51	0.063

For this study cases two boundary conditions are considered. For bubbles before the velocity discontinuity, the condition at the interface is taken to be non-slip (rigid surface). Conversely, for bubbles moving after the discontinuity, a clean free slip condition at the surface is considered. With this set of conditions, we can evaluate whether or not the magnitude of the jump is only the result of the change of shape along with a change of surface boundary conditions. It must be emphasized that this drastic change of boundary conditions is most likely an extreme condition; in an experiment, the surface of the bubble is under ordinary laboratory conditions, neither clean nor fully contaminated.

Table 5.4: Calculated drag coefficients for two bubbles one before and another after the critical volume with slip or non-slip boundary condition. HASE at $1.5wt.\%$

	non-slip	slip
Bubble before	685.3	556.9
Bubble after	385.3	305.7

Table 5.5: Comparison of the effect of shape and boundary condition on the calculated drag coefficient. Bubbles just before and just after the discontinuity moving in HASE at $1.5wt.\%$

	non-slip	slip	
Bubble before	685.3	556.9	$\frac{Cd_{,1slip}}{Cd_{,1nonslip}} = 0.813$
Bubble after	385.3	305.7	$\frac{Cd_{,2slip}}{Cd_{,2nonslip}} = 0.794$
	$\frac{Cd_{,2nonslip}}{Cd_{,1nonslip}} = 0.547$	$\frac{Cd_{,2slip}}{Cd_{,1slip}} = 0.594$	$\frac{Cd_{,2slip}}{Cd_{,1nonslip}} = 0.446$

The drag coefficients obtained from simulations, for the HASE fluid at 1.5 %, are shown in Table 5.4. It is possible to compare the drag for the same shape, but with different boundary condition. The reduction in drag is evaluated with the drag coefficients ratio:

$$\frac{Cd_{,1slip}}{Cd_{,1nonslip}} = 0.813 \tag{5.3}$$

the subindex 1 refers to a bubble before the discontinuity and the subindex 2 refers to a bubble after the discontinuity. This value is higher than 0.66, the expected ratio for an sphere. Similary, for the bubble after the discontinuity the ratio is:

$$\frac{Cd_{,2slip}}{Cd_{,2nonslip}} = 0.794 \tag{5.4}$$

as in the previos case, the drag reduction is higher than 0.66, it implies that the contribution of the change in boundary condition for spheroidal bubbles is not as important as in the spherical case. The reduction in the drag due to the change in shape, without consider the change in boundary condition;

$$\frac{Cd_{,2nonslip}}{Cd_{,1nonslip}} = 0.547 \tag{5.5}$$

$$\frac{Cd_{,2slip}}{Cd_{,1slip}} = 0.594 \tag{5.6}$$

is smaller than 0.66. Then, the change in shape is the more important factor for the drag reduction. It is important to recall that the viscosity of the HASE

liquids remains nearly constant for mean shear rate near the jump. Finally, considering the ratio between the drag coefficients of a bubble right after the critical volume and a bubble right before the critical volume, the following:

$$\frac{Cd_{,2slip}}{Cd_{,1nonslip}} = 0.446 \tag{5.7}$$

From the experimental data is possible to determine de drag coefficient ratio for the same two bubbles near the discontinuity, one before and the other one after.

$$\frac{Cd_{,2}}{Cd_{,1}} = 0.412 \tag{5.8}$$

Experimentally, obviously all the contributions to the drag are included. This drag ratio is smaller than that obtained from the simulation. It means that the difference between the two measures represents all the effects not considered in the simulation. Hence, it could be concluded that the magnitude of the discontinuity is also strongly affected by the elasticity of the fluid.

Results from simulations, along with the experimental values are shown in Table 5.6. The drag coefficients just after the discontinuity, $Cd_{,2}$ and just before the discontinuity $Cd_{,1}$ allow to determine the magnitude of the discontinuity, i. e., the ratio of these drag coefficients. For all experiments, this ratio $Cd_{,2}/Cd_{,1}$ is smaller than 1. Moreover, the ratio obtained with the simulations is larger than that obtained in the experiments. This implies that the velocity discontinuity is larger in the experiments than that predicted by the simulations. Hence, the elastic effects must also be taken into account to appropriately evaluate the magnitude of the discontinuity. These results show that the amplitude of the discontinuity can not be fully determined with only a change of the boundary condition from non-slip to slip as proposed by Astarita & Apuzzo (1965), Barnett, Humphrey & Litt (1966), Calderbank, Johnson & Loudon (1970), Leal, Skoog & Acrivos (1971)).

Table 5.6: Drag coefficient ratio defined as the drag coefficient of the bubble just after the discontinuity (indexed 2) divided by the drag coefficient of the bubble just before the discontinuity (indexed 1). This ratio is determined with the experiments (indexed exp) and also with the simulations (indexed sim).

Fluid	$(\frac{C_{d,2}}{C_{d,1}})_{exp}$	$(\frac{C_{d,2}}{C_{d,1}})_{sim}$	$\frac{(\frac{C_{d,2}}{C_{d,1}})_{exp}}{(\frac{C_{d,2}}{C_{d,1}})_{sim}}$
1-2	0.273	0.307	1.127
1-4	0.173	0.218	1.2
HASE 1.2%	0.373	0.453	1.216
HASE 1.5%	0.403	0.446	1.106

Experiments on the sphere translation in constant viscosity elastic fluids (Boger fluids) have been reported by Chhabra, Uhller & Boger (1980) and Mena, Manero & Leal (1987). Chhabra, Uhller & Boger (1980) observed a decrease in the drag coefficient ratio $C_d/C_{dStokes}$ from one to approximatively 0.75, as the Weissenberg number (Wi, or Deborah number) increased from 0 to 1. For Weissenberg numbers larger than one, the drag ratio was found to be independent of the Weissenberg number. Chmielewski, Nichols & Jayaraman (1990) studied the influence of the elasticity on the drag coefficient for different types of Boger fluids. In the case of a non-aqueous Boger fluid, Stokes law was obeyed for Weissenberg numbers up to 0.3 and then increased with the Weissenberg number. In the case of an aqueous Boger fluid, Stokes law was obeyed up to Weissenberg numbers equal to 0.1, but then decreased with increasing Weissenberg number. These results are in qualitative agreement with those of Tirtaatmadja, Uhlherr & Sridhar (1990). For our experiments, the liquids in which the discontinuity is observed are aqueous viscoelastic solutions. In all cases, the Weissenberg number increases with the volume of the bubble, and is smaller than 1. Hence, from other results in the literature an elastic reduction of the drag can also be expected, and its magnitude is of the correct order.

Chapter 6

Nonaxisymmetric Cusps

Furthermore, a morphological description related to the formation of non-axisymmetric cusps at the rear of the bubble is presented.

Lastly, a photographic study of the peculiar shapes of the bubble tails that appear after the bubble velocity discontinuity is presented. Figure 6.1 shows the terminal velocity of bubbles as a function of volume. The symbols denote the different tail shapes observed experimentally. The 2D cusp does not have a preferential orientation. Hence, several experiments were performed to obtain a frontal views. Note that these experiments are performed in a cylindrical tank with control temperature (to avoid temperature gradients) and enough time was elapsed to avoid fluid memory effects.

Previously, it was observed that a long, thin axisymmetric tail appears on the rear part of bubbles immediately after the critical volume (this case is shown in Figure 6.2 *a*). The thickness of the tail can be of the order of a few microns, while its length amounts to a few centimeters. The tail eventually breaks into micron-sized bubbles. This behavior resembles the so-called tip-streaming phenomena, when daughter drops are ejected from a thin thread at the tip of a highly stretched drop. The tip-streaming behavior was first reported by Taylor (1964) and since then has been studied by many authors. To our knowledge, tip streaming has not been reported to date for the case

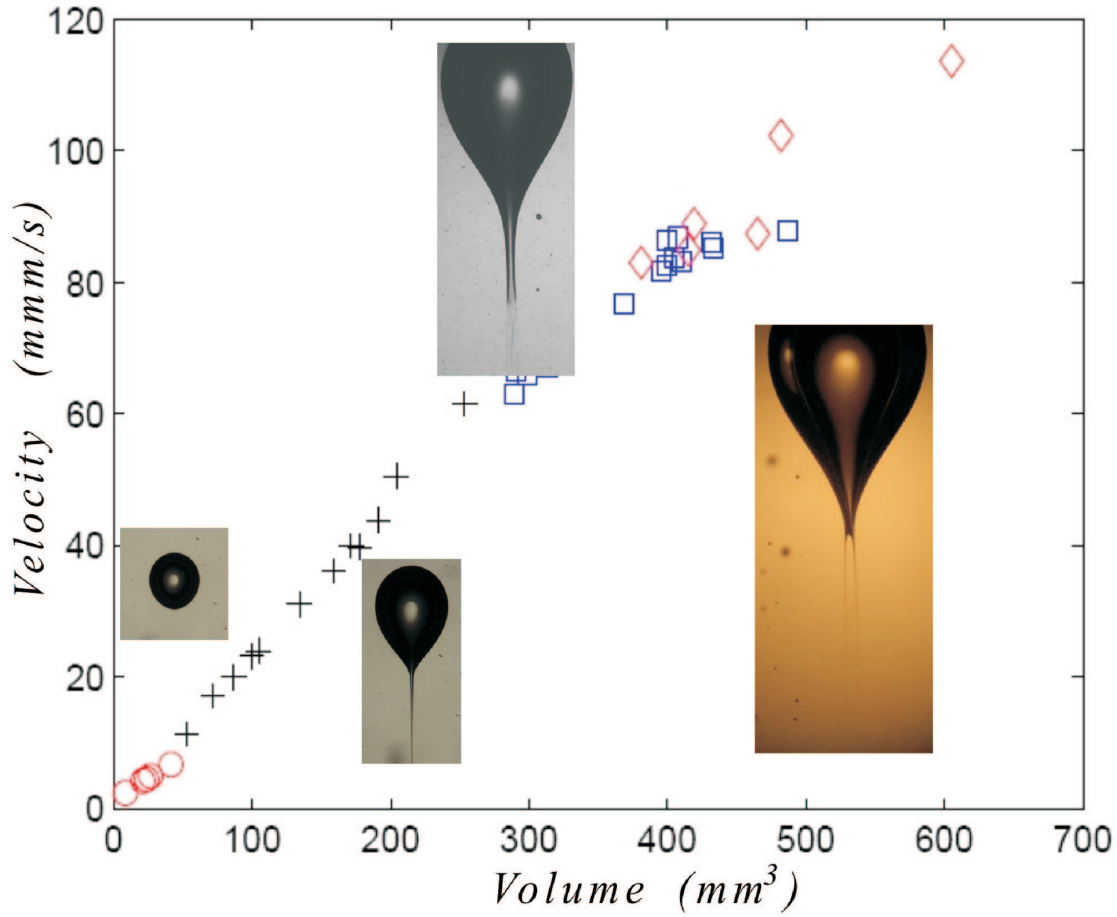

Figure 6.1: Velocity as a function of the bubble volume for 1.5% HASE. Different critical volumes for the different bubble shapes: (○) spheroidal bubbles; (+) axisymmetric tail (tip streaming); (□) 2D edged tail (fish-bone streaming); (◇) 2D edged tail (two-thread streaming).

of air bubbles moving in complex non-Newtonian liquids. For larger bubble sizes, the cusped tip transforms into a "blade-edge" tip (two–dimensional cusp, figure 6.2 *b* and c).

For volumes smaller than $280mm^3$ (corresponding to shear rates smaller than $15s^{-1}$), the tail is axisymmetric, very thin, and long. For larger volumes, a 2D cusp appears. For volumes between 280 and 350 mm^3 (corresponding to shear rates between 15 and 18 s^{-1}), only fish-bone streaming is observed. For volumes larger than 350 mm^3 (corresponding to shear rates larger than 18 s^{-1}) both two-thread and fish-bone formations can be observed. Although the influence of the type of 2D tail on the terminal velocity of the bubble (drag coefficient) is not significant, we observe that when the two types of edge-streaming appear, a larger scatter of data of bubble velocity is observed. The different shapes of tails reported in this section have never been observed for rising bubbles in either polymeric or worm-like micellar fluids. The 2D cusp does not have a preferential orientation. Note that these experiments are performed in a cylindrical tank with control temperature (to avoid temperature gradients) and enough time was elapsed to avoid fluid memory effects.

The 2D cusped end was observed from simultaneous tail images taken at perpendicular views. Several experiments are necessary to obtain images in which the edge of the tail is parallel to the photo plane (images shown in Figure 6.2 b and c). The appearance of such shapes has also been previously observed by Liu et al, 1995. Moreover, the streaming behavior can also be observed in 2D cusps; the so-called "edge streaming." We have observed that the 2D cusped tail can break into different manners for the same nominal experimental conditions. To further investigate the conditions for which the 2D cusps appear, additional series of experiments were performed for such

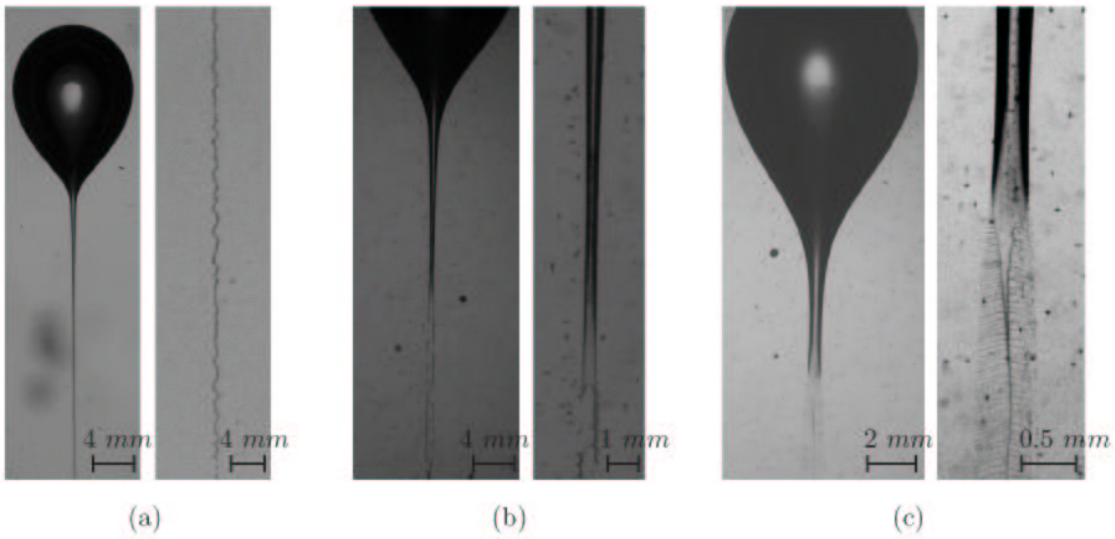

Figure 6.2: Various tail shapes for bubbles moving in a 1.5% HASE solution: (a) tip streaming: bubble with filament tail and zoom of the tail instability; (b) edge streaming: bubble with knife-edge tail and breakdown process of the tail edge; (c) edge streaming: bubble with knife-edge tail and breakdown process of the tail edge; the volume is larger than that shown in (b).

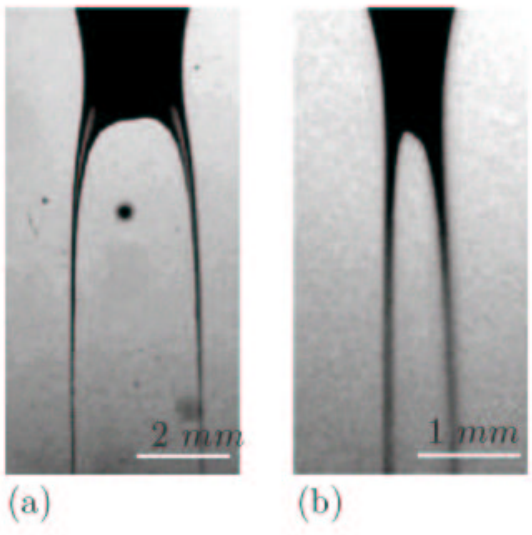

Figure 6.3: Two perpendicular views (a) and (b) of the tail; the tail breaks into two different threads ($V = 824mm^3$, 1.5% HASE).

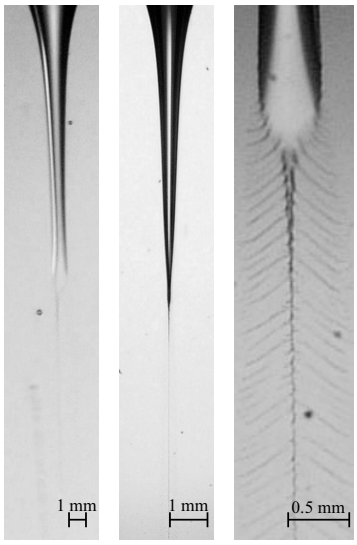

Figure 6.4: Two perpendicular views (a) and (b) of the tail. (c) The tail collapses into a single thread with perpendicular filaments that resemble a "fish backbone" ($V = 391mm^3, 1.5\%$ HASE)

large bubbles. The terminal velocities were measured for increasing bubble volumes, and the shape of the tails was also identified.

In some cases, the tail breaks into two different threads (Figures 6.2 and 6.3). The two threads extend for some distance, but eventually each one breaks into microbubbles. In other cases, the 2D tails collapse into a single thread with perpendicular filaments that resemble a "fish backbone" (Figures 6.2 and 6.4). All these fine threads eventually break into small bubbles. Edge streaming has not been previously reported for these fluids. Clearly, the viscoelastic nature of the HASE solutions is responsible for the formation of the cusped and edged tips at the back of the bubbles. However, the basic mechanism for the cusp-to-edge transition is not known. Tip streaming phenomenon is an indication that, near the cusp, high levels of fluid stretching are present. There is also a possibility that the surface active ingredients are being convected along the bubble surface, inducing surface tension gradients, hence, enhancing the tip streaming. The formation of these different shapes may be, in fact, a result

of the specific properties of the associative polymer fluid. Clearly, further experiments are needed to understand the formation process of a particular tail shape. With the present experimental setup, it is difficult to determine precisely the critical volume from which the tail changes from axisymmetric to two dimensional (either two threaded or fish backbone).

Chapter 7

Conclusions

We have shown that for bubbles rising in an associative polymer solution, as the bubble volume increases, a discontinuity of the velocity occurs. This discontinuity in the velocity is smaller than that observed for aqueous shearthinning viscoelastic liquids. A more distinctive feature for this case is that the slope of the relation velocity-volume increases significantly past the discontinuity. This particular behavior was studied for various HASE concentrations. It was possible to relate this discontinuity with the rheological properties of the fluid. In fact, the shear rates for which the discontinuity occurs correspond to those for which the normal stresses appear. It is important to note that the critical shear rates also correspond to the point at which the shear thickening appears in some solutions, which may contribute to reducing the strength of the velocity jump. The discontinuity can also be related to the bubble shape and to the flow around the bubble. For volumes smaller than the critical volume, the bubbles are spherical or spheroidal and the flow around the bubble is similar to that of a Newtonian liquid. For volumes larger than the critical one, the rear of the bubble is concave and presents a tail at their rear part. The flow around the bubble is more complex, and the presence of a negative wake can be observed.

This study provides a criterion for the determination of a critical volume at which the bubble velocity discontinuity occurs. Due to the importance of the elasticity and the surface tension, a dimensionless number defined as $\Pi = N_1 d/\sigma$ is proposed to determine the jump conditions. The discontinuity occurs for $\Pi_{crit} \approx 1$. For the case of small bubbles, we found good agreement between experiments and predictions for the velocities according Stokes-Hadamard laws. For small bubbles, the shear rate is small, and consequently, the liquid can be considered as Newtonian. The viscosity for this case had to be obtained with a falling-bead technique. In agreement with previous investigations, we found that the viscosity determined in this manner was larger than that obtained under simple-shear viscometric flow. From the present results, we have determined that the appearance of the discontinuity results from a balance between elastic and surface tension forces. Furthermore, such criterion was successfully tested for several classes of fluids (viscoelastic, shear thinning inelastic and constant viscosity elastic liquids), and a comparison with experimental results from literature was carried out.

We have shown with simulations that the magnitude of the discontinuity is caused by a combination of the change of shape, the reduction of the viscosity, the elastic effects and also, perhaps, the change of boundary conditions on the bubble surface. With simple Newtonian calculations, the simulation results could not predict the magnitude of the discontinuity as measured experimentally. Therefore, we conclude that elastic effects also provide an important contribution to the total magnitude of the drag reduction of viscoelastic fluids around moving bubbles. Finally, for large bubble volumes, a photographic study for the bubble shapes and the particularly the tail shapes was presented. Different kinds of tails can be observed. The influence of the extensional stresses at the rear of the bubbles, seems to be responsible of the formation of

a long and thin tail. As increasing the volume, the velocity increases and the tail breaks up. For larger volumes a formation of 2D tails was observed, and eventually such tails breakup in a multithread pattern. The basic mechanism of for the cusp-to-edge transition is not know. However, there is a possibility that the surface activity of the HASE fluids and their peculiar chemical structure are responsables of this behavior.

Bibliography

Arigo, M. T. and McKinley, G. H. "An experimental investigation of negative wakes behind spheres settling in a shear-thinning viscoelastic fluid", Rheol. Acta, **37**, 307-327 (1998).

Astarita, G. and Apuzzo,G. "Motion of gas bubbles in non-Newtonian liquids", A.I.Ch.E. J. **11**, 815-820 (1965).

Atkins, P. and Paula, J. "Physical chemistry", W. H. Freeman and Company, New York, Chap 3 and 28,(2002).

Aubry, N. and Singh, P. "Transient and steady state of a rising bubble in a viscoelastic fluid", Journal of Fluid Mechanics **589**, 215-252 (2007).

Barnett,S. M., Humphrey, A. E. and Litt, M. "Bubble motion and mass transfer in non-Newtonian fluid", A.I.Ch.E. J. **12**, 253-259 (1966).

Bautista, F., de Santos, J. M., Puig, J. E. and Manero, O. "Understanding thixotropic and antithixotropic behaviour of viscoelastic micellar solutions and liquid crystalline dispersions. I. The model", J. Non-Newtonian Fluid Mech. **80**, 93 (1999).

Belmonte, A. "Self oscillations of a cusped bubble rising through a micellar solution", Rheol. Acta **39**, 554-559 (2000).

Bird, R.B., Stewart, W.E. and Lightfoot, E.N. "Transport phenomena" , Wiley, New York, (2002).

Bird, R.B., Amstrong, R.C. and Hassager, O. "Dynamics of polymeric liquids", Jhon wiley & sons, New York, (1976).

Bisgaard, C. and Hassager, O. "An experimental investigation of velocity fields around spheres and bubbles moving in non-Newtonian liquids", Rheol Acta **21**, 537 (1982).

Boek, E. S., Padding, J. T., Anderson, V. J., Tardy, P. M. J., Crawshaw, J. P. and Pearson, J. R. A. "Constitutive equations for extensional flow of wormlike micelles: stability analysis of the Bautista-Manero model", J.

Non-Newtonian Fluid Mech. **126**, 39-46 (2005).

Calderbank, P. H., Johnson, D. S. and Loudon, J. "Velocity fields around spheres and bubbles investigated by laser-Doppler anemometry", Chem. Eng. Sci. **25**, 235-256 (1970).

Caram, Y., Bautista, F., Puig, J. E. and Manero, O. "On the rheological modeling of associative polymer", Rheol Acta, **46(1)**, 45-47 (2006).

Caswell, B., Manero, O. and Mena, B. "Recent developments o the slow viscoelastic flow past spheres and bubbles", Rheology Reviews 2004, The bristish society of rheology, D.M. Binding and K. Walters (Editors), pp 197-223, (2004).

Callister, D.W. "Materials science and engineering: an introduction", Jhon & Wiley, New York, (1994).

Chen, S. and Rothstein, J. P. "Flow of a wormlike micelle solution past a falling sphere", J. Non-Newtonian Fluid Mech. **116**, 205–234 (2004).

Chhabra,R. P. "Bubbles, Drops and Particles in Non-Newtonian fluids", CRC Press, Boca Raton (1993).

Chhabra, R.P. and Uhlherr, P. H. T. "The influence of fluid elasticity on wall effects for creeping sphere motion in cylindrical tubes", Can. J. Chem. Eng. **66**, 154 (1988).

Chhabra, R.P., Tui, C. and Uhlherr, P. H. T. "A study of wall effects on the motion of a sphere in viscoelastic fluids", Can. J. Chem. Eng. **59** 771 (1981).

Chhabra, R.P. "Bubbles, drops and particles in non-Newtonian fluids". Taylor and Francis, New York, Chapter 6 and 11, (2006).

Clift,R., Grace,J. R. and Weber, M. E. "Bubbles, Drops and Particles", Academic Press, New York (1978).

Funfschilling,D. and Li, H. Z. "Flow of non-Newtonian fluids around bubbles: PIV measurements and birefringence visualisation", Chem. Eng. Sci. **56**, 1137 (2001).

Hammerton, D. and Garner, F. H. "Gas Absorption from Single Bubbles", Transactions of the Institution of Chemical Engineers, **32**, S18-S24 (1954).

Hadamard, "Mouvement permanent lent d' une sphè liquide et visqueuse dans un liquide visqueux"J. C. R. Acad. Sci., Paris **152** 1735 (1911).

Happel, J. and Brenner, H. "Low Reynolds Number Hydrodynamics", Englewood Cliffs, N J: Prentice-Hall (1973).

Harris, J. "Rheology and non-Newtonian flow", Longman, London, (1997).

Hassagar, O. "Negative wake behind bubbles in non-Newtonian liquids", Nature **279**, 402 (1979).

Herrera-Velarde,J. R., Zenit, R., Chehata, D. and Mena, B. "The flow of non-Newtonian fluids around bubbles and its connection to the jump discontinuity", J. Non-Newtonian Fluid Mech. **111**, 199-209 (2003).

Jayaraman, A. and Belmonte, A. "Oscillations of a solid sphere falling through a wormlike micellar fluid", Phys. Rev. E **67**, 065301(R) (2003).

Kastner, U. "The impact of rheological modifiers on water-borne coatings", Colloids and surface A: Physicochemical and engineering aspects **183–185**, 805–821 (2001).

Kee, D. De and Chhabra, R.P. "Transport processes in bubbles, drops and particles". Taylor and Francis, New York, Chapters 4 and 13, (2002).

Leal,L. G., Skoog, J. and Acrivos, A. "On the motion of gas bubbles in a viscoelastic fluid", Can. J. Chem. Eng. **49**, 569-575 (1971).

Levich, V. G."Physico-Chemical Hydrodynamics", Prentice-Hall, Englewood Cliffs, NJ, 436 (1962).

Li, H. Z., Frank, X., Funfschilling, D. and Mouline, Y. "Towards the understanding of bubble interactions and coalescence in non-Newtonian fluids: a cognitive approach", Chem. Eng. Sci. **56**, 6419 (2001).

Liu, Y. J., Liao, T. Y. and Joseph, D. D. "A two-dimensional cusp at the trailing edge of an air bubble rising in a viscoelastic liquid", J. Fluid Mech. **304**, 321-342 (1995).

Manero, O., Bautista, F., Soltero, J. F. A. and Puig, J. E. "Dynamics of worm-like micelles: the Cox-Merz rule", J. Non-Newtonian Fluid Mech. **106**, 1-15 (2002).

McKinley, G. H. "Steady and Transient Motion of a Sphere in an Elastic Fluid", Transport Processes in Bubbles, Drops and Particles, Chapter 14 (Eds: R. Chhabra and D. DeKee) Taylor and Francis (2002).

Mendoza-Fuentes, A. "Diseño, construcción y aplicación de un equipo de asentamiento de partículas en un polímero asociativo", Facultad de Química, Universidad Nacional Autónoma de México, (2006).

Morrison, F.A. "Understanding Rheology", Oxoford university press, New York, (2001).

Rodrigue, D., De Kee, D. and Chan Man Fong, C.F. "Bubble velocities: further developments on the jump discontinuity", J. Non-Newtonian Fluid Mech. **79**, 45 (1998).

Rodrigue, D., De Kee, D. and Chan Man Fong, C.F."An experimental study of the effect of surfactants on the free rise velocity of gas bubbles", J. Non-Newtonian Fluid Mech. **66**, 213 (1996).

Rodrigue, D. Private Communication (2006).

Rybczynski, "Uber die Fortschreitende Bwegung einer-ussigen Kugel in einem zahen Medium". W. Bull. Int. Acad. Sci. Cracovie, Ser. A, 40 (1911).

Schlichting, H."Boundary Layer theory", McGraw-Hill, New-York (1964).

Sigli, D. and Coutanceau, M. "Effect of finite boundaries on the slow laminar isothermal flow of a viscoelastic fluid around a spherical obstacle", J. Non Newtonian Fluids Mechanics **2**, 1 (1977).

Soltero, J.F. A., Bautista, F., Puig, J. E. and Manero, O. "Rheology of Cetyltrimethylammonium p-Toluenesulfonate-Water System. 3. Nonlinear Viscoelasticity". Langmuir **15** 1604 (1999).

Soto, E., Guojon, C., Zenit, R. and Manero, O. "A study of velocity discontinuity for a single air bubbles rising in an associative polymer", Phys. Fluids **18**, 121510 (2006).

Stokes, G. G. "Mathematical and Physical Papers", Cambridge Univ. Press, England (1880).

Tam, K. C., Guo, L., Jenkins, R. D. and Bassett, D. R. "Viscoelastic properties of hydrophobically modified alkali-soluble emulsion in salt solutions", Polymer, **40**, 6369-6379 (1999).

Taylor, T. D. and Acrivos, A. "On the deformation and drag of a falling viscous drop at low Reynolds number", J. Fluid Mech. **18**, 466–476 (1964).

Uhlherr, P. H. T., Le, T. N. and Tiu, C. "Characterization of Inelastic Power-law Fluids Using Falling Sphere Data", Can. J. Chem. Eng., **54**, 497-502 (1976).

Walters, K. and Tanner, R.I. "The motion of a sphere trough elastic fluid" in "Transport processes in bubbles, drops amd particles", (R.P. Chhabra and

D. De Kee), Hemisphere Pub., (1992)

Winnik, M. A. and Yekta, A. "Associative polymers in aqueous solution", A. Curr. Opin. Colloid Interface Sci. **2**, 424 (1997).

Zana, E. and G. Leal, L. "The dynamics and dissolution of gas bubbles in a viscoelastic fluid", Int. J. Multiphase Flow **4**, 237 (1978).

Appendix Meetings

Paper, Talks, posters and video.

A study of velocity discontinuity for single air bubbles rising in an associative polymer

E. Soto, C. Goujon, R. Zenit, and O. Manero
Instituto de Investigaciones en Materiales Universidad Nacional Autónoma de México, Apdo. Postal 70-360, México D.F. 04510, México

(Received 2 May 2006; accepted 10 August 2006; published online 8 December 2006)

The motion of air bubbles in aqueous solutions of a hydrophobic alkali-swellable associative polymer is studied in this work. The associative nature of these polymer systems dictates their rheological properties: for moderate values of the shear rate, the formation of structure can lead to a shear-thickening behavior and to the appearance of first normal stress difference. For larger shear rates, the polymer associations can be broken, leading to shear thinning. In general, these fluids show a Newtonian behavior for small values of the shear rate, but behave as viscoelastic liquids for large shear rates. Experimental results show the appearance of a critical bubble volume at which a discontinuity in the relation velocity-volume occurs; however, the velocity increase found in this case is not as large as that previously reported for the case of shear-thinning viscoelastic fluids. The discontinuity is associated with a significant change of the bubble shape: before the critical volume, the bubbles are convex spheroids, while past the critical volume a sharp cusped end appears. The appearance of the tail is also associated with the appearance of an inflection point (change of curvature) on the bubble surface. Moreover, since the rheology of the liquids is measured it was found that the discontinuity, and hence the change of shape, occurs when the elastic nature of the liquid first manifests itself (appearance of a first normal stress difference). A comparison of the measured velocities for small bubbles with predictions from a Stokes-Hadamard law shows a discrepancy. The Newtonian viscosity measured in a viscometric flow was smaller than that determined from a falling-ball arrangement. Considering the viscosity measured under this nonviscometric flow, the comparison between theory and experiments was very good for bubbles having volumes lower than the critical one. Moreover, due to the importance of the elasticity, and due to the change of the shape of the bubble, a dimensionless number formed as the ratio of elastic to surface tension forces clearly defines the change of the behavior for the bubbles rising in these fluids. Finally, a photographic study of the peculiar shapes of the bubble tails, tip-, and *edge*-streaming phenomena is presented. To our knowledge, experiments in this class of fluids have not been reported to date. © *2006 American Institute of Physics*. [DOI: 10.1063/1.2397011]

I. INTRODUCTION

The study of the motion of air bubbles in liquids has received much attention because of its fundamental and practical importance. For the case of Newtonian liquids, there is a vast collection of investigations that report interesting behaviors in many regimes.[1] The understanding of such a system is quite complete. For the case of the motion of gas bubbles in non-Newtonian liquids, there are several unexpected phenomena that remain to be fully understood.[2,3]

Among the peculiar phenomena observed in the case of non-Newtonian liquids, of particular interest is the so-called *bubble velocity discontinuity*. In a Newtonian fluid, the magnitude of the rising velocity of a gas bubble is proportional to the bubble size and the relation velocity-volume is monotonically increasing. For the case of non-Newtonian liquids, many authors[4–10] have reported that there exists a critical value of the volume of the bubble for which a discontinuity of the velocity occurs: the bubble velocity increases monotonically as the bubble size increases, but once a critical volume is reached, the bubble velocity increases in a discontinuous manner. In other words, the bubble velocity can increase many times for a slight increase of the bubble volume. Astarita and Apuzzo[4] were the first to report that the ratio of the velocity after and before the jump ranged from 2 to 6, depending on the polymer present in the solution. They argued that this discontinuity of the velocity was a result of a transition from the Stokes regime to the Hadamard regime (a change from a rigid to a free interface). However, it can be shown that the velocity increase resulting from such a change of the boundary conditions would be equal to 1.5. Due to the fact that no discontinuity of the velocity has been reported to occur for the case of falling spheres, some authors[5–7] have supported this argument, even though it does not predict correctly the increase of velocity. Astarita and Apuzzo[4] also pointed out that the shape of the bubbles changed before and after the velocity discontinuity.

Rodrigue *et al.*[8] proposed an explanation for the discontinuity. They argued that it results from a balance between elastic and Marangoni instabilities, providing another major difference between Newtonian and non-Newtonian hydrodynamics. They have also studied the effect of surfactants in the liquid,[9] and concluded that surface active agents as well

as elastic forces must be simultaneously present in order to generate a sudden jump in velocity.

Recently, Herrera-Velarde *et al.*[10] studied the velocity field around bubbles before and after the critical volume by means of a particle image velocimetry (PIV) technique. They reported that the appearance of the velocity discontinuity is associated with the presence of the so-called *negative wake*: for small bubbles (with a volume smaller than the critical volume) the flow is similar to that of a bubble moving in a Newtonian liquid; for large bubbles (with a volume larger than the critical volume), the flow is strongly different and a negative wake is present. The wake is called "negative" because the velocity, very close to the trailing end, is in the direction of the motion of the bubbles; a short distance away from the trailing end, the velocity reverses direction. For a bubble rising in a Newtonian liquid, the wake is normal, as the velocity in the wake is in the same direction as the motion of the bubble. Hassagar[11] was the first to observe this behavior for bubbles and coined the term "negative wake." Negative wakes have also been observed for spheres falling in viscoelastic liquids.[12] Many explanations have been proposed to explain the appearance of this discontinuity; however, a complete self-consistent explanation is not yet available.

In order to acquire certain desired rheological characteristics in commercial products, rheology modifiers are used, i.e., surfactants (worm-like micellar systems), polymers (cellulose derivates), and hydrophobically modified or associative polymers (hydrophobically modified hydroxyethylcellulose).[15,16] In particular, surfactants and associative polymers are formed by two main parts: one hydrophobic and the other hydrophilic. In aqueous solutions, the hydrophilic part is surrounded by water while the hydrophobic parts associate themselves with forming agglomerates called micelles. The formation and rupture of these structures dictate the rheological behavior of these solutions. In general, for associative polymers and surfactants, modifications of rheological properties can be accomplished with smaller concentrations, compared to those needed for ordinary polymers, hence reducing the amount of residual products.

In this investigation, experiments to determine the terminal velocity of air bubbles in solutions of a hydrophobically modified alkali soluble polymer (HASE) were conducted. HASE is an associative polymer formed by a hydrophilic principal backbone and some pendant hydrophobic groups in a comb-like arrangement.[15,16] HASE solutions display complex rheological properties because they exhibit a shear thickening and/or thinning in addition to viscoelasticity. At some specific concentrations HASE solutions have a region of constant viscosity, but with the presence of elasticity, it is possible to isolate elastic and shear-thinning effects. Another advantage of using these liquids is that they serve as model systems.[17,18]

To our knowledge, experiments to determine terminal velocities of gas bubbles on HASE-type fluids have not been reported to date. Belmonte[19] reported experimental results of gas bubbles rising in worm-like micellar liquids, which share a similar complex rheology as the HASE system presented here. For these solutions, the bubbles develop a cusped edge and, for some conditions, self-trajectory oscillations appeared. Some authors[20–22] reported that the motion of settling spheres in micellar-type fluids also shows trajectory oscillations.

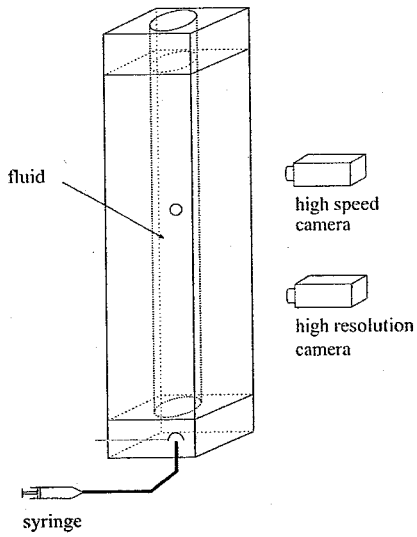

FIG. 1. Experimental device to study the motion of air bubbles in a liquid. Two cameras (one high speed and one high resolution) allow us to determine the velocity and shape of the bubble.

In this paper, we present experimental results for single bubbles rising in a HASE associative polymer. In Sec. II, the experimental methods are presented. The theory concerning bubbles moving in a Newtonian liquid at low Re is briefly summarized (Sec. III). After presenting the experimental results (Sec. IV) and their comparison with the theory (Sec. V), we present an explanation of the discontinuity of the velocity based on the rheological properties of the liquid. In the last section (Sec. VI), we present a short study of the shape of bubble tails that appears after the discontinuity.

II. EXPERIMENTAL METHODS

A. Materials and experimental setup

To analyze the motion of air bubbles in a liquid, the experimental device, presented in Fig. 1, was used. A certain volume was placed in a cap with a syringe, and by turning the cap, the bubble was released to move upwards in the inner tube. The width of the inner tube (D=9 cm) was enough to minimize wall effects. In all cases, the ratio between the diameter of the bubble and the diameter of the inner tube was smaller than 0.1. The inner tube length (L=60 cm) was long enough for the bubbles to reach a stable terminal velocity. In the outer square tube, a liquid with the same refraction index as the solution present in the inner tube was placed to reduce the refraction effects. Several HASE concentrations were tested and their rheological characterization is presented in the next part. Since, it has been shown that the velocity of the bubbles can be dependent on the injection frequency,[9] a 5-min interval was left between two consecutive bubbles to avoid this effect.

TABLE I. Properties of the bubbles (diameter d and equivalent shear rate $\dot{\gamma}=U/r$) in different solutions.

Fluid $n°$	% HASE	d (mm)	$\dot{\gamma}$ (s^{-1})
1	1.2%	0.3–9.4	1–42
2	1.5%	3.3–7.6	2–16
3	1.7%	2.5–8.7	1–10

TABLE II. Properties of the solutions: viscosity μ, surface tension σ, and coefficients a and b in the expression of the first normal stress difference, $N_1=a\dot{\gamma}^b$.

Fluid $n°$	% HASE	μ (Pa s)	σ (mN m)	a	b	Range of $\dot{\gamma}$
1	1.2%	0.22±0.009	38.41±0.34	0.2078	1.3097	0.1–100
2	1.5%	1.14±0.005	36.93±0.23	1.1449	1.3192	0.1–100
3	1.7%	3.34±0.04	55.55±0.38	2.3728	1.3289	0.1–50

HASE (Primal TT-935) is supplied by Rohm and Haas. Aqueous solutions were prepared at 1.2, 1.5, and 1.7% by weight in distilled water and left to rest for 48 h. A 0.5-M solution of 2-amino,2-methyl propanol (AMP), supplied by Aldrich, was used to adjust the pH to 9.0, at which the viscosity is a function of pH peaks. Once the solutions were free of bubbles, the rheological and surface tension properties were determined.

B. Measurement methods

1. Bubble shape and velocity

The bubble terminal velocity and shape were determined using two cameras. The first one was a high-speed camera (RedLake MotionScope Model 1000), which measures the velocity of the bubble using spatiotemporal diagrams. The error in the bubble velocity determination was smaller than 1.5 mm/s. The second one was a high-resolution camera (6 megapixels, Fuji FinePix S1pro), which determines the bubble's geometric characteristics (shape and volume) by image analysis. The bubble volume was determined assuming axial symmetry. Comparing the value of a known injected volume with that obtained by image analysis, the error is smaller than 2%. An average shear rate $\dot{\gamma}$ was defined to characterize the rheological properties of the fluid as the ratio of the terminal velocity U of the bubble to its spherical equivalent radius r: $\dot{\gamma}=U/r$. As shown elsewhere, the mean value of the shear rate $\dot{\gamma}$ can be given by U/r for the flow around a spherical bubble at low Reynolds number.[23,24] The experimental range of the bubbles diameter and mean shear rates are presented in Table I.

The flow field around the bubble on the symmetry plane was determined using PIV, with a commercial device provided by Dantec Dynamics. The light source was a 532-nm laser; fluorescent seeding and filters were used to avoid reflections within the air-liquid interface. More details about this technique can be found in Ref. 10.

2. Rheological properties

The rheological properties of the HASE solutions under simple shear were determined in a stress-controlled rheometer (TA Instruments), using a 40-mm $1°59'$ cone and plate fixture with a Peltier temperature-control system.

The HASE solutions tested behave as Newtonian fluids (at small shear rates, viscosity remains constant and normal stresses are negligible; Fig. 2). From 0.1 to 50 s^{-1}, the normal stresses are measurable while the viscosity remains almost constant. For all concentrations, a slight shear-thickening behavior can be observed for small ranges of shear rate (for 1.2% HASE, $6<\dot{\gamma}<36$; for 1.5% HASE, $2<\dot{\gamma}<12$; for 1.7% HASE, $1<\dot{\gamma}<3.7$). For large shear rates and depending on the concentration, the fluids exhibit a shear-thinning behavior: the viscosity decreases with the

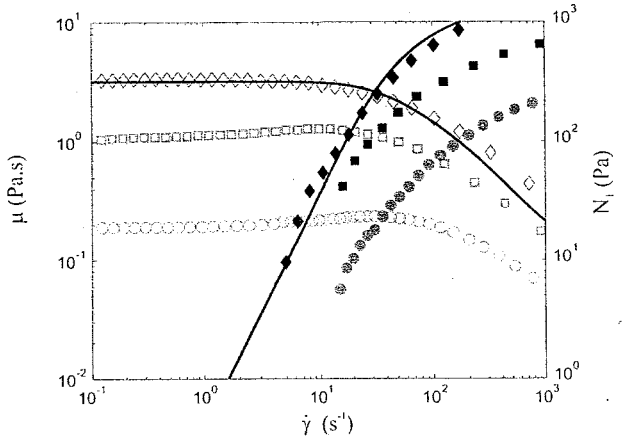

FIG. 2. Shear viscosity μ (empty symbols) and first normal stress difference N_1 (solid symbols) as a function of the shear rate for different percentages of HASE (○) 1.2%; (□) 1.5%; (◇) 1.7%. The bold lines show predictions of the Bautista-Manero model for 1.7% of HASE (Ref. 18).

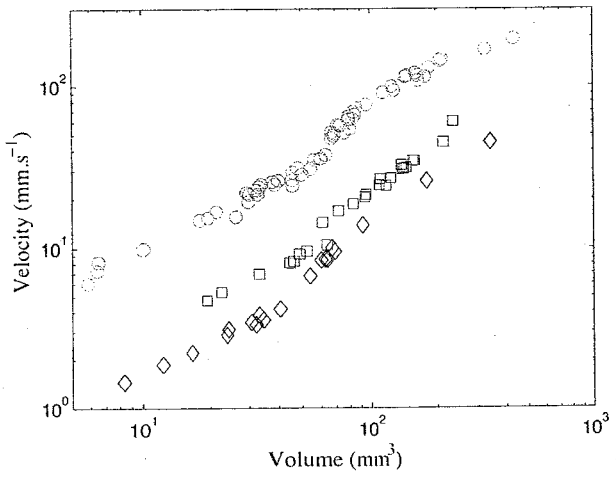

FIG. 3. Bubble velocity as a function of bubble volume for different percentages of HASE: (○) 1.2%; (□) 1.5%; (◇) 1.7%. There is a discontinuity of the bubble velocity for volumes equal to V_c (1.2%: $V_c\simeq 65$ mm^3; 1.5%: $V_c\simeq 60$ mm^3; 1.7%: $V_c\simeq 50$ mm^3). The critical volume decreases with an increase in HASE concentration.

shear rate and the first normal stress difference increases with the shear rate. In general, for a given shear rate, the viscosity and the first normal stress difference increase with HASE concentration, and the critical value of the shear rate at which normal stresses appear decreases with increasing HASE concentration.

For the first normal stress difference, it is possible to fit the data to a power law, $N_1 = a\dot{\gamma}^b$. The coefficients a and b, and the range of shear rate for which this assumption is valid, are reported in Table II. The predictions of the model by Bautista *et al.*[18] are shown with experimental data for the 1.7% HASE solution (Fig. 2). As analyzed elsewhere,[25] this model accounts for the breakage-reformation process of the structure of associative polymers under flow. The model predicts a maximum in the extensional viscosity at a strain rate corresponding to that of the onset of normal stresses and the shear-thinning region of the shear viscosity.

The surface tension of these liquids was measured with a Wilhelmy balance (Sigma 700) using a DuNouy ring (Table II).

III. THEORY FOR SPHERICAL BUBBLES

A brief summary of the theory for Newtonian flow around spherical bubbles is presented. In general, the motion of a gas bubble is mainly determined by the hydrodynamic conditions (properties of the liquid, diameter of the bubble) and by the boundary condition on the bubble surface.

At very low Reynolds numbers (creeping flow), the flow is dominated by viscous effects. The equations of motion can, in principle, be solved rigorously and hence the drag can be calculated. By equating the drag and the buoyancy, the velocity-volume relationship can be obtained. The interface of a gas bubble may be considered between the two extreme cases of a free and a rigid interface.[26,27] If the gas is assumed to be inviscid, the tangential stress τ is zero at the free interface. For a rigid interface, the velocity of the interface is equal to the velocity of the center of gravity of the bubble. In other words, the no-slip boundary condition holds at the bubble surface. For either case, the drag force on a spherical bubble in creeping flow can be calculated[28–31] according to

$$C_d = \begin{cases} 24/\mathrm{Re}, & \text{rigid interface,} \quad \text{Stokes drag} \\ 16/\mathrm{Re}, & \text{free interface,} \quad \text{Hadamard-Rybczynski drag} \end{cases}$$

Hence, the terminal velocity for each case is

$$U_{\mathrm{Stokes}} = \frac{\rho g}{18\mu} d^2, \tag{1}$$

$$U_{\mathrm{Hadamard}} = \frac{\rho g}{12\mu} d^2, \tag{2}$$

where d is the equivalent diameter of the bubbles (m), ρ is the density of the liquid (kg m^{-3}), g is the gravitational constant (g=9.81 ms^{-2}), and μ is the viscosity of the liquid (Pa s).

In the case of very small bubbles rising in the HASE solution, the shear rate is very small, and then the liquid can be considered as Newtonian: there are no normal stresses and the viscosity is constant. However, it is very difficult to determine the surface boundary condition (rigid or free). As an example, a "dirty" bubble will not have a free or a rigid interface; hence, one would expect to observe a behavior between the two regimes.

IV. EXPERIMENTAL RESULTS

A. Bubble terminal velocity and velocity field

Measurements of the terminal velocity for the three HASE solutions are presented in Fig. 3. There is a critical volume V_c for which a velocity discontinuity appears. The value of this critical volume decreases with an increase in HASE concentration. These results are in agreement with those obtained by Herrera-Velarde *et al.*[10] In all cases, the slope of the velocity-volume relation is larger for large bubbles (for $V > V_c$) than for small bubbles (for $V < V_c$). Moreover, for a given volume, the terminal velocity decreases with an increase of HASE concentration (due to the increase of viscosity). It is important to observe that the increase in velocity after the discontinuity is significantly lower than that reported previously for aqueous shear-thinning viscoelastic liquids.[10,13] A distinctive feature of the discontinuity of the velocity-volume relation, for the HASE solutions, is that the slope of the curve, defined by dU/dV (where U is the velocity and V is the volume), increases significantly past the critical volume. Clearly, the value of dU/dV at the discontinuity is larger than the values corresponding for the nonjump condition (Table III). Moreover, the amplitude of the discontinuity decreases as the percentage of HASE increases.

Flow visualization around bubbles before and after the discontinuity using the PIV technique are presented in Figs. 4 and 5. For air bubbles with volumes smaller than the criti-

TABLE III. Velocity increase, dU/dV, at the volume for which the discontinuity occurs. $dU/dV_{\mathrm{Hadamard}}$ and dU/dV_{Stokes} are calculated from Eqs. (1) and (2).

% HASE	dU/dV	$dU/dV_{\mathrm{Hadamard}}$	dU/dV_{Stokes}
1.2%	2.52	0.43	0.28
1.5%	0.55	0.14	0.09
1.7%	0.188	0.06	0.04

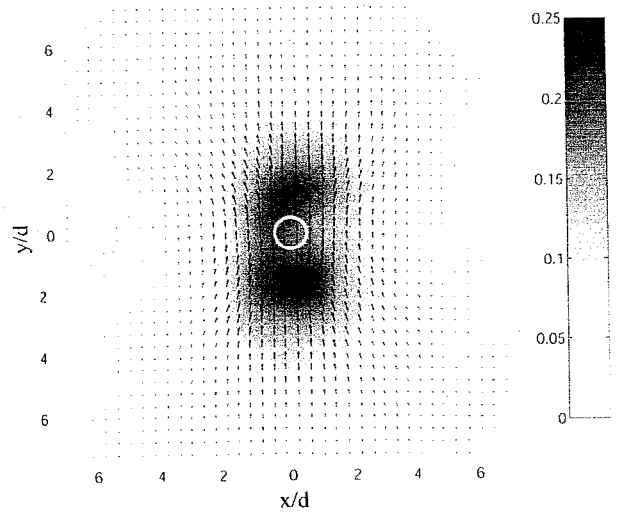

FIG. 4. Flow around a rising bubble with volume below the critical one (V=4.2 mm^3; U=1.1 mm s^{-1}; HASE 1.5%).

cal one, V_c, the fluid at the front and at the rear of the bubble is moving in the same direction of the bubble (Fig. 4). For bubbles with a volume larger than the critical one, V_c, the flow around the bubble is drastically different (Fig. 5). The flow at the front of the bubble is in the same direction of the bubble motion. At the rear of the bubble, the fluid is moving in the opposite direction of the bubble motion. This phenomenon is called negative wake and was previously reported elsewhere[3,11,32,33], and more recently in Ref. 10. The negative wake is a manifestation of importance of the elastic effects in the bubble motion. Presumably, the elasticity of the liquid is an important factor for the discontinuity to appear. This argument will be further discussed later.

B. Bubble shape

The velocity discontinuity can be related to the bubble shape. Figures 6–8 show bubbles for the three solutions with volumes smaller and larger than the critical one V_c. Clearly, there is a very significant change of the shape related to the appearance of the velocity jump.

For bubbles with a volume much smaller than the critical volume V_c, the shape is nearly spherical. With a small increase in volume, a slight deformation on the rear part of the bubble is observed. In all cases, for volumes smaller than V_c, the shape of the bubbles is convex all around, whereas for bubbles with a volume larger than the critical volume V_c, the shape is concave in the trailing end: the shape presents an inflection point. Figure 9 shows a comparison of the shape of a bubble before and after the jump. The shape in the front region is nearly the same, whereas it changes significantly in the back region. Moreover, the formation of a sharp cusp can be clearly observed. At the tip of the cusp, a long (few centimeters) and very thin (tens of micrometers) tail forms in all cases. Using two cameras acting simultaneously, it was possible to obtain a view of the tail from two sides. The cusps and tails immediately after V_c are axisymmetric. However, for volumes larger than V_c, this is no longer the case. Non-axisymmetric tails are shown and discussed in Sec. VII.

V. COMPARISON OF EXPERIMENTS AND THEORY FOR SMALL BUBBLES: TERMINAL VELOCITY

The viscosity of the HASE solutions displays a Newtonian region at small shear rates $\dot{\gamma}$. For small Reynolds numbers, one can attempt to compare the measured terminal velocities with those predicted for the Stokes-Hadamard drag [Eqs. (1) and (2)].

Figure 10 shows a comparison of experimental results obtained for fluid 1 (1.2% HASE). The predictions [Eqs. (1) and (2)] consider the measured zero shear-rate viscosity.

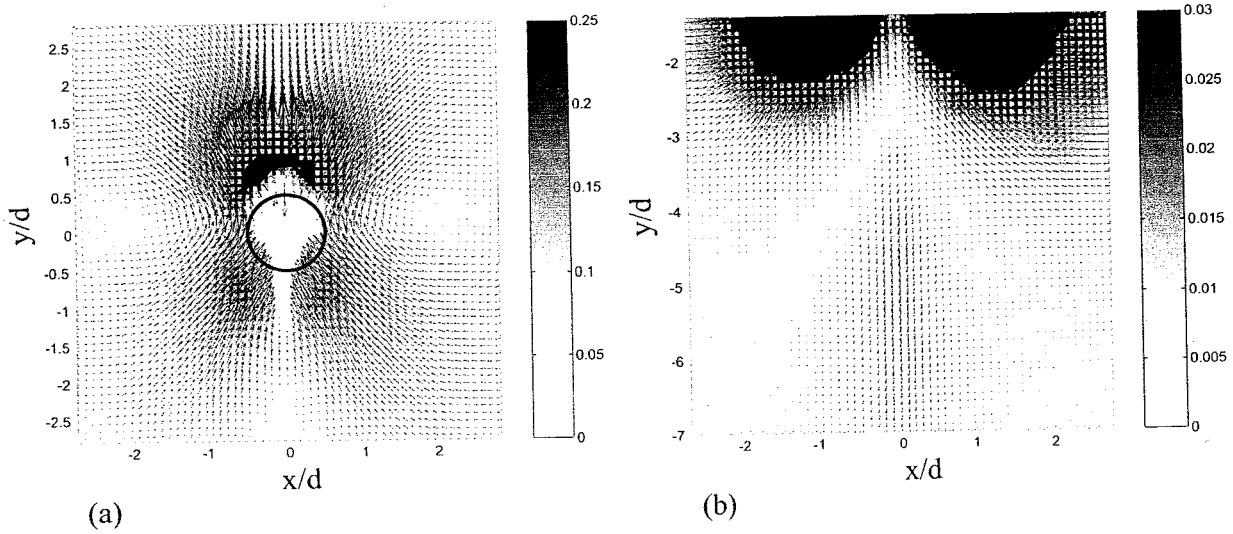

FIG. 5. Flow around a rising bubble with volume above the critical one. (a) Flow around the bubble. The flow is very similar to the flow observed for a bubble with a volume smaller than V_c. (b) At the rear part of the bubble, the negative wake can be seen (V=239 mm^3; U=54.6 mm s^{-1}; HASE 1.5%).

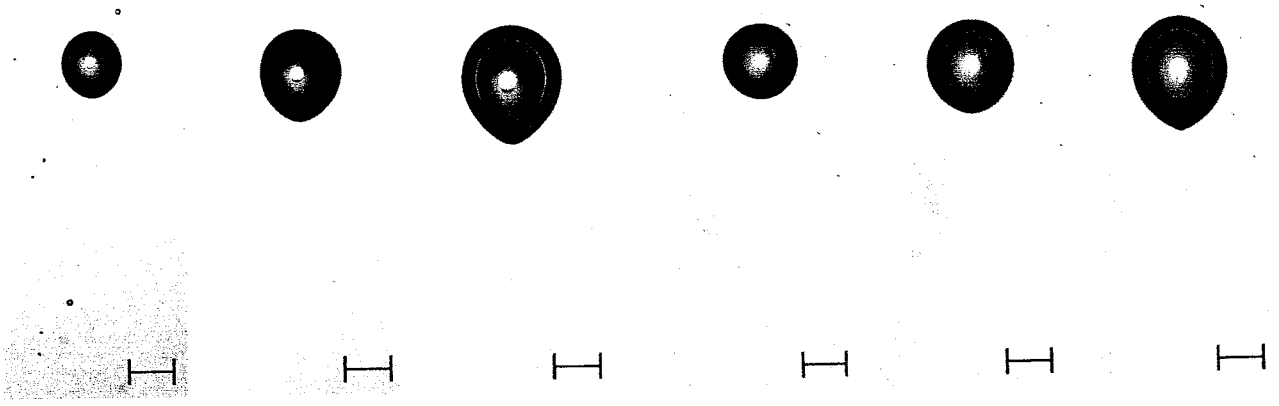

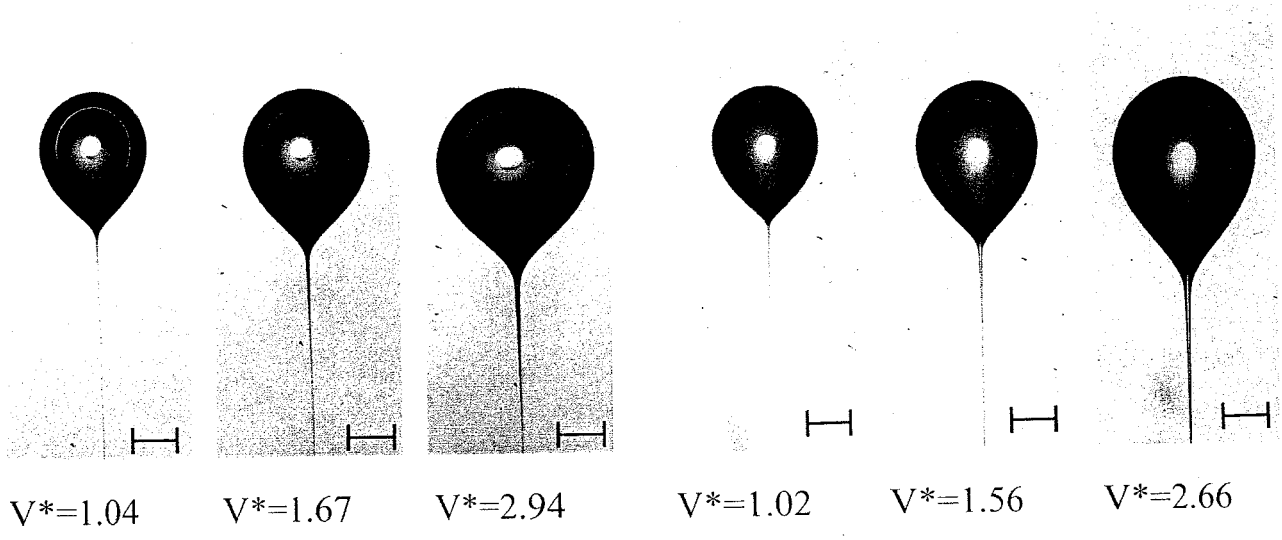

FIG. 6. Bubble shapes for different values of the dimensionless volume $V^*=V/V_c$ for %HASE=1.2, with V_c=65 mm^3. The small bubbles are almost spherical. For larger volumes (for $V^*>1$), the shape of the bubbles is concave with a very thin and long tail at the rear part of the bubble. The scale represents 2 mm.

FIG. 7. Bubble shapes for different values of the dimensionless volume $V^*=V/V_c$ for %HASE=1.5, with V_c=60 mm^3. The scale represents 2 mm.

Clearly, the disagreement among the two sets of data is apparent. The rheometric flow (simple shear), in which the viscosity was measured, contrasts that of the flow around the bubble. To improve the predictions, the viscosity of the liquid was obtained from a simple falling-bead setup. The effective viscosity in this case inferred from

$$\mu=\frac{2}{9}\frac{r^2\Delta\rho g}{U},$$

where r is the bead radius (m), $\Delta\rho=\rho_{\text{bead}}-\rho_{\text{liquid}}$ is the density difference between bead and liquid (kg m^{-3}), g is the gravitational constant (g=9.81 m s^{-2}), and U is the terminal settling velocity of the sphere m s^{-1}.

The experiments are conducted by varying the diameter of the glass beads from 3 to 6 mm. In all the cases, the Reynolds number is smaller than 1. The shear rate is also small, corresponding to shear rates within the Newtonian region of the rheometric flow curve. In addition, the ratio d_s/D is smaller than 0.07 (d_s is the diameter of the bead and D is the diameter of the test section). The viscosity obtained from these experiments is constant for shear rates between 0.2 and 10 s^{-1}. The results are presented in Table IV. The viscosity obtained from falling-bead experiments is in all cases larger than that obtained under simple shear. The ratio of these viscosities (α) as a function of HASE percentage is shown in Table IV. This ratio decreases with HASE concentration. This behavior can be explained by two reasons.

First, in these experiments, wall effects are present. For Newtonian fluids, the drag correction factor reduces to the well-known Faxén correction,[35] which is commonly expressed in the form

$$K_N(a/R)=\frac{1}{1-f(r/R)}=\frac{U_{\text{Stokes}}}{U} \tag{3}$$

with

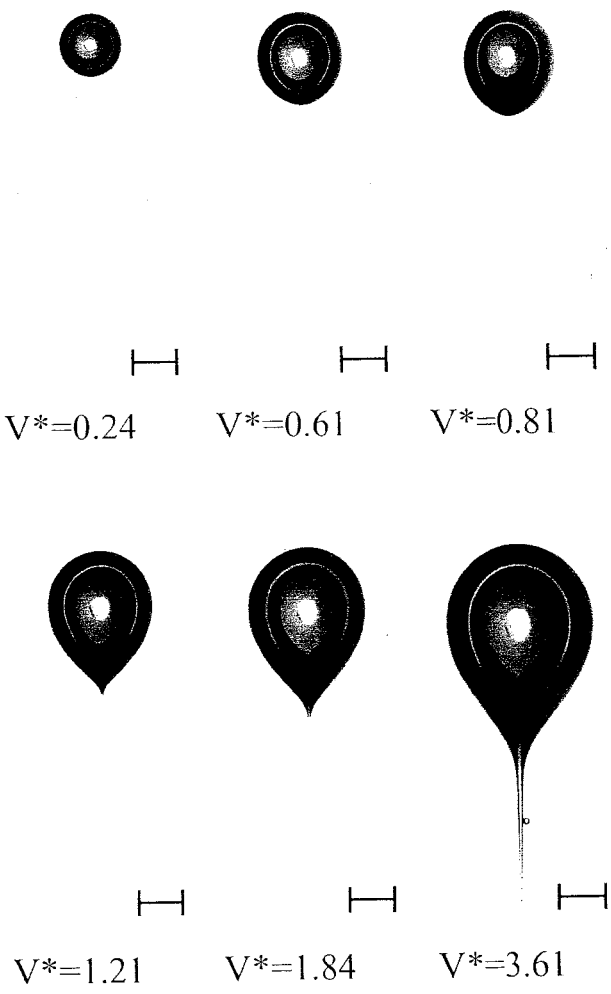

FIG. 8. Bubble shapes for different values of the dimensionless volume $V^*=V/V_c$ for %HASE=1.7, with $V_c=50$ mm^3. The scale represents 2 mm.

$$f(r/R) = 2.104\,44(r/R) - 2.088\,77(r/R)^3 + 0.948\,13(r/R)^5 + 1.372(r/R)^6 - 3.87(r/R)^8 + 4.19(r/R)^{10} + \cdots, \quad (4)$$

where r is the radius of the falling bead and R is the container radius. This relation is only valid in the case of a Newtonian fluid for Reynolds number smaller than 1. It has been shown[36] that "for moderate Deborah Numbers De, wall effects appear to be less important than in the motion of the corresponding Newtonian fluid." In our experiments, the Deborah number lies between 0.5 and 1.6, implying that the drag correction factor is smaller than the one calculated in the case of a Newtonian fluid.[37] In these HASE solutions, a r/R value of 0.07 corresponds to $K_N(r/R)=1.16$. It implies a viscosity increase of 1.16. Moreover, the wall correction factor for elastic, constant-viscosity fluids[38] is given by $f(r/R)=1-0.17r/R$ for Deborah numbers larger than 0.2, which corresponds in our case to $K_N(r/R)=1.006$. The wall effect contributes to a small increase in viscosity obtained from falling-bead experiments over that obtained in simple shear. However, the difference between the two viscosities is within a factor of 2.

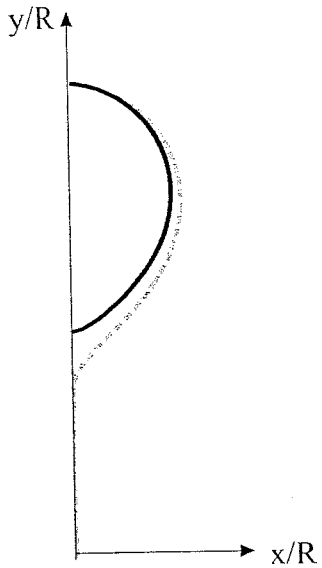

FIG. 9. Bubble shapes before (continuous line) and after (dashed line) the jump. The shape does not change in the front part of the bubble, whereas it changes in its back part ($V_{\text{before}}=49.2$ mm^3; $V_{\text{after}}=61.2$ mm^3; 1.5% HASE).

The second reason is that, conceptually, the flow around a bubble can be divided into three regions: a simple shear region at the equator, a simple extensional region at the rear, and a biaxial extensional region at the front. The extensional components lead to extra stresses that slow the sphere motion down. But this extensional flow depends on the Reynolds number. For large values of the Reynolds number the extensional components will be more important; as a consequence, the difference between the two viscosities will increase.

The ratio of the viscosity estimated from falling-bead data to the viscometric viscosity decreases with HASE concentration (Table IV). In addition to the wall effects, which decrease the terminal velocity and hence increase the viscosity, it is necessary to include the extensional flow contributions. Under extensional flow, models[17,18,39] predict a region of extensional thickening at extension rates of the order of the inverse of the main relaxation time. This region coincides with the onset for measurable normal stresses in shear flow, closely related to the appearance of the velocity discontinuity. The extensional flow contribution further retards the motion of the falling bead, increasing the mentioned viscosity ratio.

The experimental and theoretical results obtained with the two viscosity measurements are compared. The results are presented in Fig. 10. For small bubbles that are almost spherical, the experimental measurements lie between the two limiting cases of Hadamard and Stokes laws with a viscosity calculated from the falling-bead experiments. Therefore, the bubble interface can neither be considered fully contaminated nor clean. We note that the comparison is good for bubbles with volumes smaller than the critical volume V_c.

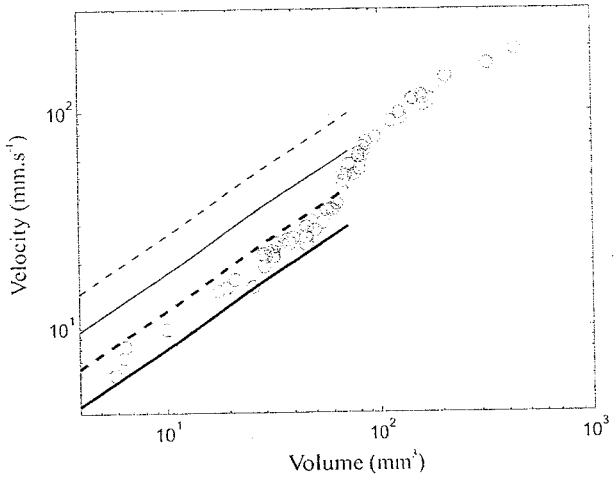

FIG. 10. Bubble velocity as a function of bubble volume, 1.2% HASE. The lines are the theoretical predictions obtained from the Stokes (continuous lines) and Hadamard (dashed lines) laws: (thin lines) $\mu=\mu_{\text{rheometer}}$; (thick lines) $\mu=\mu_{\text{fall}}$.

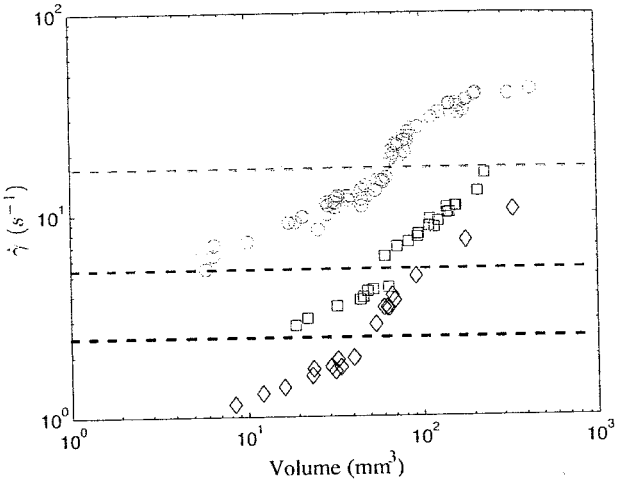

FIG. 11. Mean shear rates $\bar{\dot{\gamma}}$ as a function of the volume for different percentages of HASE: ○ 1.2%; □ 1.5%; ◇ 1.7%. The dashed lines represent, for each percentage of HASE, the shear rate for which the normal stresses are measurable.

Above V_c, the bubbles are no longer spheroidal and develop a long tail. The results for the other fluids and their comparison with the theory are not presented here, but the agreement between theory and experiments is equally good. Contrary to the measurement of the viscosity by falling-bead experiments, the simple shear rheological measurements do not take into account the uniaxial and biaxial deformations. This explains why the behavior of small bubbles rising in a viscoelastic fluid is better described using a falling-sphere measurement of the viscosity.

VI. INTERPRETATION

In the case of bubbles rising in an associative polymer, it has been shown that there is a critical value of the volume at which a discontinuity in the velocity-volume curve occurs. The analysis of the bubble shape shows that for small bubbles (with a volume smaller than the critical value), the shapes of the bubbles are convex: the bubbles are spherical or spheroidal. For volumes larger than the critical value, the shape of the bubbles is completely different: the bubbles are concave, there is an inflection point, and a very thin, long tail appears at the rear part of the bubble. Moreover, the velocity field around the bubbles also changes significantly for experiments below and above the critical volume. In particular, for bubbles with volumes above the critical value, the presence of the so-called negative wake can be observed.

It is possible to link this behavior with the rheological properties of the fluid. For this, the mean shear rate (defined as $\bar{\dot{\gamma}}=U/r$) at which the normal stresses are measurable and at which the discontinuity of the velocity occurs, is determined. Figure 11 shows the calculated $\bar{\dot{\gamma}}$ for the three tested liquids. From this plot, the value of the shear rate corresponding to the critical volume can be determined and is approximately the same as the shear rate at which the elastic nature of the fluid begins to manifest itself (N_1 becomes measurable). Therefore, it can be said that the bubble velocity discontinuity is a direct result of the appearance of elastic stresses.

For negligible normal stresses, the bubbles are almost spherical and their velocities are governed by the Stokes and Hadamard laws. For significant normal stresses, the velocity is larger than the velocity predicted by Stokes and Hadamard law, and the bubbles are concave, presenting a tail at their rear part.

The immediate consequence of the presence of normal stresses in the liquid is a change in the bubble shape, which evidently leads to a drag reduction and, hence, a rapid increase of velocity. A particular bubble shape is then related to its rising velocity.

We have shown before that the elasticity of the liquid plays an important role, because the discontinuity of the velocity occurs when the normal stress appears in the liquid. Consequently, we can consider that the Deborah number, defined by the ratio of the first normal stress difference N_1 and two times the tangential stress $\tau=\mu\dot{\gamma}$, can be considered to determine when the discontinuity occurs;

$$\mathrm{De}=\frac{N_1}{2\tau}=\frac{N_1 d}{4\mu U}.$$

TABLE IV. Viscosity measurements for different solutions with two methods: $\mu_{\text{rheometer}}$ is the viscosity measured in a cone-plane rheometer under simple shear. μ_{fall} is the viscosity calculated from falling-bead experiments. The ratio of the viscosity α decreases with increasing HASE concentration.

Fluid n°	% HASE	$\mu_{\text{rheometer}}$ (Pa s)	μ_{fall} (Pa s)	Viscosity ratio α
1	1.2	0.22	0.49±0.01	2.23
2	1.5	1.14	1.58±0.04	1.39
3	1.7	3.34	4.08±0.23	1.22
4 (Ref. 34)	2.1	12.5	13.23±0.4	1.06

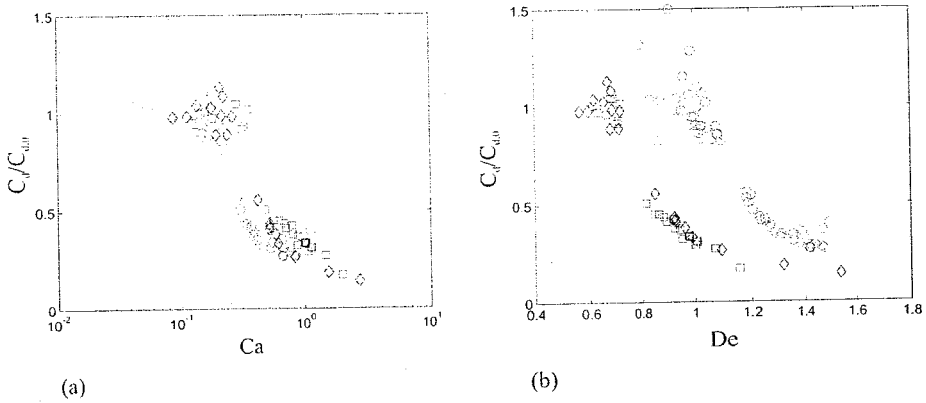

FIG. 12. (a) $C_d/C_{d,0}$ as a function of the Capillary number, (b) $C_d/C_{d,0}$ as a function of the Deborah number, for different percentages of HASE: (○) 1.2% HASE; (□) 1.5% HASE; (◇) 1.7% HASE. The critical value of these dimensionless numbers for which the discontinuity of the velocity occurs depends on the percentage of HASE.

Since there is a strong change of the shape of the bubble before and after the discontinuity, this implies that the surface tension will also play an important role. Since the discontinuity of the velocity occurs for Reynolds number smaller than 1, the capillary number, defined by the ratio of the viscous forces and the surface forces, $\mathrm{Ca}=\mu U/\sigma$ can also be considered to be an important parameter to the problem. We can define a normalized drag coefficient, which is equal to $C_d/C_{d,0}$, where $C_{d,0}$ is the Hadamard drag coefficient ($C_{d,0}=16/\mathrm{Re}$). For small bubbles (with a volume smaller than the critical one), the normalized drag coefficient will be close to 1. For large bubbles, there is an increase of the velocity. And so, for a decrease of the drag coefficient, the normalized drag coefficient will be smaller than 1. The normalized drag coefficient is shown in Fig. 12 as a function of the two dimensionless numbers previously defined. Clearly, for small De, the bubbles are spherical and $C_d/C_{d,0}$ is around 1. After a certain critical De, the normalized drag coefficient decays abruptly, corresponding to the point for which the discontinuity occurs. This behavior can be observed in the three solutions. However, the value of the critical De for which the discontinuity occurs is not unique, as it depends on the percentage of HASE. A similar trend can be observed for the capillary number: at a critical value of Ca, the normalized drag drops abruptly, but this critical value is different for each liquid. Hence, neither De nor Ca can be used to capture a generally valid condition for the jump to occur. There are two main conclusions from the results of this analysis: (1) the discontinuity appears when the elastic properties manifest themselves and (2) there is a significant change in the shape associated with the bubble velocity increase. It is then appropriate to form a dimensionless group that compares elastic forces to capillary forces,

$$\Pi = \frac{N_1 d}{\sigma}.$$

This number would be large if elastic effects dominate over surface tension effects and vice versa. In fact, this number could be interpreted as $\Pi = 4\mathrm{Ca}\times\mathrm{De}$.

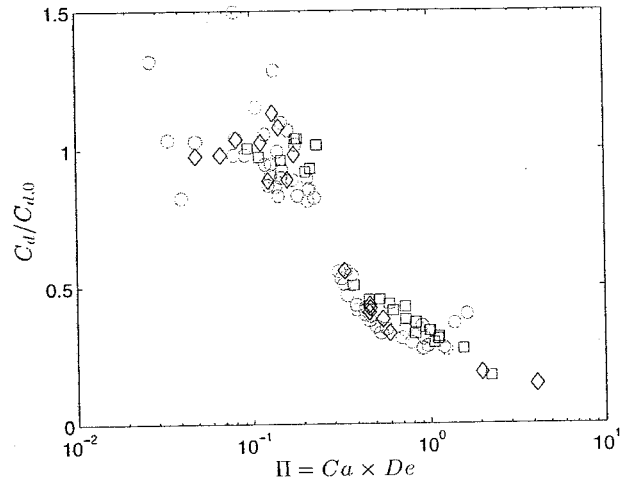

FIG. 13. Normalized drag coefficient as a function of $\Pi=\mathrm{Ca}\times\mathrm{De}$ for: (○) 1.2% HASE; (□) 1.5% HASE; (◇) 1.7% HASE. For all the percentages of HASE, the discontinuity occurs for the same value of Π ($\Pi\simeq 0.25$).

Figure 13 shows the normalized drag coefficient as a function of the dimensionless group Π. For this case, the transition from high to low drag appears to be the same for all the liquids: there is a critical value of Π ($\Pi_{\mathrm{crit}}\simeq 0.25$) that determines the conditions for the bubble velocity discontinuity to appear for all the liquids tested.

The tail at the rear part of the bubble leads to a decrease of the drag coefficient and consequently to a rapid increase of the velocity. Since the tail shape can also influence the flow behavior of the bubble, the tail shape can be related to the bubble velocity. This aspect is further discussed in the next section.

VII. SHAPES OF THE TAILS

Lastly, we present a photographic study of the peculiar shapes of the bubble tails that appear after the bubble velocity discontinuity. Previously, it was observed that a long, thin axisymmetric tail appears on the rear part of bubbles immediately after the critical volume [this case is shown in Fig. 14(a)]. The thickness of the tail can be of the order of a few microns, while its length amounts to a few centimeters. The

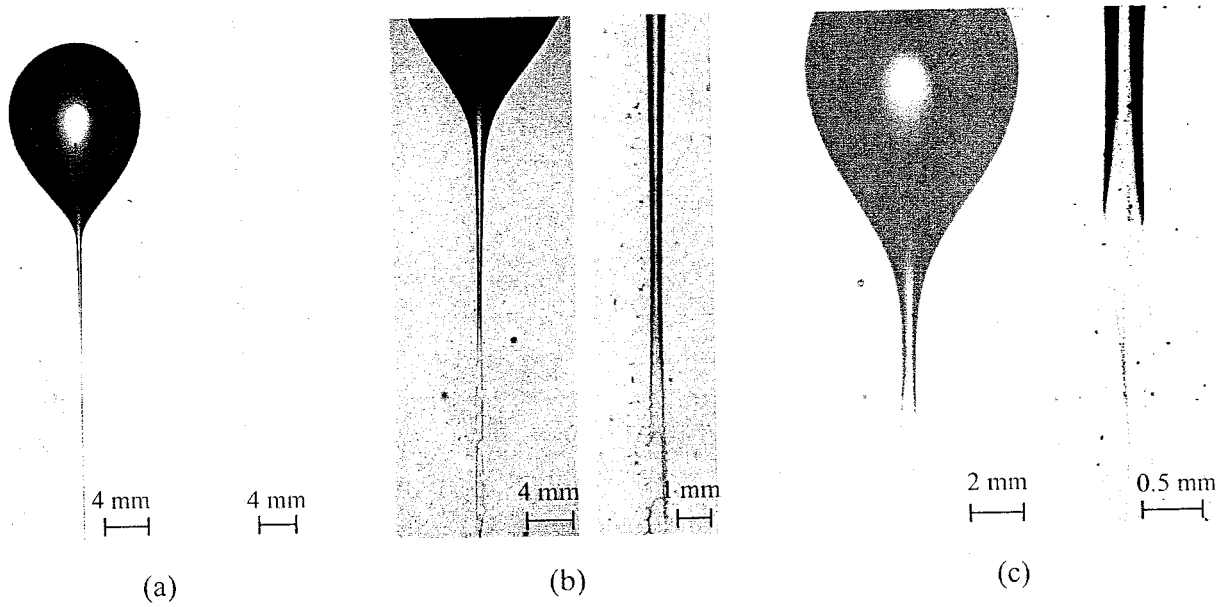

FIG. 14. Two perpendicular views (a) and (b) of the tail; the tail breaks into two different threads (V=824 mm^3, 1.5% HASE).

tail eventually breaks into micron-sized bubbles. This behavior resembles the so-called tip-streaming phenomena, when daughter drops are ejected from a thin thread at the tip of a highly stretched drop. The tip-streaming behavior was first reported by Taylor[40] and since then has been studied by many authors. To our knowledge, tip streaming has not been reported to date for the case of air bubbles moving in complex non-Newtonian liquids.

For larger bubble sizes, the cusped tip transforms into a "blade-edge" tip [two–dimensional (2D) cusp] [Figs. 14(b) and 14(c)]. The 2D cusped end was observed from simultaneous tail images taken at perpendicular views. Several experiments are necessary to obtain images in which the edge of the tail is parallel to the photo plane [images shown in Figs. 14(b) and 14(c)]. The appearance of such shapes has also been previously observed.[14] The 2D cusp does not have a preferential orientation. Note that these experiments are performed in a cylindrical tank.

Moreover, the streaming behavior can also be observed in 2D cusps; the so-called "edge streaming." We have observed that the 2D cusped tail can break into different manners for the same nominal experimental conditions. In some cases, the tail breaks into two different threads [Figs. 14(b) and 15]. The two threads extend for some distance, but eventually each one breaks into microbubbles. In some other cases, the 2D tails collapse into a single thread with perpendicular filaments that resemble a "fish backbone" [Figs. 14(c) and 16]. All these fine threads eventually break into small bubbles. Edge streaming has also not been previously reported for these fluids.

Clearly, the viscoelastic nature of the HASE solutions is responsible for the formation of the cusped and edged tips at the back of the air bubbles. However, the basic mechanism for the cusp-to-edge transition is not known. Tip streaming phenomenon is an indication that, near the cusp, high levels of fluid stretching are present. There is also a possibility that the surface active ingredients are being convected along the bubble surface, inducing surface tension gradients, hence, enhancing the tip streaming.

To further investigate the conditions for which the 2D cusps appear, additional series of experiments were performed for such large bubbles. The terminal velocities were measured for increasing bubble volumes, and the shape of the tails was also identified. Figure 17 shows the terminal velocity of bubbles as a function of volume. The symbols denote different tail shapes observed experimentally. With the present experimental setup, it is difficult to determine precisely the critical volume from which the tail changes

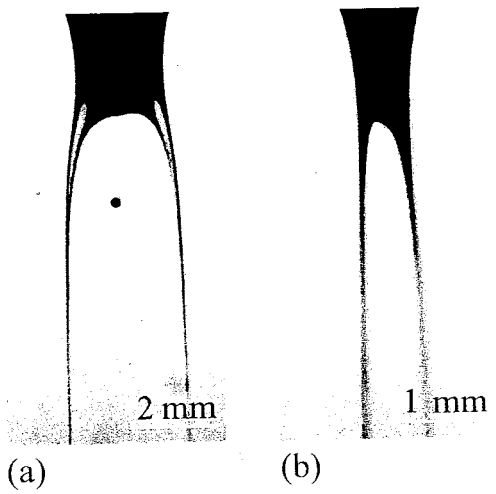

FIG. 15. Various tail shapes for bubbles moving in a 1.5% solution of HASE: (a) tip streaming: bubble with filament tail and zoom of the tail instability; (b) edge streaming: bubble with knife-edge tail and breakdown process of the tail edge; (c) edge streaming: bubble with knife-edge tail [the volume is larger than that shown in (b)] and breakdown process of the tail edge.

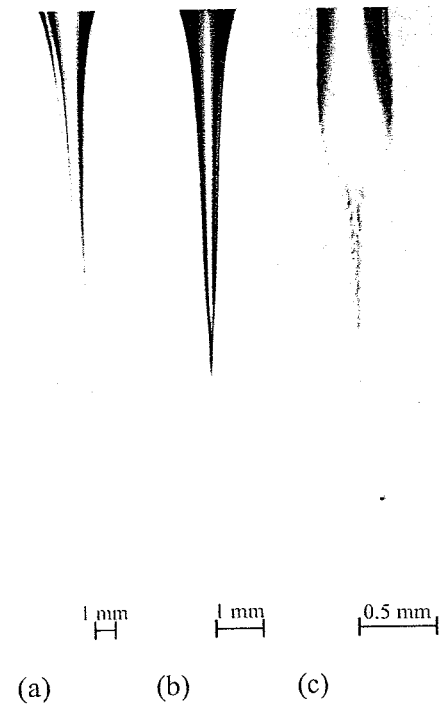

FIG. 16. Two perpendicular views (a) and (b) of the tail. (c) The tail collapses into a single thread with perpendicular filaments that resemble a "fish backbone" (V=391 mm^3, 1.5% HASE).

from axisymmetric to two dimensional (either two threaded or fish backbone).

For volumes smaller than 280 mm^3 (corresponding to shear rates smaller than 15 s^{-1}), the tail is axisymmetric, very thin, and long. For larger volumes, the 2D cusp appears. For volumes between 280 and 350 mm^3 (corresponding to shear rates between 15 and 18 s^{-1}), only fish-bone streaming is observed. For volumes larger than 350 mm^3 (corresponding to shear rates larger than 18 s^{-1}) both two-thread and fish-bone formations can be observed. Although the influence of the type of 2D tail on the terminal velocity of the bubble (drag coefficient) is not significant, we observed that when the two types of edge-streaming appear, a larger scatter of data of bubble velocity is observed.

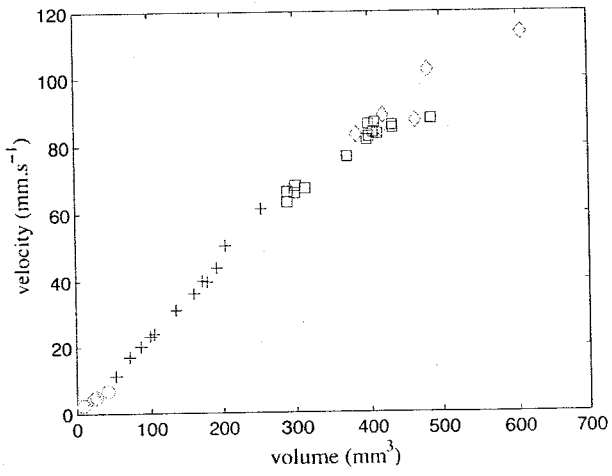

FIG. 17. Velocity as a function of the bubble volume for 1.5% HASE. Different critical values of the volume for the different bubble shapes: (○) spheroidal bubbles; (+) axisymmetric tail (tip streaming); (□) 2D edged tail (fish-bone streaming); (◇) 2D edged tail (two-thread streaming).

The different shapes of tails reported in this section have never been observed for rising bubbles in either polymeric or worm-like micellar fluids. The formation of these different shapes may be, in fact, a result of the specific properties of the associative polymer fluid. Clearly, further experiments are needed to understand the formation process of a particular tail shape.

VIII. SUMMARY AND CONCLUSIONS

We have shown that for bubbles rising in an associative polymer solution, as the bubble volume increases, a discontinuity of the velocity occurs. This discontinuity in the velocity is smaller than that observed for aqueous shear-thinning viscoelastic liquids. A more distinctive feature for this case is that the slope of the relation velocity-volume increases significantly past the discontinuity. This particular behavior was studied for various HASE concentrations. It was possible to relate this discontinuity with the rheological properties of the fluid. In fact, the shear rates for which the discontinuity occurs correspond to those for which the normal stresses appear. It is important to note that the critical shear rates also correspond to the point at which the shear thickening appears in some solutions, which may contribute to reducing the strength of the velocity jump.

The discontinuity can also be related to the bubble shape and to the flow around the bubble. For volumes smaller than the critical volume, the bubbles are spherical or spheroidal and the flow around the bubble is similar to that of a Newtonian liquid. For volumes larger than the critical one, the rear of the bubble is concave and presents a tail at their rear part. The flow around the bubble is more complex, and the presence of a negative wake can be observed.

This study provides a criterion for the determination of a critical volume. Due to the importance of the elasticity and the surface tension, a dimensionless number defined as $\Pi = N_1 d/\sigma$ is proposed to determine the jump conditions. The discontinuity occurs for $\Pi_{crit} \simeq 0.25$.

For the case of small bubbles, we found good agreement between experiments and predictions for the velocities according Stokes-Hadamard laws. For small bubbles, the shear rate is small, and consequently, the liquid can be considered as Newtonian. For this agreement, the viscosity had to be obtained with a falling-bead technique. In agreement with previous investigations, we found that the viscosity determined in this manner was larger than that obtained under simple-shear viscometric flow.

For large bubble volumes, we presented a photographic study of the bubble shapes and particularly the tail shapes. Different kinds of tails can be observed.

From the present results, we have determined that the appearance of the discontinuity results from a balance between elastic and surface tension forces. We are currently conducting additional experiments with other non-

Newtonian liquids (Boger, inelastic, etc.) to further corroborate the appropriateness of the Π group to describe the conditions of the bubble velocity discontinuity. These results will be reported in a future communication.

ACKNOWLEDGMENTS

C.G. acknowledges the support of UNAM's postdoctoral program. E.S. appreciates the financial support from Conacyt and DGEP. The authors would like to thank QFB Araceli Ordónez Medrano for the surface tension characterization and Thibault Behaghel for his help during the first stage of experimental work.

[1]R. Clift, J. R. Grace, and M. E. Weber, *Bubbles, Drops and Particles* (Academic, New York, 1978).
[2]R. P. Chhabra, *Bubbles, Drops and Particles in Non-Newtonian Fluids* (CRC, Boca Raton, FL, 1993).
[3]D. Funfschilling and H. Z. Li, "Flow of non-Newtonian fluids around bubbles: PIV measurements and birefringence visualisation," Chem. Eng. Sci. **56**, 137 (2001).
[4]G. Astarita and G. Apuzzo, "Motion of gas bubbles in non-Newtonian liquids," AIChE J. **11**, 815 (1965).
[5]S. M. Barnett, A. E. Humphrey, and M. Litt, "Bubble motion and mass transfer in non-Newtonian fluid," AIChE J. **12**, 253 (1966).
[6]P. H. Calderbank, D. S. Johnson, and J. Loudon, "Velocity fields around spheres and bubbles investigated by laser-Doppler anemometry," Chem. Eng. Sci. **25**, 235 (1970).
[7]L. G. Leal, J. Skoog, and A. Acrivos, "On the motion of gas bubbles in a viscoelastic fluid," Can. J. Chem. Eng. **49**, 569 (1971).
[8]D. Rodrigue, D. De Kee, and C. F. Chan Man Fong, "Bubble velocities: further developments on the jump discontinuity," J. Non-Newtonian Fluid Mech. **79**, 45 (1998).
[9]D. Rodrigue, D. De Kee, and C. F. Chan Man Fong, "An experimental study of the effect of surfactants on the free rise velocity of gas bubbles," J. Non-Newtonian Fluid Mech. **66**, 213 (1996).
[10]J. R. Herrera-Velarde, R. Zenit, D. Chehata, and B. Mena, "The flow of non-Newtonian fluids around bubbles and its connection to the jump discontinuity," J. Non-Newtonian Fluid Mech. **111**, 199 (2003).
[11]O. Hassagar, "Negative wake behind bubbles in non-Newtonian liquids," Nature **279**, 402 (1979).
[12]M. T. Arigo and G. H. McKinley, "An experimental investigation of negative wakes behind spheres settling in a shear-thinning viscoelastic fluid," Rheol. Acta **37**, 307 (1998).
[13]E. Zana and L. G. Leal, "The dynamics and dissolution of gas bubbles in a viscoelastic fluid," Int. J. Multiphase Flow **4**, 237 (1978).
[14]Y. J. Liu, T. Y. Liao, and D. D. Joseph, "A two-dimensional cusp at the trailing edge of an air bubble rising in a viscoelastic liquid," J. Fluid Mech. **304**, 321 (1995).
[15]M. A. Winnik and A. Yekta, "Associative polymers in aqueous solution," Curr. Opin. Colloid Interface Sci. **2**, 424 (1997).
[16]K. C. Tam, L. Guo, R. D. Jenkins, and D. R. Bassett, "Viscoelastic properties of hydrophobically modified alkali-soluble emulsion in salt solutions," Polymer **40**, 6369 (1999).
[17]O. Manero, F. Bautista, J. F. A. Soltero, and J. E. Puig, "Dynamics of worm-like micelles: the Cox-Merz rule," J. Non-Newtonian Fluid Mech. **106**, 1 (2002).
[18]F. Bautista, J. M. de Santos, J. E. Puig, and O. Manero, "Understanding thixotropic and antithixotropic behaviour of viscoelastic micellar solutions and liquid crystalline dispersions. I. The model," J. Non-Newtonian Fluid Mech. **80**, 93 (1999).
[19]A. Belmonte, "Self oscillations of a cusped bubble rising through a micellar solution," Rheol. Acta **39**, 554 (2000).
[20]S. Chen and J. P. Rothstein, "Flow of a wormlike micelle solution past a falling sphere," J. Non-Newtonian Fluid Mech. **116**, 205 (2004).
[21]A. Jayaraman and A. Belmonte, "Oscillations of a solid sphere falling through a wormlike micellar fluid," Phys. Rev. E **67**, 065301(R) (2003).
[22]A. M. Mollinger, E. C. Cornelissen, and B. H. A. A. van den Brule, "An unexpected phenomenon observed in particle settling: oscillating falling spheres," J. Non-Newtonian Fluid Mech. **86**, 389 (1999).
[23]P. H. T. Uhlherr, T. N. Le, and C. Tiu, "Characterisation of inelastic power-law fluids using falling sphere data," Can. J. Chem. Eng. **54**, 497 (1976).
[24]D. Rodrigue (private communication).
[25]Y. Caram, F. Bautista, J. E. Puig, and O. Manero, "On the rheological modeling of associative polymer," Rheol. Acta (to be published).
[26]D. Hammerton and F. H. Garner, "Gas absorption from single bubbles," Trans. Inst. Chem. Eng. **32**, S18 (1954).
[27]V. G. Levich, *Physico-Chemical Hydrodynamics* (Prentice-Hall, Englewood Cliffs, NJ, 1962).
[28]G. G. Stokes, *Mathematical and Physical Papers* (Cambridge University Press, England, 1880).
[29]H. Schlichting, *Boundary Layer Theory* (McGraw-Hill, New York, 1964).
[30]J. Hadamard, "Mouvement permanent lent d'une sphere liquide et visqueuse dans un liquide visqueux," C. R. Acad. Sci. Paris **152**, 1735 (1911).
[31]W. Rybczynski, "Uber die Fortschreitende Bwegung einer-ussigen Kugel in einem zahen Medium," Bull. Acad. Sci. Cracovie Ser. A **1**, 40 (1911).
[32]C. Bisgaard and O. Hassager, "An experimental investigation of velocity fields around spheres and bubbles moving in non-Newtonian liquids," Rheol. Acta **21**, 537 (1982).
[33]H. Z. Li, X. Frank, D. Funfschilling, and Y. Mouline, "Towards the understanding of bubble interactions and coalescence in non-Newtonian fluids: a cognitive approach," Chem. Eng. Sci. **56**, 6419 (2001).
[34]A. Mendoza Fuentes, "Diseño, construccion y aplicacion de un equipo de asentamiento de particulas en un polimero asociativo," Master thesis, Universidad Nacional Autonoma de Mexico, 2006.
[35]J. Happel and H. Brenner, *Low Reynolds Number Hydrodynamics* (Prentice-Hall, Englewood Cliffs, NJ, 1973).
[36]G. H. McKinley, *Transport Processes in Bubbles, Drops and Particles*, edited by R. Chhabra and D. DeKee (Taylor and Francis, New York, 2002), Chap. 14.
[37]R. P. Chhabra, C. Tiu, and P. H. T. Uhlherr, "A study of wall effects on the motion of a sphere in viscoelastic fluids," Can. J. Chem. Eng. **59**, 771 (1981).
[38]R. P. Chhabra and P. H. T. Uhlherr, "The influence of fluid elasticity on wall effects for creeping sphere motion in cylindrical tubes," Can. J. Chem. Eng. **66**, 154 (1988).
[39]E. S. Boek, J. T. Padding, V. J. Anderson, P. M. J. Tardy, J. P. Crawshaw, and J. R. A. Pearson, "Constitutive equations for extensional flow of wormlike micelles: Stability analysis of the Bautista-Manero model," J. Non-Newtonian Fluid Mech. **126**, 39 (2005).
[40]T. D. Taylor and A. Acrivos, "On the deformation and drag of a falling viscous drop at low Reynolds number," J. Fluid Mech. **18**, 466 (1964).

BULLETIN
OF THE AMERICAN PHYSICAL SOCIETY

PROGRAM OF THE 60th ANNUAL MEETING OF THE DIVISION OF FLUID DYNAMICS

November 18–November 20, 2007
Salt Lake City, Utah

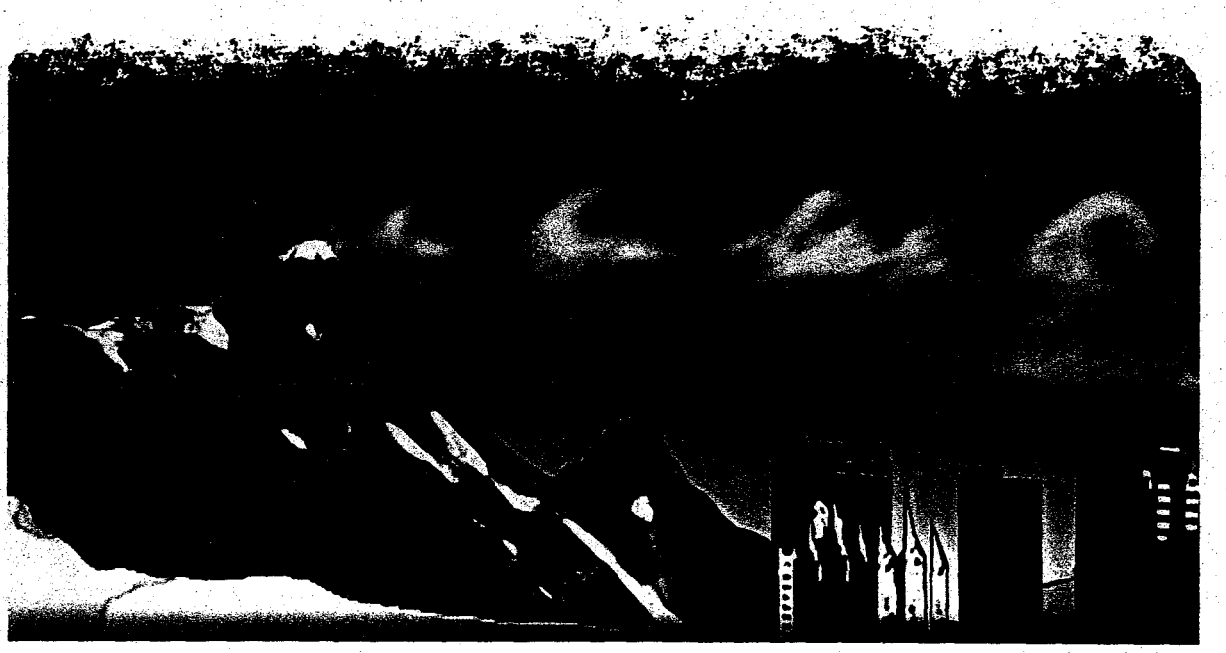

THE UNIVERSITY OF UTAH
Utah State University
University of Idaho
BYU BRIGHAM YOUNG UNIVERSITY

November 2007
Volume 52, No. 17

APS physics

31. *A Numerical Investigation of Polygonal Converging Shock Waves*

Veronica Eliasson, University of California, Berkeley and KTH Mechanics, Sweden; William D. Henshaw and Daniel Appel, Lawrence Livermore National Laboratory.

32. *Water Bells Formed on the Underside of a Horizontal Plate*

Eleanor C. Button and John E. Sader, University of Melbourne, Australia; Ben Dwyer, Claire Jenkins and Graeme Jameson, University of Newcastle, Australia.

33. *Bubble Dynamics in a Microfluidic Channel*

Pedro A. Quinto-Su and Vasan Venugopalan, University of California, Irvine.

34. *Spatio-Temporal Evolution of Segregation Patterns*

Estelle Guyez and J. Thomas, University of Warwick, UK.

35. *Wake Structure of Single Rising Clean Bubble*

Ayaka Sato, Yuta Takedomi and Masao Watanabe, Kyushu University, Japan; Minori Shirota, National Institute of Advanced Industrial Science and Technology, Japan; Toshiyuki Sanada, Shizuoka University, Japan.

36. *A Ratcheting Mechanism via Shape Change in an Oscillating Fluid*

Saverio Spagnolie and Mike Shelley, New York University.

37. *Anatomy of the Flow Past a Cube by 3D Full-Field Flow Measurement*

Gang Pan, TSI Inc.

38. *The Diffusion Fish*

Thomas Peacock and Roman Stocker, Massachusetts Institute of Technology; Eric Lauga, UCSD; Will Etheridge, Massachusetts Institute of Technology.

39. *Fractal Kelvin-Helmholtz Break-Ups*

J. Fontane and L. Joly, Ensica, France; J.N. Reinaud, University of St-Andrews, UK.

40. *Rosensweig Instability of a Ferrofluid Droplet*

Ching-Yao Chen, National Chiao Tung University, Taiwan; Z.-Y. Cheng, National Yunlin University of Science & Technology, Taiwan.

41. *Interfacial Instability of a Miscible Ferrodroplet Immersed in a Thin Fluid Layer*

Ching-Yao Chen, National Chiao Tung University, Taiwan; W.-K. Tsai, National Yunlin University of Science and Technology, Taiwan.

42. *Evolution of Coherent Structures in Low Reynolds Number Flows over an Airfoil*

Serhiy Yarusevych, University of Waterloo; Greg Kawall, Ryerson University; Pierre Sullivan, University of Toronto.

GALLERY OF FLUID MOTION VIDEOS

1. *Fruit Flies in Free Flight*

Leif Ristroph and Itai Cohen, Cornell University.

2. *DPIV of Mammalian Swimming*

Paul Legac and Timothy Wei, Rensselaer Polytechnic Institute; Frank Fish, West Chester University; Terrie Williams, University of Santa Cruz; Russell Mark and Sean Hutchison, USA Swimming/ King Aquatics Club.

3. *High Speed Visualization of Vortex Breakdown*

Goossens Thomas, Jori E. Ruppert-Felsot and Philippe Petitjeans, ESPCI, France.

4. *Particle Resuspension due to Foot Motion*

Yoshihiro Kubota and Hiroshi Higuchi, Syracuse University.

5. *High-Speed X-Rays Vision of Isopropanol Droplet Impact on Isopropanol Surface*

Kamel Fezzaa and Yujie Wang, Argonne National Laboratory.

6. *Vortex Patterns in a T-Channel*

Susan Thomas and Timothy Ameel, University of Utah

7. *A Fuel Jet as seen with X-Rays and 150 Picosecond Time Resolution*

Kamel Fezzaa, Yujie Wang, KyoungSu Im, Wah-Keat Lee and Jin Wang, Argonne National Laboratory.

8. *Rapid Growth Events of Enstrophy in 3D Turbulence*

Joerg Schumacher, Technical University Ilmenau, Germany; Herwig Zilken, Maik Boltes and Marc-Andre Hermanns, Research Centre Juelich, Germany; Bruno Eckhardt, Philipps University Marburg, Germany.

9. *Spouts and Stars: Instabilities in Oscillating Magnetic Fluids*

Wayne Smith and Matthew Staymates, National Institute of Standards and Technology.

10. *Rupture of Viscoelastic Liquids at Extremely High Strain Rates*

Vladimir V. Mitkin, Chee-Loon Ng and Theo G. Theofanous, University of California Santa Barbara.

11. *A New Window to Aero-Breakup made possible by LIF and 15 ns exposure*

Chee-Loon Ng, Vladimir V. Mitkin and Theo G. Theofanous, University of California Santa Barbara.

12. *The Lagrangian Skeleton of Turbulence*

Manikandan Mathur, George Haller, and Thomas Peacock, Massachusetts Institute of Technology; Jori E. Ruppert-Felsot, LMD-CNRS, Ecole Normale Superieure, France; Harry L. Swinney, University of Texas at Austin.

13. *Inflatable Wing Aerodynamics*

Jamey Jacob, Oklahoma State University; Suzanne Smith, University of Kentucky; Dave Cadogan and Steve Scarborough, ILC Dover.

14. *Simulation of Deformable Particle Suspensions using a Coupled Lattice-Boltzmann/Finite-Element Method*

Jonathan Clausen, Robert MacMeccan, Paul Neitzel and Cyrus Aidun, Georgia Institute of Technology.

15. *Thinking Bubbles*

Manu Prakash and Neil Gershenfeld, Massachusetts Institute of Technology.

16. *Glass Bead Impact on Isopropanol: a High-Speed X-Ray Vision*

Kamel Fezzaa and Yujie Wang, Argonne National Laboratory.

17. *X-Ray Vision of Water Droplet Impact on Water*

Kamel Fezzaa and Yujie Wang, Argonne National Laboratory.

18. *Flow Patterns of Thin Water Films on Inclined Structured Plates Visualized by Infrared Thermography*

Karsten Luffler, Tatiana Gambaryan-Roisman and Peter Stephan, TU Darmstadt, Germany.

19. *Break Up of the Tail of a Bubble in a Non-Newtonian Fluid*

Enrique Soto, Roberto Zenit and Octavio Manero, Universidad Nacional Autonoma de Mexico.

20. *Motion of Floating Droplet under Laser Heating*

Chaeyeon Song, Jong Kyun Moon, Kyuyong Lee and Hyuk Kyu Pak, Pusan National University, Korea.

21. *"Black Hole" Nucleation in a Splash of Milk*

Laurent Courbin and James C. Bird, Harvard University; Andrew Belmonte, Penn State University; Howard A. Stone, Harvard University.

22. *Oscillating Band-Patterns of Suspended Polystyrene Balls in a Water-Filled Rotating Horizontal Cylinder*

Gabriel Seiden, Max Planck Institute for Dynamics and Self-Organization, Goettingen, Germany; Marius Ungarish and Stephen G. Lipson, Technion-Israel Institute of Technology.

23. *Spilling Breakers and Surfactants*

Xinan Liu, James Diorio and James H. Duncan, University of Maryland.

24. *Rayleigh-Benard Convection with Imposed Heat Flux*

Hans Johnston, University of Massachusetts; Charles R. Doering, University of Michigan.

25. *Curiously Shaped Instabilities at the Fronts of Volatile Drops*

N. Murisic and L. Kondic, New Jersey Institute of Technology; Y. Gotkis, KLA-Tencor.

26. *Dispersed-Phase Motion in MHD Turbulence at Low Magnetic Reynolds Number*

Jehud Flores and Damian Rouson, U.S. Naval Research Laboratory; Stavros Kassinos, University of Cyprus.

27. *Virtual Rheoscopic Fluids*

Florian Hecht, Georgia Institute of Technology; Peter J. Mucha, University of North Carolina at Chapel Hill; Greg Turk, Georgia Institute of Technology.

28. *Laser-Induced Vapor Bubble in a Liquid Jet*

Etienne Robert and Peter A. Monkewitz, Swiss Federal Institute of Technology Lausanne (EPFL).

BULLETIN

OF THE AMERICAN PHYSICAL SOCIETY

APS dfd 59 2006
Division of Fluid Dynamics

UF UNIVERSITY of FLORIDA

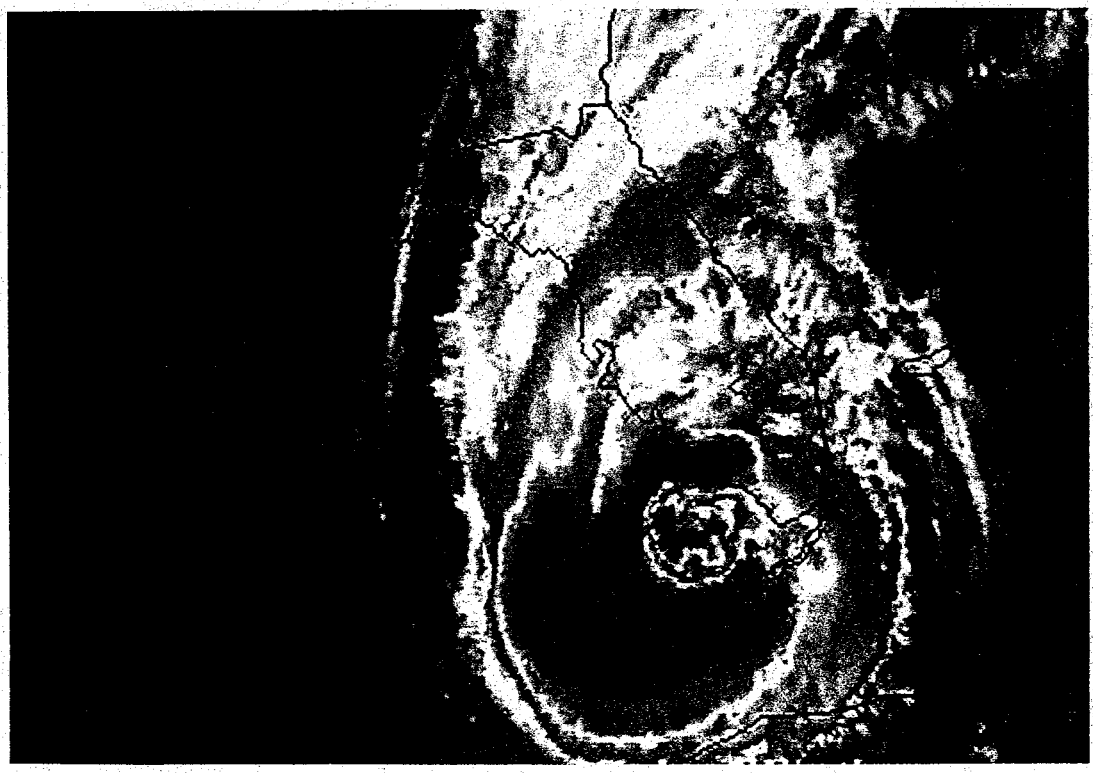

Tampa Bay, Florida

November 2006

Volume 51, No. 9

APS physics

SESSION KK: NON-NEWTONIAN FLOWS II
Monday evening, 20 November 2006
Meeting Room 4, Tampa Marriott Waterside Hotel and Marina at 17:15
Andrew Belmonte, Penn State University, presiding

17:15
KK 1 Dynamical slowdown of polymers in laminar and random flow DARIO VINCENZI, EBERHARD BODENSCHATZ, *Max Planck Institute for Dynamics and Selforganization, Goettingen, Germany* ALBERTO PULIAFITO, ANTONIO CELANI, *INLN, Nice, France* The dynamics of an isolated polymer in a flow field forms the basis of constitutive models for dilute polymer solutions. We investigate the influence of an external flow on the relaxation dynamics of a single polymer theoretically and numerically. We show that a pronounced dynamical slowdown occurs in the vicinity of the coil–stretch transition, especially when the dependence on polymer conformation of the drag is accounted for. For the elongational flow, relaxation times are exceedingly larger than the Zimm relaxation time, resulting in the observation of conformation hysteresis. For random smooth flows hysteresis is not present. Yet, relaxation dynamics is significantly slowed down because of the large variety of accessible polymer configurations. In both cases, the dependence of the drag force on the polymer configuration plays a prominent role. This suggests the necessity of improving current models of polymer solutions in turbulent flows to account for such effect.

17:28
KK 2 Transport properties of a flexible fiber in cellular flows MICHAEL SHELLEY, *Courant Institute, New York University* YUAN-NAN YOUNG, *Department of Mathematical Sciences, New Jersey Institute of Technology* Recent experiments by V. Steinberg and his collaborators have used "low Reynolds turbulence" in elastic flows to demonstrate coil-stretch transitions of fluorescently labelled DNA molecules. With this as motivation, we consider the much simpler problem of an elastic fiber that moves in a periodic cellular flow. Our numerical simulations show that such a fiber can act as a spatially extended test particle whose internal dynamics can lead to complex transport properties across space. In some parameter regimes, we find that space can be divided into regions of fiber entrapment and fiber transport, with fibers either trapped near elliptic points, or being transported along the connecting manifolds of the hyperbolic points. We also find that fiber buckling near hyperbolic points can yield random walk behavior over long times, with the effective diffusivity showing little dependence on the effective rigidity of the fiber.

17:41
KK 3 Microfluidic bubble trains in non-Newtonian fluids MATTHEW SULLIVAN, *Division of Engineering and Applied Sciences, Harvard University / Schlumberger-Doll Research* KARINA MOORE, *Norfolk State University* HOWARD STONE, *Division of Engineering and Applied Sciences, Harvard University* We present studies of bubble formation and propagation in non-Newtonian fluids using a microfluidic flow-focusing device. Under certain conditions, monodisperse bubble trains can be formed. The bubble size and shape at formation are measured as a function of fluid flow rate and gas pressure and compared to bubble generation in a Newtonian fluid. We also observe two instabilities in non-Newtonian bubble propagationdrifting toward the channel wall and drifting towards neighboring bubbles in the bubble train even at large initial bubble separations. This behavior is in contrast to a Newtonian fluid where bubbles occupy a stable position along the channel centerline and maintain their initial separation.

17:54
KK 4 Computation of the Knife-Edge Cusp of a Rising Bubble in a Viscoelastic Fluid* RUOBO YOU, HOSSEIN HAJ-HARIRI, *University of Virginia* We consider the buoyant rise of an originally-spherical bubble through a viscoelastic fluid. Experiments have demonstrated that the sharp trailing edge could develop a three dimensional cusp of "knife-like" shape under certain conditions (high capillary number, large drop size). In order to understand the complex physics of this phenomenon, we have conducted a linear, three-dimensional temporal stability analysis of a computationally-obtained axisymmetric cusped bubble. The in-house time-accurate code is control-volume based and uses a body-fitted grid. Flux-difference splitting is employed to handle large Deborah numbers. Artificial compressibility is used for time marching. The resulting eigenanalysis shows the only linearly-unstable mode to be the one with azimuthal wavenumber of 2. The eigenvalue is real and the nature of instability is an exchange of stability. Thus an axisymmetric cusp can indeed develop into a knife-like shape. An investigation of the energy production and dissipation for the disturbances shows that the normal pressure gradient of the base-state along the free surface plays an important role in the evolution of the instability.

*supported by NASA Grant NAG3-2760; R. Balasubramaniam.

18:07
KK 5 Influence of shape and boundary condition on the drag on bubbles moving in non Newtonian liquids E. SOTO, C. GOUJON, R. ZENIT, *Inst. Inv. Materiales, Universidad Nacional Autonoma de Mexico* Bubbles moving in non Newtonian fluid exhibit a peculiar behavior: the terminal velocity increases abruptly for a critical value of the volume. There has been a long debate on the nature of this phenomenon, one of which assumes that the boundary condition on the surface of the bubble changes from non-slip to slip. To investigate this claim we have performed an axi-symmetric 2D simulation to determine the drag on a bubble moving in a container. The parameters used are those corresponding to bubbles in which the bubble velocity discontinuity appears. From experiments, the exact shape of bubbles is obtained by a digital analysis. The profile is then feed into a fixed shape Navier-Stokes solver. The viscosity and rise velocity are also taken from the experiments. Then the boundary condition on the surface is chosen to either be slip or non-slip. The drag coefficient can be calculated for each case. We tested cases corresponding to bubbles in non-Newtonian liquids right before and after the velocity discontinuity. Bubbles below this critical volume are spheroidal considering a rigid interface. Bubbles above this value have a tear like

shape, with or without a tail, and a free interface. Our results show that the drag reduction associated with the bubble velocity discontinuity is not as large as that observed experimentally. Hence, the change of shape and boundary conditions cannot fully explain the nature of this phenomenon.

18:20

KK 6 Thinning of Lamella in a Non-Newtonian Foam LUCIEN BRUSH, *University of Washington* STEVEN ROPER, *Northwestern University* Consider a surfactant-free lamella in an evolving foam. Asymptotic analysis in small capillary number is used to assess the effects of non-Newtonian properties of the liquid using power-law and Ellis models of viscosity, principally present in the transition region. For a foam in which the Plateau border radius of curvature and the lamellar length are of the same order of magnitude, the shear rate dependence of the viscosity changes the time scale for thinning but not the power law behavior of the thinning rate compared to Newtonian fluids. For a foam in which the area of fluid in the Plateau border and in the lamellar region are of the same order initially the effects of the non-Newtonian viscosity appear explicitly in the integrated form of the lamellar thinning law. Comparisons are made between a number of shear-thinning fluids, a shear-thickening fluid and a Newtonian fluid.

18:33

KK 7 Modelling persistent holes in complex fluids ROBERT D. DEEGAN, RICHARD R. KERSWELL, *University of Bristol* Mekr *et al.* (PRL 184501 **98**, (2004)) discovered that vertically vibrated shear thickening fluids can support stable vertical interfaces. These stable structures take the form of holes, voids that span the fluid layer which can last indefinitely, or of fingers, columnar-type protrusions which persist for thousands of cycles. We show that the stability of the holes can be understood in terms of a hysteretic rheology model, and confirm the existence of this hysteresis in rheological measurements of a mixture of cornstarch and water.

18:46

KK 8 Viscoelastic bells LUC LEBON, JEAN-SEBASTIEN ROCHE, LAURENT LIMAT, *PMMH - ESPCI/CNRS* ANDREW BELMONTE, *Penn State University* We performed experiments on liquid bells resulting from the impact of a viscoelastic fluid on a circular obstacle larger than the jet diameter, in the way of water bells by Savart[1]. We used polymer solutions or giant-micelle solutions as viscoelastic fluid. In the regime of closed bell, we observed a particular shape of bells, very different from the shape of water bells as observed and predicted by Clanet[2]. The bells shape is essentially controled here by the viscoelastic rheology. It appears also very sensitive to the pressure gap through the liquid film. For higher flow rate, the bells do not close anymore and form liquid sheets. Their desintegration is very different from the one observed for Newtonian liquid : filaments structure extends the sheet without any drops formation. An original behaviour of growth of circular holes with a thick rim is also observed.

[1]F. Savart, *Ann. Chim.* **54** (1833)
[2]C. Clanet, *J. Fluid Mech.* **430** (2001)

SESSION KL: TURBULENT BOUNDARY LAYERS IV

Monday evening, 20 November 2006
Meeting Room 8, Tampa Marriott Waterside Hotel and Marina at 17:15
Ellen Longmire, University of Minnesota, presiding

17:15

KL 1 Zero Pressure Gradient Flat Plate Boundary Layer Experiments Using Synchronized PIV and a Hot Wire Anemometry Rake* M. TUTKUN, P.B.V. JOHANSSON, W.K. GEORGE, *Chalmers University of Technology, Dept. of Applied Mechanics, 412 96 Goteborg Sweden* M. STANISLAS, J.M. FOUCAUT, J. KOSTAS, S. COUDERT, *Laboratoire de Mecanique de Lille, UMR CNRS 8107, 59655 Villeneuve d'Ascq France* J. DELVILLE, *Laboratoire d'Etudes Aerodynamiques, UMR CNRS 6609, 86036 Poitiers France* Zero pressure gradient flat plate boundary layer experiments have been performed in the 20 meter long test section of the Laboratoire de Mécanique de Lille, LML, wind tunnel. Measurements were carried out at Re_θ = 10 000 and Re_θ = 20 000 using synchronized PIV and a hot wire anemometry rake. The boundary layer thickness at the measurement location was about 30 cm. A hot wire rake of 143 probes was placed in the test section of the wind tunnel to provide the time history of the boundary layer. 2 stereo PIV systems in the wallnormal-spanwise (YZ) plane, and 1 stereo PIV system to record in the streamwise-wallnormal (XY) were used. One high repetition PIV system was used in streamwise-spanwise (XZ) plane. The sampling frequency of the XZ PIV system was 3000 VF/s at Re_θ = 20 000 and 1500 VF/s at Re_θ = 10 000.

*This work has been performed under the WALLTURB project. WALLTURB (A European synergy for the assessment of wall turbulence) is funded by the CEC under the 6th framework program (CONTRACT N: AST4-CT-2005-516008)

17:28

KL 2 Adverse Pressure Gradient Boundary Layer Experiments Using Synchronized PIV and a Hot Wire Anemometry Rake* P.B.V. JOHANSSON, M. TUTKUN, W.K. GEORGE, *Chalmers University of Technology, Dept. of Applied Mechanics, 412 96 Goteborg Sweden* M. STANISLAS, J.M. FOUCAUT, J. KOSTAS, S. COUDERT, *Laboratoire de Mecanique de Lille, UMR CNRS 8107, 59655 Villeneuve d'Ascq France* J. DELVILLE, *Laboratoire d'Etudes Aerodynamiques, UMR CNRS 6609, 86036 Poitiers France* This is the first report of an adverse pressure gradient turbulent boundary layer experiment performed in Laboratoire de Mécanique de Lille, LML, wind tunnel which is of 20 meter in length. The adverse pressure gradient was created by means of a bump of 30 cm height. The thickness of the boundary layer was about 30 cm and Reynolds number based on momentum thickness, Re_θ, was 30 000 for 10 m/s external free stream velocity. A hot wire rake of 143 probes synchronized and simultaneously sampled together with 2 stereo PIV systems in the wallnormal-spanwise (YZ) plane, 1 cm upstream of the wires

BULLETIN

OF THE AMERICAN PHYSICAL SOCIETY

PROGRAM OF THE 58th ANNUAL MEETING OF THE DIVISION OF FLUID DYNAMICS

November 20–22, 2005
Chicago, Illinois

World Year of PHYSICS 2005
www.physics2005.org

November 2005

Volume 50, No. 9

APS

for presenting data produced by experiment and simulation. In this talk we discuss the key changes in the force network for a granular material in an inclined bed. We use particle dynamics to model the granular material as a two-dimensional system of polydisperse disks, and study the evolution of forces, contact angles and network topology as the system approaches the onset of flow. By applying novel network analysis techniques, we gain insight into how granular materials organize, restructure, and ultimately fail under shear.

13:59

HJ 4 Twisted Sandpiles: A Structural Signature of Jamming in Granular Materials ERIC CORWIN, HEINRICH JAEGER, SIDNEY NAGEL, *The James Franck Institute and Department of Physics,The University of Chicago* When the temperature is increased, a glass loses its rigidity and begins to flow. If sufficient shear stress is applied to a granular material, it too will lose its rigidity and flow. There is no ambiguity between the rigid and flowing phases in both cases. However glasses and liquids have nearly identical structure. Are jammed states and flowing states in a granular system structurally different? And if so is there a measurement which would yield a signature of this difference? We have created an experimental technique that measures the contact-force distribution during shearing flow to address these questions. The distribution of forces is sensitive to minute variations in particle to particle distances. As such, it provides a microscopic view of the nearest-neighbor position correlations. At the onset of jamming we find a qualitative change in the force distribution. This, in turn, hints that there may be a similar structural signature in glasses. Further, we also measure a new granular temperature in granular systems which may be analogous to the glass-transition temperature in liquids.

14:12

HJ 5 Cage Dynamics in a Uniformly Heated Granular Fluid PEDRO REIS, ROHIT INGALE, MARK SHATTUCK, *Levich Institute, City College of New York* We report a novel experimental investigation of the dynamics of a uniformly heated, horizontal and quasi-2D granular fluid. Our study is done as a function of filling fraction, ϕ, in the region prior to crystallization which we observe at $\phi_s = 0.719 \pm 0.007$. We perform a statistical analysis based on two quantities that are typically employed in colloidal/molecular systems: the Mean Square Displacement (MSD) and the Self Intermediate Scattering Function (SISF). These are calculated from the trajectories obtained by tracking all particles inside a representative imaging window of the full system. At low ϕ the classic diffusive behavior of a disordered fluid is observed. As the filling fraction is increased towards ϕ_s, the MSD (or SISF) develops a two-step increase (or decrease) analogous to what is commonly observed in glassy systems. This plateau at intermediate timescales is a signature of the slowing down of the motion of particles due to temporary trapping inside the cages formed by their neighbors. This caging is increasingly more pronounced as ϕ_s is approached from below. For $\phi > \phi_s$, each particle becomes fully arrested by its six neighbors, for the whole time accessible experimentally. Moreover, the relaxation time extracted from the SISF, as a function of ϕ, is well described by the Vogel-Fulchers law. Our results are an important step in strengthening the analogy between colloidal/molecular glassy systems and dense granular materials under uniform thermalization.

SESSION HK: NON NEWTONIAN FLOWS I

Monday Afternoon, 21 November 2005

Joliet, Hilton Chicago at 13:20

Roberto Zenit, Universidad Nacional Autonoma de Mexico, presiding

13:20

HK 1 A continuum model with microstructural evolution for Stokesian suspensions, viscoplastic dispersions and granular media JOE GODDARD, *University of California, San Diego* A special case of the "thixotropic" fluid proposed several years ago by this author (*J. NonNewtonian Fluid Mech.* 14 141-160,1984) is explored as a plausible model for the flow of homogeneous particle suspensions and dense granular media. The effect of deformation history is described by the shear-induced evolution of a second-rank "fabric" tensor, which serves to define a pair of non-negative fourth-rank tensors for viscosity and plasticity. The viscous model predicts qualitatively most of the time-dependent viscous shear-stress and normal-stress effects observed experimentally in Stokesian suspensions. The addition of plastic terms allows for yield stress arising from mechanical contact between particles, and the purely plastic form provides a model for quasi-static deformation of dry granular media. Addition of viscous effects to the latter provides a generalization of models currently being employed to describe dense, rapid granular flows, where the relevant microstructural time scale is associated with granular micro-inertia. A brief consideration is given to non-homogeneous (Acrivos-Leighton) models, of a type that allow for particle segregation and possibly for material instability.

13:33

HK 2 The rise velocity and shape of an air bubble moving in HASE fluid E. SOTO, C. GOUJON, T. BEHAGHEL, R. ZENIT, *IIM-UNAM, Mexico* Experiments were conducted to determine the shape and the rise velocity of an air bubble moving in a HASE fluid. These type of non Newtonian materials can be classified as associative fluids, because their internal structure is formed by hydrophobic molecules which associate or dissociate as a result of flow. In particular, the liquid used in this investigation has a nearly constant shear viscosity for a wide range of shear rates but shows significant elasticity above a certain critical shear rate. Millimetric size bubbles were released from rest in a tall cylindrical container. Two types of images were obtained: high resolution photographs, from which the bubble shape and volume were obtained; and, low resolution high speed videos were used to measure the bubble velocity. We found that the bubble velocity increases with the bubble volume; however, a sudden increase of the bubble velocity is observed as the bubble volume reaches a critical value. This phenomena, known as the bubble velocity discontinuity, has been observed in other non Newtonian fluids but, to our knowledge, has never been reported for associative fluids. Additionally, we identified that a significant change of the bubble shape occurs along with the appearance of the velocity discontinuity. Moreover, by performing PIV measurements we are able to relate the appearance of the velocity jump with values of the local shear rate at which the elasticity of the fluid becomes important.

either computational or experimental studies of flow phenomena. The outstanding entries, selected by a panel of referees for artistic content, originality, and ability to convey information, will be honored during the meeting and will appear in the annual Gallery of Fluid Motion article in a future issue of *Physics of Fluids*.

GALLERY OF FLUID MOTION POSTERS

1. *Flow Bifurcations Due to Inertia or Viscoelasticity Greatly Enhance the Rate of Heat and Mass Transfer to Neutrally Buoyant Particles.*

Donald L. Koch and Ganesh Subramanian, Cornell University.

2. *Interaction of a Vortex Ring with a Moving Sphere.*

Yann Jouanne, Ecole Polytechnique de l'Université de Nantes, **and James J. Allen**, New Mexico State University.

3. *Turbulent Spots and the Mechanism of Their Origin in Passing Wake Induced Boundary Layer Transition.*

Xiaohua Wu, Stanford University, **and Paul A. Durbin**, Stanford University and Iowa State University.

4. *Shock Wave Interaction with Rebounded Bubbles (Bubble Candies).*

Georgy N. Sankin, W. Neal Simmons and Pei Zhong, Duke University.

5. *Tip to Edge Streaming in Non-Newtonian Flows.*

Enrique Soto, Celione Goujon, Thibault Behaghel, Roberto Zenit and Octavio Manero, Instituto de Investigaciones en Materiales, UNAM, Mexico.

6. *Visualization of Vortex Structures Downstream of a Circular Lobed Nozzle/Mixer.*

Hui Hu, Iowa State University, **and Toshio Kobayashi**, Japan Automobile Research Institute.

7. *Three-Dimensional Wave Patterns in Falling Films.*

Benoit Scheid, Université Libre de Bruxelles.

8. *Rivulet Instability in a Locally Heated Falling Film.*

Benoit Scheid, Oleg A. Kabov and Pierre Colinet, Université Libre de Bruxelles.

9. *Initiation of the Emulsification of an Oil-Water Mixture.*

J. F. Hernández-Sánchez, R. Zenit, Universidad Nacional Autonoma de Mexico, **and G.M. Homsy**, University of Califonia at Santa Barbara.

10. *Birth of a Bubble-Type Vortex Breakdown.*

T. T. Lim and Y. D. Cui, National University of Singapore, **and J. M. Lopez**, Arizona State University.

11. *Two-Dimensional Primary Instabilities of Flow Generated by an Oscillating Circular Cylinder.*

John R. Elston, Monash University, **Hugh M. Blackburn**, CSIRO, **and John Sheridan**, Monash University.

12. *Microscale Breaking Induced by Wave Blocking: Nonlinearity and Universal Crest Profile.*

Afieng Yao and Chin H. Wu, University of Wisconsin, Madison.

13. *Families of Vortices in an Indeterminate Origin Nozzle Jet.*

Fangjun Shu, Michael W. Plesniak and Paul E. Sojka, Purdue University.

14. *Round and Round it Goes.*

Claudia Cenedese, Woods Hole Oceanographic Institution, **and Rachel Bueno de Mesquita**, Universitá di Roma "La Sapienza".

15. *Swirl Generated By Jet Engine Fuel Nozzle Rig.*

Xiaohua Wu, Gianluca Iaccarino and Parviz Moin, Stanford University.

16. *Plume Structure in High Rayleigh Number Convection.*

Baburaj A. Puthanveettil, Indian Institute of Technology Madras, **and Jaywant H. Arakeri**, Indian Institute of Science Bangalore.

17. *Virtual Submarine in a Stratified Sea.*

Yakov D. Afanasyev, Memorial University of Newfoundland.

18. *Rupture of a Magnetic Thin Film in a Perpendicular Magnetic Field.*

Ching-Yao Chen and L.-W. Lo, National Yunlin University of Science & Technology.

19. *Labyrinthine Instability of a Miscible Magnetic Drop.*

C.-Y. Wen, Da-Yeh University, **Ching-Yao Chen and T.-C. Kuan**, National Yunlin University of Science & Technology.

20. *The Fluid-Mechanical Sewing-Machine.*

Sunny Chiu-Webster and John Lister, University of Cambridge.

21. *The Dynamics of a Closed Flexible Body in a High-Speed Flow.*

PASI 2007

Pan-American Advanced Studies Institute on Interfacial Fluid Dynamics: From Theory to Applications

August 6-17, 2007 - Mar del Plata, Argentina

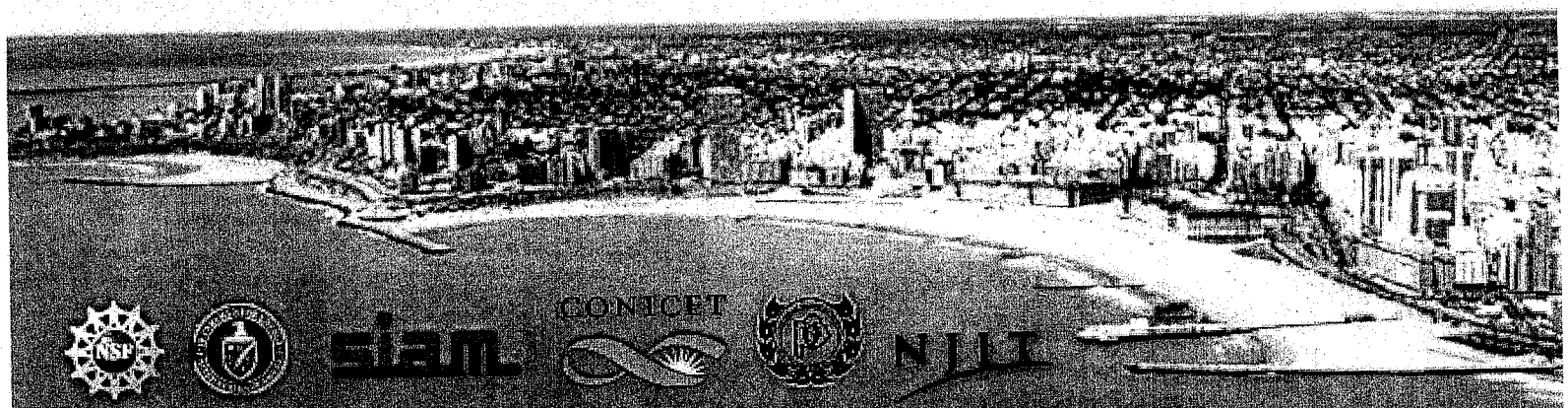

Speakers and Discussion Leaders (partial list)

- J. Diez, UNCPBA, Argentina
- J. Feng, UBC, Canada
- J. Gratton, UBA, Argentina
- D. Joseph, U. Minnesota, USA
- L. Kondic, NJIT, USA
- O. Manero, UNAM, Mexico
- M. Miksis, Northwestern U., USA
- P. Neitzel, GeorgiaTech, USA
- D. Papageorgiou, NJIT, USA
- E. Rame, NASA, USA
- M. Rosen, UBA, Argentina
- M. Shelley, NYU, USA
- M. Siegel, NJIT, USA
- P. Steen, Cornell, USA
- J. E. Wesfreid, ESPCI, France

Organizing Committee

- Lou Kondic, NJIT (Chair)
- George (Bud) Homsy, USB
- Javier Diez, UNCPBA
- Marta Rosen, UBA
- Roberto Zenit, UNAM

Full or partial support available for selected applicants from North, Central, and South America

More information http://m.njit.edu/Events/PASI/ or http://www.exa.unicen.edu.ar/pasi2007/

XII Congreso de la División de Fluidos y Plasmas

en conjunto con el

XLIX Congreso Nacional de Física
Sociedad Mexicana de Física

Universidad Autónoma de San Luis Potosí, SLP
del 16 al 19 de octubre de 2006

Se invita a los interesados en la dinámica de fluidos y los plasmas a presentar trabajos de investigación en las áreas de: Flujos astrofísicos, Flujos marinos y atmosféricos, Flujos viscosos, Flujos multifásicos, Medios granulados, Turbulencia, Fluidos no-newtonianos, Física de plasmas y otros.

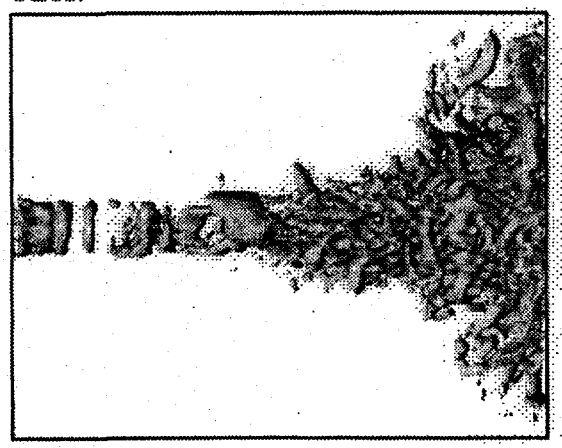

Visualización de un chorro circular supersónico a Mach 2: Estructuras turbulentas. M. Salinas y W. Vicente, II-UNAM

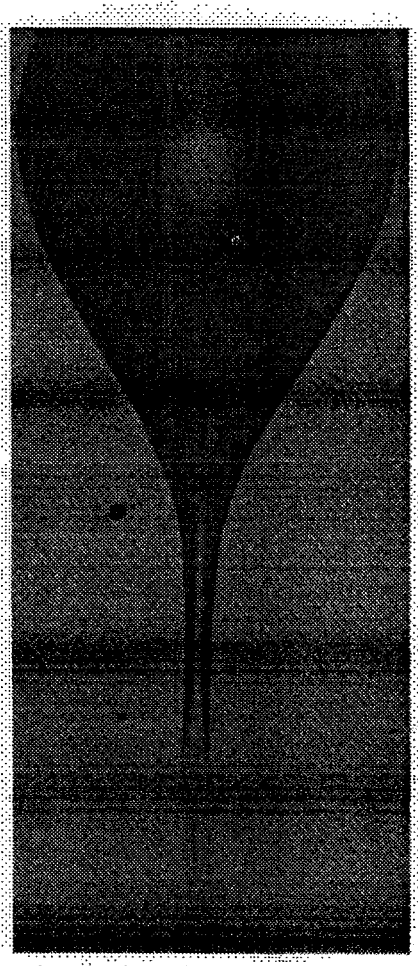

Barbeja con cola de flujo de cuchillo que se mueve en un fluido no newtoniano. HASE (flip wedge streaming). E. Soto, C. Coulon, T. Hohgfeld, O. Manero y R. Zenit, IIM-UNAM

Se invita también a presentar imágenes originales de flujos, producidas experimental o numéricamente, en la GALERIA DE FLUIDOS. Las imágenes serán evaluadas por un comité académico. El trabajo ganador será utilizado para promocionar el siguiente congreso de la división.

Envío de resúmenes hasta el 7 de julio de 2006, en la página:
http://www.smf.mx/cddf o por e-mail al comité organizador.
Para Galería de Fluidos: viernes 29 de septiembre de 2006

Informes: http://www.smf.mx/~dfp-smf
Comité Organizador:
Guadalupe Huelsz, CIE-UNAM, ghl@cie.unam.mx
Sergio Cuevas, CIE-UNAM, scg@cie.unam.mx
Julio Martinell, ICN-UNAM, martinel@nucleares.unam.mx
Arturo Pacheco FCQ-UASLP, apacheco@uaslp.mx
Ricardo Romero FCQ-UASLP, rromerom@uaslp.mx
Catalina Stern FCUNAM catalina@graef.fcienciias.unam.mx (Galería)

División de Fluidos y Plasmas

SMF
Sociedad Mexicana de Física